Bioinspired Anti-Icing Coatings and Spatial Control of Nucleation using Engineered Integral Humidity Sink Effect

by

Xiaoda Sun

A Dissertation Presented in Partial Fulfillment
of the Requirements for the Degree
Doctor of Philosophy

Approved November 2016 by the
Graduate Supervisory Committee:

Konrad Rykaczewski, Chair
Jerry Lin
Patrick Phelan
Robert Wang
Marcus Herrmann
Liping Wang

ARIZONA STATE UNIVERSITY

May 2017

ABSTRACT

Durable, cost-effective, and environmentally friendly anti-icing methods are desired to reduce the icing hazard in many different industrial areas including transportation systems, power plants, power transmission, as well as offshore oil and gas production. In contrast to traditional passive anti-icing surfaces, this thesis work introduces an anti-icing coating that responds to different icing conditions by releasing an antifreeze liquid. It consists of an outer porous superhydrophobic epidermis and a wick-like underlying dermis that is infused with the antifreeze liquid. This bi-layer coating prevents accumulation of frost, freezing fog, and freezing rain, while conventional anti-icing surfaces typically work only in one of these conditions. The bi-layer coating also delays condensation on the exterior surface at least ten times longer than identical system without antifreeze.

It is demonstrated that the significant delay in condensation onset is due to the integral humidity sink effect posed by the hygroscopic antifreeze liquid infused in the porous structure. This effect significantly alters the water vapor concentration field at the coating surface, which delays nucleation of drops and ice. It was demonstrated that with a proper design of the environmental chamber the size of the region of inhibited condensation and condensation frosting around an isolated pore, as well as periodically spaced pores, filled by propylene glycol can be quantitatively predicted from quasi-steady state water vapor concentration field. Theoretical analysis and experiments revealed that the inhibition of nucleation is governed by only two non-dimensional geometrical parameters: the pore size relative to the unit cell size and the ratio of the unit cell size to the thickness of the boundary layer. It is demonstrated that by switching the size of the pores from millimeters

to nanometers, a dramatic depression of the nucleation onset temperature, as well as significantly greater delay in nucleation onset can be achieved.

To

my mother Hongsheng Niu

and my father Maoqi Sun

ACKNOWLEDGMENTS

I have been very fortunate to work at Arizona State University (ASU) during the past three and a half years. I would like to express my deepest thanks to the researchers I worked with, to my department, and to ASU.

First, I would like to acknowledge my research advisor, Prof. Konrad Rykaczewski, for offering me the opportunity to work in his lab. Prof. Rykaczewski has been an excellent advisor throughout my Ph.D. study. He brought ideas from nature to lab and shared his insights of science with me. He taught me the pathway to being a successful researcher. By working with him, I expanded my understanding of physics, learned experiment skills, and practiced scientific writing and professional presenting. His passion and diligence will influence my enthusiasm in science and in my life.

I would like to thank my committee members for their kind help on my study. They provided suggestions on my research and built my fundamental knowledge in heat transfer, mass transfer, and microscopy.

Next, I would like to thank my colleagues who have been working with me in lab. Viraj Damle helped me build experimental setups, and provided valuable suggestions on my project. I also thank Viraj for his friendly support outside of work. Shanliangzi Liu worked with me on a project focused on flexible sensors, and helped to conduct icing experiments. Aastha Uppal helped to fabricate materials used in my research. I also thank all the other members in Prof. Rykaczewski's group: Matt Ralphs, Akshay Phadnis, Chad Manning, Ajay Roopesh, Rubin Linder, Nick Kemme, and Nick Dhuyvetter. They are kind and patient colleagues.

I thank my mother Hongsheng Niu and my father Maoqi Sun for giving me their endless love, support and guidance of life. I love them forever.

TABLE OF CONTENTS

Page

LIST OF TABLES ix

LIST OF FIGURES x

CHAPTER

1 BACKGROUND AND INTRODUCTION 1

1.1 Icing Hazards and De-icing Methods 1

1.2 Effect of Surface Wetting Properties and the Humidity Sink Process 4

1.3 Overview of This Dissertation 6

2 BIOINSPIRED STIMULI-RESPONSIVE AND ANTIFREEZE-SECRETING ANTI-ICING COATINGS 8

2.1 Introduction 8

2.2 Results 10

2.2.1 Materials and Fabrication 10

2.2.2 Freezing Rain Experiments 13

2.2.3 Freezing Fog Experiments 19

2.2.4 Condensation Frosting Experiments 21

2.3 Conclusions 24

3 INHIBITION OF CONDENSATION FROSTING BY ARRAYS OF HYGROSCOPIC ANTIFREEZE DROPS 27

CHAPTER Page

3.1 Introduction 27

3.2 Results and Ddiscussion.....30

3.2.1 Sample Fabrication and Experimental Procedure 30

3.2.2 Frost Growth Dynamics Around Individual Hydroscopic Drops 33

3.2.3 Frost Growth Around Arrays of Hygroscopic Macroscale Drops and Hygroscopic Films 38

3.2.4 Frost Growth Around Sprayed Arrays of Hygroscopic Microscale Drops……..46

3.3 Conclusions 47

4 SPATIAL CONTROL OF DROPLET AND FROST NUCLEATION USING ENGINEERED INTEGRAL HUMIDITY SINK EFFECT 50

4.1 Introduction 50

4.2 Sample Fabrication and Experimental Setup 54

4.2.1 Environmental Chamber 54

4.2.2 Sample Preparation 58

4.2.3 Finite Element Simulations and Simulation Data Analysis 62

4.3 Results and Discussion.....63

4.3.1 Inhibition of Nucleation, Droplet and Frost Growth Around Isolated Antifreeze Filled Pores..... 63

4.3.2 Inhibition of Nucleation, Droplet and Frost Growth by Arrays of Antifreeze Filled Pores 67

CHAPTER Page

4.3.3 The Temporal Anti-frosting Performance of the Nanoporous Bi-layer Antifreeze Infused Coatings 83

4.4 Conclusions 87

5 CONCLUSION AND RECOMMENDATIONS FOR FUTURE WORK 90

5.1 Summary of the Performed Work 90

5.2 Recommendations for Future Work 95

5.3 Original Contributions and Publications 96

REFERENCES 99

LIST OF TABLES

Table Page

3.1 Static (Θ), Advancing (Θ_a), And Receding (Θ_r) Contact Angles of Different Studied Liquids on The PTFE-Coated Silicon Water. Percentage of Propylene Glycol (PG) in Water Solution is Indicated in Per Weight Terms. 31

4.1 Polycarbonate Membrane Geometrical Information Provided by Manufacturer (Http://Www.Sterlitech.Com/Pcte-Product-And-Performance-Characteristics.Html).[A.]Tolerance + 0%, -20% [B.] Tolerance +/-15%..... 61

4.2 95% Confidence Interval Values for The Fitted Model Parameters for $1 - e - wbau.$ 71

4.3 Fitted Functions of F for Cell Size a=1 Mm, 250 Mm, 1 Mm; The Difference of F Between Square and Round Pore Shapes in Three Cell Size a..... 82

LIST OF FIGURES

Figure Page

1.1 (a) to (c) Schematics and Example Images of Ice Type Formed in Different Atmospheric Conditions: (a) Frost Formed by Desublimation or Condensation Followed by Freezing, (b) Rime Formed Through Freezing Fog, and (c) Glaze Formed Through Freezing Rain. 2

2.1 (a) Schematic of the Stimuli Responsive Antifreeze Secreting Anti-Icing Coating Inspired by the Functionality and Bi-Layer Architecture of a Poison Dart Frog Skin. the Porous Superhydrophobic Epidermis Separates the Antifreeze Infused Dermis from the Environment; (b) Schematic Showing That the Antifreeze Liquid is Secreted Through the Pores in Response to Contact With Ice or Frost Forming on the Surface, Which Results in Melting of the Ice or Frost. Subsequently, the Melt is Removed via Air Motion or Partially Wicked Back into the Dermis. 9

2.2 Schematic, Top-Down and Cross-Sectional SEM Images of the Porous Superhydrophobic Hydrobeadtm Epidermis Sprayed onto Superhydrophilic Dermis Consisting of a Nanoporous Nylon Membrane; Optical Images of Water Drop in Contact With the Two Layers Demonstrate the Superhydrophilic Nature of the Dermis and Superhydrophobic Nature of the Epidermis (Irrelevant of Whether the Dermis is or is Not Filled with Antifreeze). The Small Water Droplets were Dyed Blue to Facilitate Interpretation. 12

2.3 Sequence of Images Taken at 4000 Fps Showing Droplet Supercooled to -5°C Impacting onto Cu+HB and Ny+HB+PG Samples Cooled to -10°C in Completely Dry

Conditions (Relative Humidity ~0% with Environment at 15°C). Images for Weber Numbers (We) in Range of ~10 to 75 are Shown. Time Starting from ~1 to 2 Ms Prior to Impact is Indicated in Milliseconds Within the Images. 15

2.4 (a) Results of Simulated Freezing Rain Experiments Showing Images of All Surfaces 20 Minutes into the Experiments as Well as of the Ny+HB+PG Surface After 10, 30, and 60 Minutes After Start of the Experiment. Icing Onset (I.E., the Time That Presence of Ice Was First Observed on the Surface) is Also Indicated for All Surfaces; (b) and (c) Sequence of Images Taken at 4000 Fps Showing Drops Impacting onto (b) Cu+HB and (c) Ny+HB+PG Samples at Different Time Intervals During the Freezing Rain Experiments. Time Starting from ~1 to 2 ms Prior to Impact is Indicated in Milliseconds Within the Images. 17

2.5 (a) Side-View Optical Images of Vertically Mounted Samples at -10°C after 20 Minutes of Exposure to Water Mist (for Reference, Cu Sample is Also Shown Prior to Exposure), (b) Histogram of Average Thickness of the Ice Accumulated in 20 Minutes with Sample Surface Temperatures of -5°C and -10°C, (c) Top-Down Images of Ice Accumulated after 33 Minutes on Ny+PG on Ny+HB+PG Cooled to -10°C, (d) Thickness of Ice Growing on Ny+HB+PG at -10°C as a Function of Time with Nitrogen Gas Exposure Points Indicated, and (e) Images of Iced-Over Ny+HB+PG, Cu, and Cu+HB Samples after Short Exposure to Pressurized Nitrogen Gas..... 19

2.6 (a) Top-Down Images of All Samples after 20 Minutes of Cooling at -10°C in Moist Air at 60% Relative Humidity and 22°C, and (b) Corresponding Histogram of Measured Frost Heights; (c) Top-Down Images of Extended Testing in the Same

Conditions Testing of Single Layer (“1x”) Ny+HB and Ny+HB+PG; and (d) Histogram of Frost “Onset” Time, Which for Samples Without Antifreeze This Refers to the Time That First Water Freezing Was Observed; for the Ny+PG This Time Refers to Onset of Slush Formation, While for the Ny+HB+PG This Time Refers to First Visible Ice Crystal Formation within the Liquid Film. For the Ny+HB+PG Sample Time That Substantial Ice Accumulation (Uniform Frost Growth) Was Initiated is Also Indicated. to Facilitate Interpretation, Antifreeze is Dyed Blue and the Nylon Membrane Samples are Taped Down Using Either Black or Purple Tape. 24

3.1 Illustration of Condensation and Frost Nucleation Inhibition Using a (a) Single Hygroscopic Drop, (c) Multiple Hygroscopic Drops with $S>2\delta$, and (d) Multiple Hygroscopic Drops with $S<2\delta$ (I.e. Overlapping Regions of Inhibited Nucleation); and (b) Equilibrium Water Vapor Pressure Above Surface of Water, Ice, Saturated Water Salt Solution, and 60%, 90%, and 99% by Weight Propylene Glycol Water Solution in the Temperature Range of -40°C to 20°C. PBL, Δl, Δice Stand for Partial Pressure of Water at Boundary Layer, and Radii of Water and Ice RIC, Respectively. 28

3.2 Representative Frost Growth Dynamics Around Isolated Hygroscopic Drop: (a) Plot of Drop (R) and RIC (Δ) Radius vs. Time for 2 µl Isolated Drops of Saturated Salt Solution and 99% Propylene Glycol and (b) Images Corresponding to the Latter, (c) Plot of Variation Δ/R vs. of R/R0 for Six Different Drops (PG-Propylene Glycol, Nacl-Saturated Water Solution), and (d) Schematic Illustrating the Four Observed Frost Growth Stages Around Hygroscopic Drops. 37

Figure Page

3.3 Images of Condensation Frosting Around Four 2 µl Propylene Glycol (PG) Drops with (a) Sparse Separation of $S/2R0$~2.2 and (b) Dense Separation of $S/2R0$~1.3, and (c) Corresponding Plot of Temporal Evolution of the Average Drop Radius (Data for Analogous Experiment with Four 2 µl Drops of Nacl Saturated Water Solution are Also Presented). 39

3.4 Images of Condensation Frosting Over (a) An Array of 30 Propylene Glycol (PG) Drops with $S/2R0\sim$ 1.4 to 1.5, and (b) a Film of 60 µl Propylene Glycol, (c) Corresponding Plot of Temporal Evolution of the Average Drop Radius, and (d) Frost Coverage. Data for Nacl Saturated Water is Also Indicated in (c) and (d). 43

3.5 Images of Frost Propagation of Microscale Droplets of (a) Salt Saturated Water and (b) Propylene Glycol (PG); (c) Percentage of Frost Coverage Corresponding to (a) and (b) as Well as Equivalent Experiments with Arrays Salt Saturated Water Microdroplets. 45

4.1 Schematics and Images of Nucleation and Condensation Frosting Inhibition on a Hydrophobic Membrane with (a) An Individual Pore with Diameter of 500 mm and (b & c) 4 by 4 Square Pore Array with (b) Non-Overlapping Regions of Inhibited Condensation and Condensation Frosting (RIC) Due to Pore Spacing, a, Being Larger Than Size of RIC ($a \geqslant 2\delta$), and (c) Overlapping RIC (I.e. $a \leqslant 2\delta$); in This Case Condensation Frosting is Completely Inhibited in-Between the Pores Due to the Integral Humidity Sink Effect. in All Cases the Membranes are on Top of a Hydrophilic Porous Layer Infused with Propylene Glycol Antifreeze. 54

Figure Page

4.2 (a) Schematic of the Designed Environmental Chamber and (b) Plot Comparing Experimentally Measured Thickness of Condensing Water Film on Superhydrophilic Copper Oxide Surface and Same Value Predicted from One Dimensional Diffusion Theory for Three Different Source (Wet Cotton) Temperatures of 20°C, 25°C, and 30°C with Sample Temperature at 5°C..... 57

4.3 Example Image Processing and Statistical Analysis of 200 Nm Polycarbonate Tract Etch Membrane Pore Density: (a) Original SEM Image (Image Width 22 mm), (b) Image after Edge Detection, Filling, and Binarization, and (c) Imaged of the Colorized Detected Components, (d) Plot of the Location of the Computed Component Centroids (in Pixels), and (e) Histogram of the Distance Between Neighboring Pores (4 Closest Neighbors Analyzed) Compiled from Analysis of Three SEM Images. 62

4.4 (a) Plot of Water Vapor Saturation Concentration Above Surface of Water and Ice as Well as for Several Concentrations Propylene Glycol (PG) and Water Solutions (Concentration Specified by Weight) as Function of Temperature; (b) Plot of the Measured and Theoretically Predicted Radius of the Circular Regions of Inhibited Condensation and Condensation Frosting (Circular RIC with Radius Δ) Around Isolated Pores with Radius R in Membranes with Hydrophobic and Hydrophilic Exterior Surface Cooled from to -6°C±2 with Source Temperature of 20°C±1, and (c) Plot of the Measured and Theoretically Predicted $R\delta$ Ratio for Different Vapor Source Temperatures with Fixed Sample Temperature of -6°C±2..... 66

4.5 (a) Schematic Representation of the Mathematical Formulation of the Integral Humidity Sink Effect Posed by Array of Square Pores with Uniform Concentration

Figure Page

CHS at the Pore Surface as Well as Re-Formulated Version of the Problem Proposed by Muzyczka Et Al.[116] with Equivalent Mass Sink, (b) Plot of Concentration Profiles Along the Unit Cell Diagonal, s, for the Two Problem Formulations Simulated Using FEM and Calculated Using Muzyczka et al.[116] Analytical Solution with J_{HS} Directly Substituted from FEM Simulations as Well as Calculated Using the Proposed Empirical Formula, and (c) Plot of the Normalized Mass Sink, J_{HS}/J_{max}, and Proposed Empirical Fits as a Function of Non-Dimensional Pore Size, b/a, for Various Pore to Boundary Layer Thickness Ratio a/h_{BL}. 72

4.6 Variation of the Function $\Omega 1$ with the Non-Dimensional Pore Size (ba) 74

4.7 (a) Plot of $\Omega 0$ as a Function of Non-Dimensional Pore Size, b/a, for Various Ratios of the Array Unit Cell Size to Boundary Layer Thickness, a/h_{BL}; the Inset Shows Variation of the Excess Saturation to Pore Surface Concentration Ratio, $C_{sat}(T_{surface}) - C_{BL}(T_{BL})C_{HS}(T_{surface}) - C_{BL}(T_{BL})$, as a Function of Surface Temperature, $T_{surface}$, for Fixed Boundary Layer Temperature of T_{BL}=298 K; (b) Plot of Theoretically Predicted (Colored Areas) and Experimentally Measured (Points with Darker Tone of the Colored Area Correspond to This a) Nucleation Onset Surface Temperature, T_{NOST}, as a Function of b/a for Various a/h_{BL} Ratios (to Account for Some Dilution Effects, Predictions for Propylene Glycol Concentrations Between 75% and 99% are Plotted for Each Unit Cell Size), and (c) Example Images of the Porous Membranes Used in the Experiments with Unit Cell Size, a, of 1 mm (Laser Etched PTFE Membranes), 250 mm (PDMS Coated Steel Mesh), and ~500 nm (for the

Polycarbonate Membranes An Equivalent Cell Size Was Found Through Image Analysis). 80

4.8 (a) Plot of Simulation Result of Total Flux on the Pore Area, F, of Cell Size a=1 Mm, 250 Mm, 1 Mm for Square and Round Pores; Simulation Results of Cell Size a=1 Mm, 250 Mm, 1 Mm are Presented in (b)(c)(d) Respectively. 81

4.9 Histogram and Images Summarizing the Results of the Extended Frosting Experiments of the Nanoporous Bi-Layer Antifreeze Infused Coatings with Surface Temperature of (a) 253 K and (b) 243 K. 86

CHAPTER 1

BACKGROUND AND INTRODUCTION

1.1. Icing Hazards and De-icing Methods

Ice accumulation can make commute by foot,[1] car,[2] water[3] or air[4] hazardous. Furthermore, icing can cause major electrical outages,[5] disrupt offshore gas and oil production[3,6,7] as well as decrease efficiency of wind power generation.[8] While number of different anti-icing techniques exist, they can be expensive, in-effective, and environmentally unfriendly. The problems posed by ice are due to its physical properties, which in turn can vary greatly between different forms of ice.[7] In general, ice accumulation occurs through nucleation from the vapor phase to solid phase (desublimation), droplet condensation followed by freezing (condensation frosting), supercooled droplets or snow impingement. For example, snow (ice crystals) and sleet (frozen drops) precipitation can cause slipping hazards, however without melting and refreezing, these types of solid ice precipitates do not pose high safety risks for ships and aircraft[7] because they can be easily removed through air motion. Besides solid precipitation, ice can accumulate on surfaces either through heterogeneous nucleation from the vapor phase or through liquid precipitation followed by freezing. Nucleation from the vapor phase via desublimation or condensation followed by freezing leads to the formation of frost, which consists of sparse dendritic crystal structures that become denser with time (see Figure 1a).[7,9] In turn, the type of ice formed by impinging droplets depends on their size range. Freezing rain, consisting of large droplets with diameters ranging from 70 μm to even a few millimeters, leads to the formation of clear, dense, and hard ice, referred to as glaze (see Figure 1c).[7] In contrast,

rime is a white, brittle, feather-like ice that forms because of freezing of supercooled droplets with diameters in the range of 5 to 70 μm originating from clouds or fog (see

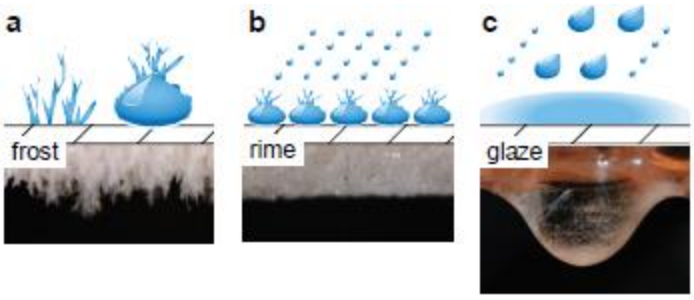

Figure 1.1. (a) to (c) Schematics and example images of ice type formed in different atmospheric conditions: (a) frost formed by desublimation or condensation followed by freezing, (b) rime formed through freezing fog, and (c) glaze formed through freezing rain.

Figure 1b).[7]

A common approach used in commercial applications for icing prevention is the use of chemicals that depress the freezing point of water. These chemicals can range from salts and beet juice to alcohols and glycols.[6] The latter antifreeze substances are non-corrosive and are preferred by the aviation industry. The most common dispensing approach is to spray a large amount of the glycol-based fluids onto the aircraft prior to departure. An alternative approach, used to prevent icing of small airplanes during flight, is flooding the aircraft surface with a film of glycol-based fluids.[6,10] To avoid the need for the rather heavy liquid pumping system, a porous wick can be used to resupply the antifreeze from a reservoir through capillary forces.[6,11] Antifreeze substances can also be chemically embedded into and slowly released from sol-gel coatings.[12] Regardless of the dispensing method, however, the use of antifreeze raises concerns related to its cost, supply, and

environmental impact.[13] These issues have motivated the search for alternative, fully passive routes to prevent ice accumulation or at least, to facilitate its removal by minimizing its adhesion strength. The use of hydrophobic coatings addresses both of these goals by increasing free energy barriers to ice nucleation[14–19] and reducing ice adhesion strength. [13,20,21] However, the extent of these two qualities of smooth hydrophobic surfaces have proven to be insufficient for anti-icing coatings, which is why recent research has focused on using surface engineering to exceed the baseline set by these coatings.

In the case of icing, nature is the source of the problem but can also offer inspiration for its potential solutions.[22] For example, the remarkable water-repelling and non-adhesive characteristics of the lotus leaf[23–25] and the pitcher plant[26] have inspired the design of anti-icing superhydrophobic (SHS)[13,15,27–31] and lubricant impregnated surfaces (LIS).[32–37] However, recent research has shown that these coatings do not prevent accumulation of all the types of ice illustrated in Figure 1.[15,35] SHS are hydrophobic surfaces with nano- and micro-scale texture that repel water due to air trapped within its surface. With tuned surface topology, these surfaces can significantly slow down glaze-like ice accumulation by repelling impinging drops[38–43] and by disrupting heterogeneous ice nucleation dynamics.[18,39,41,43] The latter mechanism can lead to dramatically decreased nucleation temperature and very long delay in freezing.[39,43] However, the majority of SHS are susceptible to frosting.[15,35,44–46] When covered by frost, SHS do not repel water droplets and can rapidly ice over.[15] Furthermore, the presence of surface texture can increase adhesion of glaze-like ice as compared to flat hydrophobic surfaces.[28,41,47,48] Use of LIS has been reported to resolve some of the shortcomings of anti-icing SHS.[28,33] These coatings attain their liquid shedding and low adhesive properties by replacing the air

trapped within the nano- and micro-scale topological features of SHS with a low surface energy lubricant that is immiscible with water.[26,32,34,49] LIS are also omniphobic and can have self-cleaning and self-healing characteristics.[26,34,50,51] Despite these attractive properties, the anti-icing functionality of LIS can be compromised by frosting as well.[35] In particular, the lubricant was shown to drain from within the textured substrate into the forming frost layer in response to nucleation of nano-scale icicles on top of frozen droplets.[35] As a result, a significant portion of the lubricant was lost with each frosting-defrosting cycle, and its replenishment would become necessary for sustained anti-icing performance.[35] Besides textured surfaces impregnated with lubricants that are immiscible with water, anti-icing coatings that consist of hygroscopic polymers that attract and are lubricated by water have been recently described.[52,53] This class of coatings suppresses the crystallization of water adsorbed within the polymers, leading to formation of a thin lubricating water layer between the substrate and the ice. However, the freezing suppression ceases once the polymer is over-saturated with water, which could occur rapidly during atmospheric precipitation of water.

1.2. Effect of Surface Wetting Properties and the Humidity Sink Process

From a thermodynamic point of view, possibility of heterogeneous ice or drop nucleation on a flat substrate depends on the surface's wetting properties and concentration of water vapor above it. The embryo formation rate J can be expressed as:[9,14,15,54–56]

$$J = \exp(\Delta G_c / kT) \qquad \text{(Eq. 1)}$$

Where *k* is the Boltzmann constant, *T* is temperature, and ΔG_c is the critical Gibbs free energy change for nucleation. After substituting the expression for the nuclei critical radius, the Gibbs free energy for nucleation can be expressed as:

$$\Delta G_c = \frac{4\pi V_m^2 \sigma^3}{3\left(RTln(P/P_{sat})\right)^2}(2 - 3cos\theta + cos^3\theta) \qquad \text{(Eq. 2)}$$

Where θ is the angle that the edge of the nuclei makes when in contact with the solid, σ is surface energy of the nuclei, V_m is the molar volume of liquid, R is the universal gas constant, P is the partial pressure of water vapor in the surrounding, and P_{SAT} is the water vapor saturation pressure at the surface. Put together, Eq. 1.1 and 1.2 imply that the nucleation rate can be exponentially decreased using two approaches: (1) by increasing the water contact angle of the surface and (2) by decreasing the water vapor concentration above it. The first approach has provided rationale for use of hydrophobic coatings (θ>90°) to delay formation of frost and ice.[9,57–60] Following the same argument, superhydrophobic surfaces (θ>150°) have been proposed as improved anti-frosting/icing coatings.[15,61–63] However, as discussed in the previous section, SHS surfaces are highly susceptible to condensation and condensation frosting. In contrast to the extensive research effort motivated by the first approach, my research focuses on delaying frost formation by altering the vapor concentration above the surface. Since the partial pressure of water at the hygroscopic liquid's surface is lower than P_{SAT}, the hygroscopic drop can act as a humidity sink and form a region of inhibited condensation (RIC), and prevent condensation frosting, around it.[64–68] In this region, frost formation is delayed since condensation is absent. The hypothesis is that frost can be inhibited if the spacing between two drops is

less than twice the radius of RIC, 2δ. Furthermore, frost also can be inhibited on the surface of a porous membrane if the spacing of the pores is less than 2δ of a pore infused with hygroscopic antifreeze. To validate the hypothesis, a series of icing experiments are carried out using drop arrays of hygroscopic liquid.

1.3. Overview of This Dissertation

This dissertation presents three studies investigating performance and fundamental transport processes on the bi-layer anti-icing coatings. Chaptor 2 presents the stimuli-responsive bi-layer anti-icing coating design inspired by the skin of a poison dart frog. It contains a superhydrophobic porous outer layer and a inner layer to store antifreeze. The outer layer seperates the antifreeze and the environment to avoid fast dilution and loss of antifreeze through water droplet impacting. Antifreeze can be secreted to the outer layer in response of contact with frost or ice penetrating the pores. To validate the functionality of this coating, testing in three icing senarios are carried out in this dissertation: freezing rain, freezing mist and condensation frosting. For all the senarios, the bi-layer coating is compared with bare metal surfaces, teflon coating, SHS, and LIS.

Chapters 3 presents a study of the humidity sink effect around drops or pores filled with antifreeze, which can be used to inhibit condensation and frost formation. Previous studies have shown that condensation and condensation frosting can be inhibited around a region (RIC) around a single droplet of hygroscopic liquid. In this chapter, experiments using arrays of hygroscopic droplets were conducted to show the relationship between inhibition of nucleation and spatial arrangement of hygroscopic droplets.

Chapter 4 presents a study of the spatial control of nucleation using engineered integral humidity sink effect. The humidity sink effect around hygroscopic droplet arrays is described in Chapter 3. Chapter 4 extended the integral humidity sink effect to bi-layer structures consisting of engineered porous layer and antifreeze layer. An analytical model of vapor concentration field around the pore arrays is developed and validated experimentally. The model is then used to uncover intriguing pore sizing effect on vanishing surface concentration gradient. The implications of this effect are demonstrated experimentally.

CHAPTER 2

BIOINSPIRED STIMULI-RESPONSIVE AND ANTIFREEZE-SECRETING ANTI-ICING COATINGS

2.1. Introduction

In this Chapter, it is demonstrated that the icing problem can be resolved by mimicking active natural systems that secrete functional liquids only in response to external stimuli. For example, poison dart frogs have two types of specialized glands in their skin to produce mucus and toxins.[69] These amphibians continually secrete the mucus to remain hydrated but secrete the toxin only to deter predators.[69] Inspired by this biological example, an anti-icing coating that prevents accumulation of all forms of ice by responding to its presence with secretion of antifreeze liquid was developed. The schematic in Figure 2.1a illustrates that the stimuli-responsive multifunctionality of the coating is achieved by mimicking the bi-layer skin architecture of a frog, with a permeable superhydrophobic "epidermis" that separates antifreeze-infused superhydrophilic "dermis" from the environment. As in the case of SHS and LIS, the epidermis should prevent glaze formation by shedding large impinging droplets. In turn, when atmospheric conditions lead to growth of frost and rime, the porosity of the epidermis should enable microscale contact between the antifreeze and either liquid or solid water. This contact could trigger the functional liquid release that leads to melting and eventual removal of the ice from the surface (see schematic Figure 2.1b). In instances of extreme icing conditions, antifreeze release could also facilitate accumulated ice removal by creating of a thin lubricating melt layer. This approach is a semi-passive anti-icing solution that can be viewed as a hybrid method between icing-

prevention by antifreeze dispensing and by repelling impinging drops. The hypothesis is that the new coating architecture will reduce the need for antifreeze liquid by dispensing antifreeze only when needed, which would have significant economic and environmental benefits. Here the feasibility of this bi-layer anti-icing "skin" is demonstrated and its performance is compared to a set of reference and state-of-the-art anti-icing surfaces in

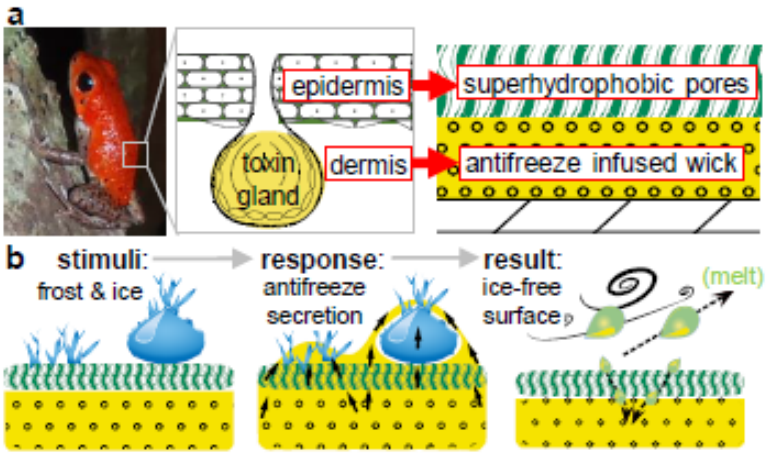

Figure 2.1 (a) schematic of the stimuli responsive antifreeze secreting anti-icing coating inspired by the functionality and bi-layer architecture of a poison dart frog skin. The porous superhydrophobic epidermis separates the antifreeze infused dermis from the environment; (b) schematic showing that the antifreeze liquid is secreted through the pores in response to contact with ice or frost forming on the surface, which results in melting of the ice or frost. Subsequently, the melt is removed via air motion or partially wicked back into the dermis.

three simulated ice-forming conditions: freezing rain, freezing fog, and condensation frosting. The mechanisms responsible for antifreeze release in each icing scenario and their relation to the measured antifreeze use is described.

2.2. Results

2.2.1. Materials and Fabrication

To fabricate the bi-layer epidermis-dermis coating architecture a hierarchical polymeric superhydrophobic shell (Hydrobead^{TM} or HB) was sprayed onto a nylon membrane (Ny) with thickness and a pore size of 170 µm and 0.45 µm, respectively (see SEM images in Figure 2.2). Spraying of the membrane for 30 s from 1 m away resulted in a 20 µm to 100 µm thick porous superhydrophobic epidermis with static water contact angle of 162°±1.2° and contact angle hysteresis (CAH) of 2.4°±1.8°. The fabrication of the epidermis did not affect the wetting properties of the underlying superhydrophilic dermis, which wicked in water (i.e., ~ 0° water contact angle). Illustrating its separating capabilities, the outer layer remained superhydrophobic even after the bottom wick layer was infused with propylene glycol (PG) antifreeze (see Figure 2.2). Furthermore, the contact angle and CAH of sessile water drops on the epidermis was not affected by the time that has passed since antifreeze infusion into the dermis. The anti-icing performance of the bi-layer skin, referred to as the Ny+HB+PG sample (for Nylon+Hydrobead+Propylene Glycol combination), was compared to a set of reference coatings as well as SHS, LIS, and antifreeze-infused hydrophilic porous surfaces.[6,11] The latter sample consisted of antifreeze-infused nylon membrane (Ny+PG) and was used in order to quantify how much antifreeze can be conserved by the addition of the epidermis layer. To facilitate observation of antifreeze interactions with water and ice, the PG liquid infused into Ny+PG and Ny+HB+PG was dyed blue for all the simulated icing experiments. The other samples were prepared on mirror-polished copper by plasma deposition of a sub-100 nm-thick

hydrophobic Polytetrafluoroethylene (PTFE)-like film and spraying of Hydrobead^{TM} using the same procedure as with the nylon membrane. The bare polished copper (Cu), hydrophobic copper (Cu+PTFE), and superhydrophobic copper (Cu+HB) samples had static water contact angles of 62.2° ± 1.8°, 116.8° ± 0.3°, and 162.1° ± 0.2°, respectively. To fabricate the LIS, perfluorinated Krytox lubricant was infused into a nanoporous superhydrophobic Repellix^{TM} coating also deposited onto the polished copper substrate as in our previous work.[35] The Repellix coating was selected as the base for the LIS because it consists of a nanostructure with nearly uniform height, which is beneficial for LIS performance.[50,51] The LIS sample had a water contact angle of 120.2±0.8°. As controls, all experiments were also performed on unmodified (Ny) and Hyperbead^{TM} coated (Ny+HB) nylon membranes without antifreeze. Thus, the anti-icing performance of Ny+HB+PG was compared to Cu, Cu+PTFE, Cu+HB, Ny+PG, and as controls Ny and Ny+HB coatings.

The anti-icing performance of the samples was tested in three sets of experiments mimicking freezing rain, freezing fog, and condensation frosting conditions. To simulate glaze build-up in freezing rain conditions, water drops with average diameter of ~2.1 mm pre-chilled to ~0°C were dripped onto the cooled samples. The ability of the cooled surfaces to shed large supercooled water droplets at different impacting speeds in dry environment was also tested. In turn, to simulate growth of rime in freezing fog conditions, a mist of microscale water droplets was generated using an ultrasonic mister with nozzle directed at the cooled sample surface. The condensation frosting experiments were performed by adjusting the relative humidity to 60% (i.e., dew point of 14°C). All icing experiments were performed in a controlled environmental chamber, with air temperature equal to ~22°C, and the initial relative humidity set to below 10% for the simulated fog

and rain experiments. The surface temperature of the samples, measured using a thermocouple mounted on the sample edge, was decreased to and maintained during the experiments at -5°C and/or -10°C using water-cooled Peltier stage.

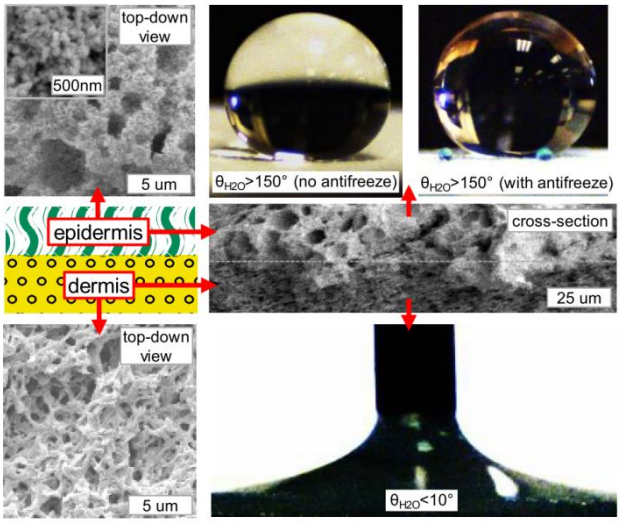

Figure 2.2 Schematic, top-down and cross-sectional SEM images of the porous superhydrophobic HydrobeadTM epidermis sprayed onto superhydrophilic dermis consisting of a nanoporous nylon membrane; optical images of water drop in contact with the two layers demonstrate the superhydrophilic nature of the dermis and superhydrophobic nature of the epidermis (irrelevant of whether the dermis is or is not filled with antifreeze). The small water droplets were dyed blue to facilitate interpretation.

2.2.2. Freezing Rain Experiments

Prior to performing freezing rain experiments, we used high speed imaging to quantify the resistance of the various samples with the superhydrophobic HB coating to impalement by large (~1.8 to 2.4 mm diameter) water drops. Specifically, we imaged impact of individual drops at ambient conditions (drop, surface, and environment at 22°C with 30 to 40% relative humidity) and drops supercooled to -5°C in completely dry conditions (environment at 15°C with ~0% relative humidity) onto surfaces cooled to -10°C. Use of supercooled water drops is more representative of conditions encountered during freezing rain icing.[29,42,43,70–72] Maitra et al.[40,42,43] pointed out recently that supercooling water drops has only a minor influence on surface tension (5 to 10% increase) but very strong effect on the liquid's viscosity (200 to 400% increase). The viscous effects were reported to significantly affect drop impact dynamics, increasing the contact time during drop recoil on ordered hierarchical SHS.[42,43] The images in Figure 2.3 show impact of supercooled drops onto Cu+HB and Ny+HB+PG samples below and in vicinity of the observed impalement Weber number ($We = \rho_l d_0 V^2/\sigma_{lv}$, where ρ_l is the liquid density, d_0 is the pre-collision drop diameter, V is the impact velocity, and σ_{lv} the liquid's surface tension). At low We of ~12 to 17 (V~0.7 to 0.8 m/s) water drops appear to rebound from both of the surfaces within ~5 ms. In turn, supercooled drops with $We \geq 70$ ($V \geq 1.5$ m/s) were impaled on both of the surfaces but in two very different modes (see Figure 2.3). In particular, the drops impacting onto the Cu+HB surface broke-up into multiple smaller droplets. Within about 13 ms some of these smaller droplets bounced away from while others were stuck to the surface. In contrast, drops hitting the Ny+HB+PG sample with

$We \geq 70$ spread and recoiled within ~7 ms, but instead of breaking up and partially rebounding, were entirely impaled onto the surface. A careful evaluation of drops impacting onto the Ny+HB+PG as well as Ny+HB samples with $We < 70$ reveals that some of the impinging water is transferred to the surface even below the full impalement threshold. In particular, results show that even at $We < 70$ a small portion of the impacting water is transferred to the sample while majority of the liquid rebounds. On the Ny+HB sample the transferred portion of liquid was quickly wicked into the nylon membrane making its presence easy to confirm visually. Formation of residual droplets from some of the low We drops impacting the Ny+HB+PG sample in cold and ambient conditions were also observed. These small residual droplets wicked into the surface while majority of the liquid bounced away from it. Thus for the current surface architecture very limited contact between the antifreeze stored within the dermis and drops impacting onto the epidermis occurs even in absence of surface condensation or icing.

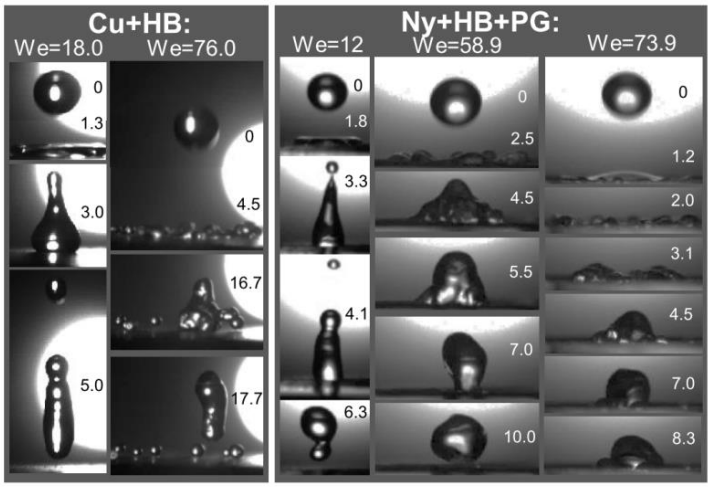

Figure 2.3 Sequence of images taken at 4000 fps showing droplet supercooled to -5°C impacting onto Cu+HB and Ny+HB+PG samples cooled to -10°C in completely dry conditions (relative humidity ~0% with environment at 15°C). Images for Weber numbers (We) in range of ~10 to 75 are shown. Time starting from ~1 to 2 ms prior to impact is indicated in milliseconds within the images.

The freezing rain experiments were preformed following procedure described by Mishchenko et al.[29] In particular, drops with average diameter of 2.1 mm pre-chilled to ~0°C were released at rate of 216 mL/h (3 to 4 drops per second) onto the samples mounted at a 30° tilt and cooled to -10°C. The impact Weber number and velocity were set to an average of $We\sim$ 50 and $V\sim$1.3 m/s by adjusting drop travel distance. Performing the freezing rain experiments with We below the drop impalement threshold enabled a fair comparison of anti-icing performance of our coating with the SHS (i.e. at higher We some small drops are impaled and can freeze rapidly on the Cu+HB surface compromising its superhydrophobic property). As commonly performed in the literature,[15,29] the initial relative humidity was set to below 10% in order to prevent condensation prior to start of

the experiments. However, after the start of the experiment, relative humidity above the surface was not artificially kept below this value through the use of strong dry air or nitrogen flow. Instead the relative humidity was allowed to settle via droplet evaporation to a value of ~50%. The experiments were performed in this way because the scenario with increasing humidity and potential surface condensation simulates much harsher and more realistic icing conditions. Illustrating this point, even the Cu+HB sample, which effectively repelled water droplets in dry environment, began to ice over within a minute after dripping of the large pre-chilled water droplets was started. In fact, images in Figure 2.4a show that icing of all samples apart from the anti-icing bi-layer skin started in less than 5 minutes after water flow began. Similarly, the images in Figure 2.4a show that while after 20 minutes of the experiments the remaining samples are covered with at least 5 mm thick glaze, only a few liquid droplets are pinned to the Ny+HB+PG surface. An extended drop impingement experiment showed that the onset of ice formation on the Ny+HB+PG was delayed by at least a factor of 10 when compared to all other samples. The light blue color of the drops is a clear indication that contact between the water and the dyed antifreeze occurred. The freezing point depression that occurred due to the diffusion of the antifreeze into the drops prevented full glazing-over of the Ny+HB+PG surface to nearly 1 hour.

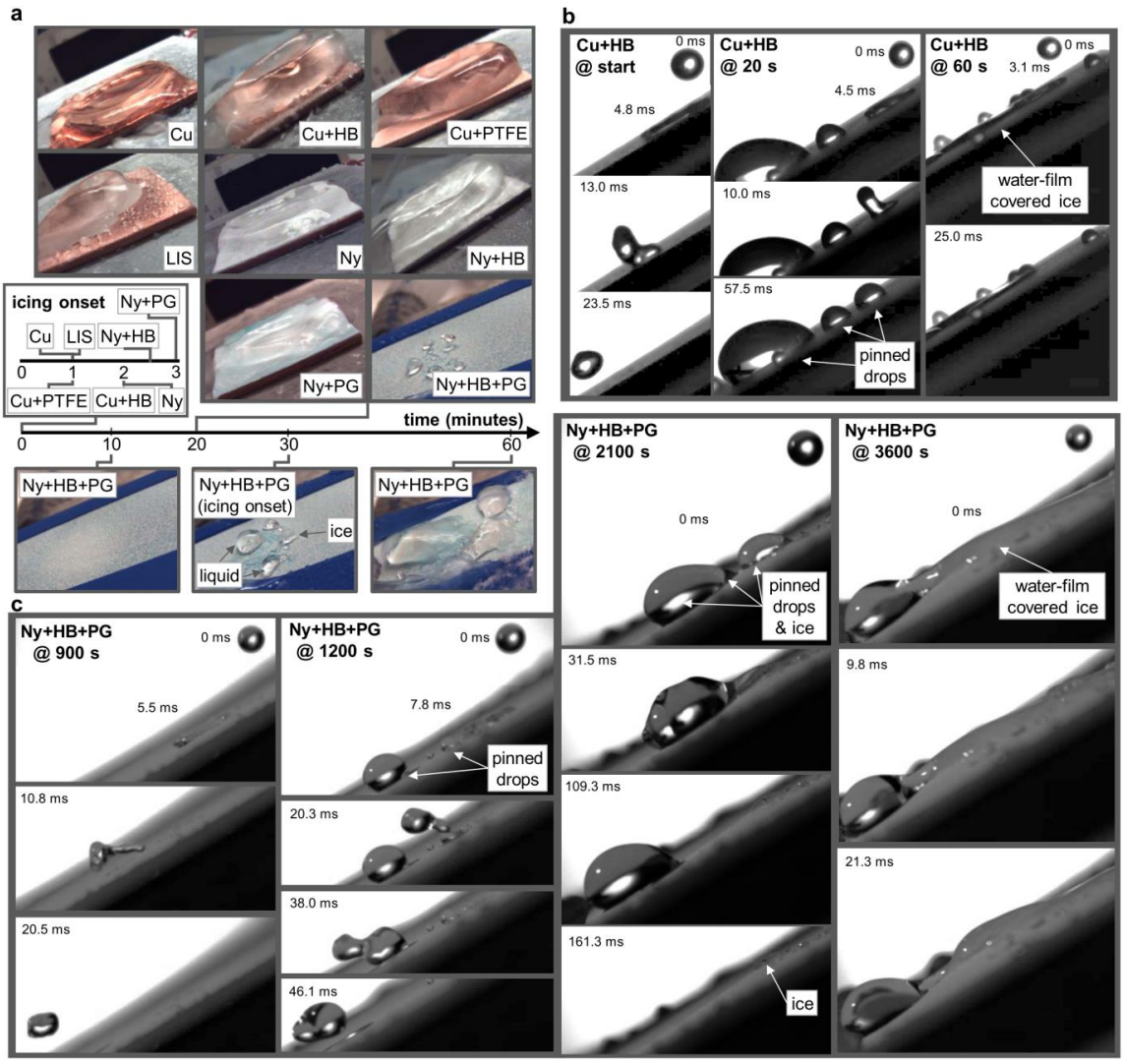

Figure 2.4 (a) Results of simulated freezing rain experiments showing images of all surfaces 20 minutes into the experiments as well as of the Ny+HB+PG surface after 10, 30, and 60 minutes after start of the experiment. Icing onset (i.e., the time that presence of ice was first observed on the surface) is also indicated for all surfaces; (b) and (c) sequence of images taken at 4000 fps showing drops impacting onto (b) Cu+HB and (c) Ny+HB+PG samples at different time intervals during the freezing rain experiments. Time starting from ~1 to 2 ms prior to impact is indicated in milliseconds within the images.

To provide an insight into the glaze growth dynamics drop impact onto the Cu+HB and Ny+HB+PG samples during different stages of the freezing rain experiments was also imaged using high speed camera. The images in Figure 2.4b show that, instead of bouncing away from the sample as at the start of the experiment, drops hitting the surface after 20 s of the experiments were pinned to and began to accumulate on the surface. These drops are likely pinned to the Cu+HB surface because of surface condensation,[73] which causes formation of capillary bridges through coalescence between the large impacting and much smaller condensed "satellite" drops.[74] Within 60 s of the experiment an ice film grew at the bottom of the pinned drops. Its formation is evident from the dramatic switch in drop impact dynamics. In particular, sequence of images in Figure 2.4b shows that after 60 s of the experiment drops hitting the Cu+HB sample do not recoil but merge with the existing water and ice film. After the impact a capillary wave travels down the water film causing some of the liquid to drain from top of the ice layer. The presence of antifreeze not only dramatically prolongs but also enables additional stages of the icing process to occur on the Ny+HB+PG samples. The images in Figure 2.4c show that even 900 s into the freezing rains experiments drops easily bounced away from the epidermis. Drop pinning and accumulation began after ~1200 s. However, antifreeze diffusion into the drops slowed ice nucleation. As a consequence, drops impacting the surface for the next ~900 to 1500 s were coalescing with and aiding shedding of majority of the accumulated liquid. Small patches of ice began to form after ~1800 to ~2100 s of continuous drop impingement. The ice film slowly expanded, covering most of the surface after ~3600 s of the experiment. At this stage, drop impact dynamics onto the water and ice covered Ny+HB+PG sample resemble those observed on the iced-over Cu+HB sample at 60 s.

2.2.3. Freezing Fog Experiments

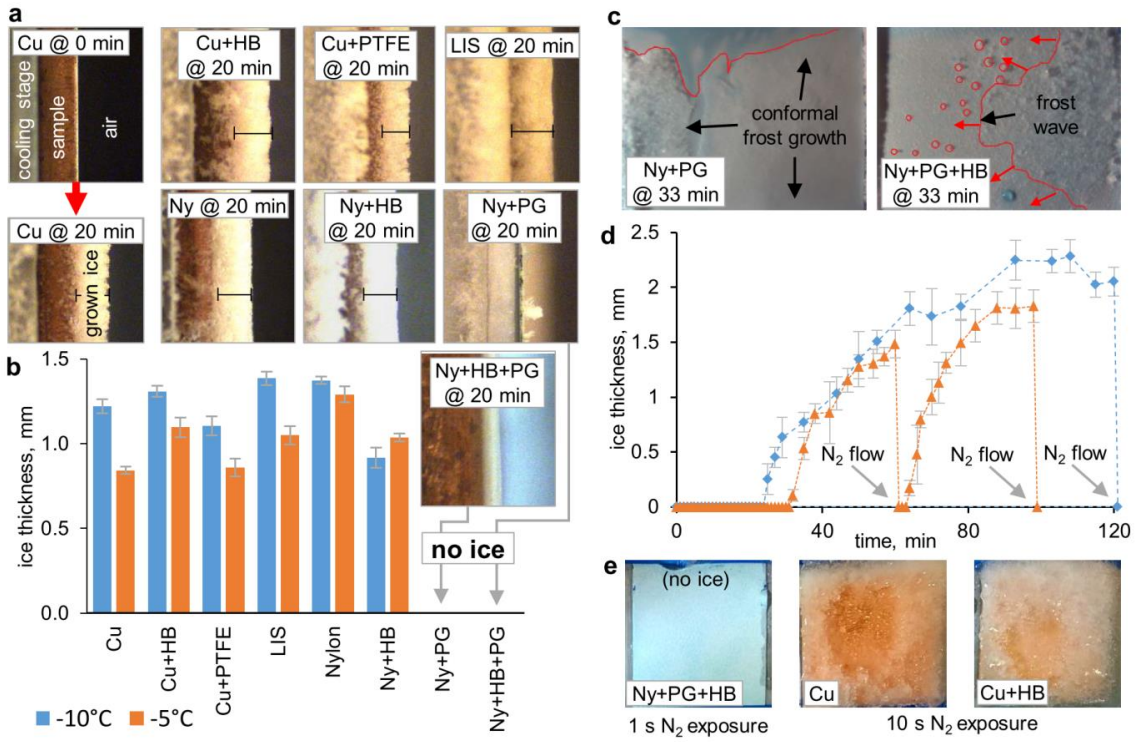

Figure 2.5 (a) Side-view optical images of vertically mounted samples at -10°C after 20 minutes of exposure to water mist (for reference, Cu sample is also shown prior to exposure), (b) histogram of average thickness of the ice accumulated in 20 minutes with sample surface temperatures of -5°C and -10°C, (c) top-down images of ice accumulated after 33 minutes on Ny+PG on Ny+HB+PG cooled to -10°C, (d) thickness of ice growing on Ny+HB+PG at -10°C as a function of time with nitrogen gas exposure points indicated, and (e) images of iced-over Ny+HB+PG, Cu, and Cu+HB samples after short exposure to pressurized nitrogen gas.

The histogram and images in Figure 2.5a and 2.5b show that 20 minutes of misting of samples cooled to -5°C and -10°C resulted in accumulation of about 1 mm of ice on all

surfaces without antifreeze. To facilitate optical measurement of ice thickness and to prevent accumulation of water around the edges, the samples were mounted vertically. On the Ny+PG and Ny+HB+PG surfaces we only observed formation of a liquid film within the first 20 minutes of misting. Onset of icing on these two surfaces was not observed for another 10 minutes of continued misting. Images in Figure 2.5c show the ice coverage of Ny+PG and Ny+HB+PG samples after 33 minutes of the simulated freezing fog experiments. Contrasting of these two images reveals that ice formation had begun uniformly throughout the entire Ny+PG surface but freezing on the Ny+HB+PG sample was initiated at the edge and on a few selected points throughout the surface. Subsequently, ice spread throughout the epidermis surface in a wave-like manner resembling frost-wave typically observed during condensation frosting on hydrophobic and superhydrophobic surfaces.[19,45,46] The plot in Figure 2.5d shows that after the frost-wave propagated through the surface rime-like ice accumulated on the Ny+HB+PG surface at a similar vertical growth rate as on the other surfaces (~0.05 mm/min).

Misting the Ny+HB+PG sample for 60 minutes increased ice thickness to ~1.5 mm. At this stage, the adhesion of rime grown on this surface to rime grown on Cu and Cu+HB was compared. It is noted that in contrast to glaze grown in inverted cuvettes,[13] to quantify the value of rime adhesion strength in this case in situ ice growth within refrigerated centrifuge is required.[21,27,48,75,76] Instead, rime adhesion strength on different surfaces was qualitatively compared by exposing the grown ice to dry nitrogen flow at a gauge pressure of 400 kPa. Images in Figure 2.5e show that the nitrogen flow could not remove the ice from the Cu and the Cu+HB within even 10 s exposure (at which point ice started melting) but it nearly instantaneous blew all of the ice off from the Ny+HB+PG surface.

Subsequently, the ice-free surface was re-exposed to the mist. In this case, ice regrowth was delayed by only 4 minutes and its thickness increased to 1.8 mm in the next 30 minutes. Further experiments showed that vertical ice growth rate decreased during extended mist exposure, reaching only a thickness of ~2.1 mm after a total two hours of mist exposure. Irrelevant of the rime growth time (up to tested 2 h), however, the adhesion of the ice to the Ny+HB+PG surface tested with the nitrogen flow did not change and remained minimal. Thus, the presence of antifreeze not only delays accumulation of rime, but it also dramatically reduces its adhesion to the surface.

2.2.4. Condensation Frosting Experiments

The images and histogram in Figure 2.6a and 2.6b show that within 20 minutes of condensation frosting experiments a 1 mm to 1.5 mm thick frost layer formed on all reference samples but not on the two antifreeze infused samples (Ny+PG and Ny+HB+PG). To investigate this trend further, we performed extended condensation frosting experiments. The top down images in Figure 2.6c show that while ice accumulation was significantly delayed in both cases, the frosting process proceeded in very different stages on the Ny+PG and Ny+HB+PG samples. In particular, on the Ny+PG sample, several patches of liquid film formed within the first 20 minutes. For this sample, a few millimeter sized ice crystals began to emerge out of these liquid patches after about 60 minutes of cooling. These crystals were surrounded by a light blue liquid film for an extended period of time and are referred to as ice-antifreeze solution slush. After about 90 minutes of cooling the liquid film was depleted and frost-like crystals began to rapidly emerge. In contrast, the Ny+HB+PG surface remained mostly liquid-free until about 80 minutes into

the cooling process. Subsequently we observed growth of small ice crystals within the liquid film. These crystals did get larger than 0.5 to 1 mm until ~100 minutes into the cooling process. At this point, growth of frost-like crystals over the entire sample was observed. The onset of this frost-like film growth is referred to as ice accumulation starting time. In addition to these experiments, frosting experiments with varied amounts of antifreeze infused per sample area were performed. This was achieved by layering multiple infused nylon membranes. The variation in the volume of the liquid per area is indicated by "1x", "2x", and "4x", referring to 1, 2, and 4 antifreeze-infused nylon membranes (for the Ny+HB+PG samples, only the top layer had the superhydrophobic coating). The histogram in Figure 6d summarizes the extended condensation frosting experiments, clearly demonstrating superior performance of the antifreeze-infused samples. Furthermore, the bioinspired bi-layer "skin" samples (Ny+HB+PG) delayed the onset of large ice crystal accumulation by 40 to 60 minutes when compared to the solely antifreeze-infused samples. While doubling the amount of initial antifreeze (i.e., from 1x to 2x) did increase the delay in both slush and ice accumulation, further doubling of the antifreeze amount (i.e., from 2x to 4x) did not cause proportional delays. In all cases, obvious secretion of the antifreeze, indicated by the light blue tint of the ice slush and later frost, was observed.

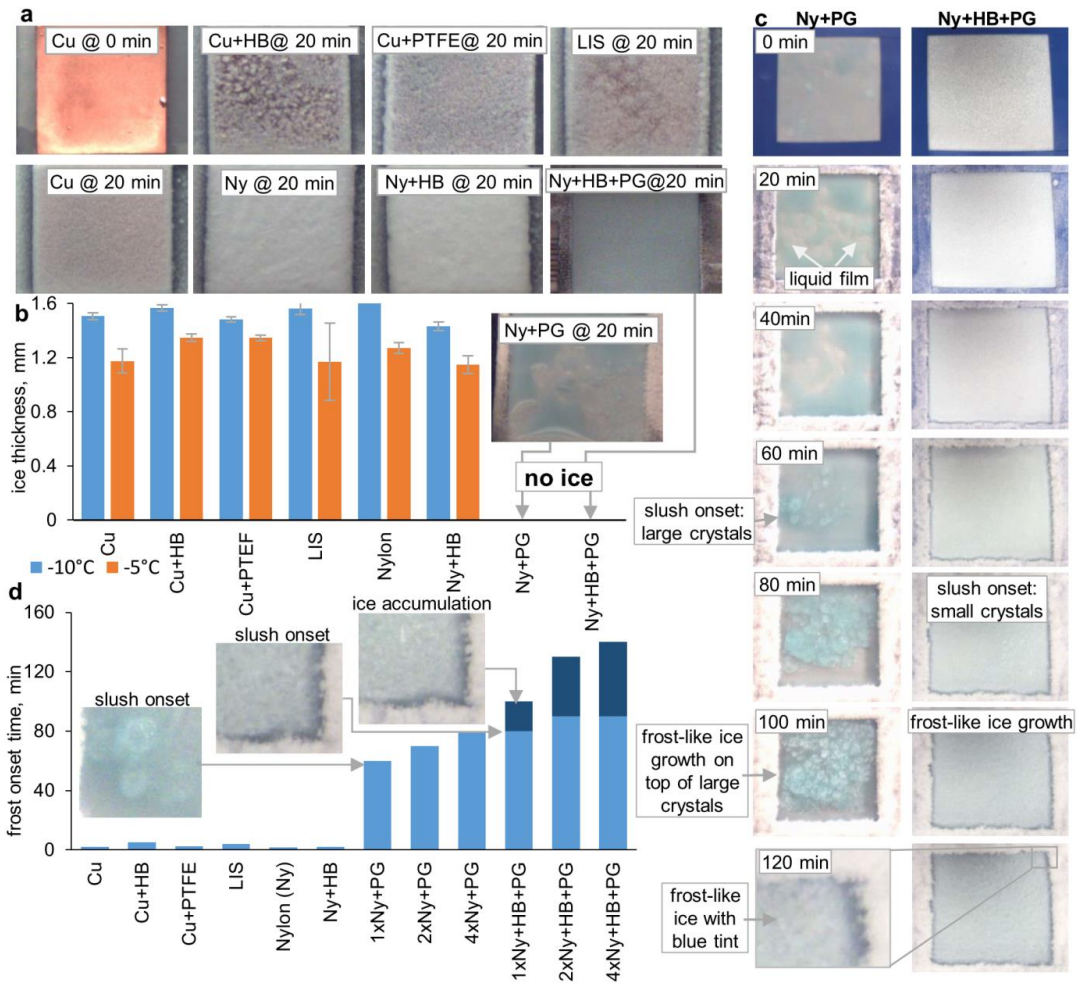
a
Cu @ 0 min
Cu+HB@ 20 min
Cu+PTFE@ 20 min
LIS @ 20 min
Cu @ 20 min
Ny @ 20 min
Ny+HB @ 20 min
Ny+HB+PG@20 min
b
ice thickness, mm
1.6
1.2
0.8
0.4
0
Ny+PG @ 20 min
no ice
-10°C
-5°C
Cu
Cu+HB
Cu+PTEF
LIS
Nylon
Ny+HB
Ny+PG
Ny+HB+PG
c
Ny+PG
Ny+HB+PG
0 min
20 min
liquid film
40min
60 min
slush onset: large crystals
80 min
slush onset: small crystals
100 min
frost-like ice growth on top of large crystals
frost-like ice growth
120 min
frost-like ice with blue tint
d
frost onset time, min
160
120
80
40
0
slush onset
slush onset
ice accumulation
Cu
Cu+HB
Cu+PTFE
LIS
Nylon (Ny)
Ny+HB
1xNy+PG
2xNy+PG
4xNy+PG
1xNy+HB+PG
2xNy+HB+PG
4xNy+HB+PG

Figure 2.6 (a) Top-down images of all samples after 20 minutes of cooling at -10°C in moist air at 60% relative humidity and 22°C, and (b) corresponding histogram of measured frost heights; (c) top-down images of extended testing in the same conditions testing of single layer ("1x") Ny+HB and Ny+HB+PG; and (d) histogram of frost "onset" time, which for samples without antifreeze this refers to the time that first water freezing was observed; for the Ny+PG this time refers to onset of slush formation, while for the Ny+HB+PG this time refers to first visible ice crystal formation within the liquid film. For the Ny+HB+PG sample time that substantial ice accumulation (uniform frost growth) was initiated is also indicated. To facilitate interpretation, antifreeze is dyed blue and the nylon membrane samples are taped down using either black or purple tape.

2.3. Conclusions

In summary, in this Chapter a novel type of anti-icing coating inspired by the functional liquid skin secretion in natural systems was introduced. This semi-passive coating consists of porous superhydrophobic epidermis and wick-like underlying dermis that is infused with antifreeze liquid. The outer layer serves as a barrier between the antifreeze and environment and, as a typical anti-icing superhydrophobic surface, easily sheds large sessile drops. However, in scenarios in which a typical SHS easily ices over, such as by pore penetration by high-velocity impacting drops or condensation frosting, the coating architecture responds by releasing stored antifreeze liquid. In general, the presence of antifreeze on the surface, with or without the epidermis layer, prevents the accumulation of all the studied forms of ice for a significantly longer time when compared to all other studied anti-icing coatings. The addition of the epidermis dramatically improved the

performance of the surface in freezing rain conditions. In particular, the experiments showed that slow condensation on this heterogeneous surface and antifreeze diffusion into drops slowed icing-onset and complete icing-over of the surface by a remarkable ~1000% and ~2000% as compared to the Ny+PG and rest of the samples (i.e., 30 and 60 minutes vs. <3 minutes). For the condensation frosting experiments, addition of the epidermis slowed both the icing-onset and complete icing-over of the surface by about 133% as compared to the Ny+PG (additional 20 to 40 minutes) and by at least 1600% as compared to all other samples (i.e., 80 minutes vs. <5 minutes). Furthermore, in contrast to the large ice crystals covering the Ny+PG surface, only a thin frost-like layer formed on the Ny+HB+PG coating. Icing-onset during the misting experiments was delayed by the presence of the antifreeze by ~600% (i.e., 30 minutes vs. <5 minutes) on both the antifreeze infused coatings when compared to the rest of the samples. The addition of the epidermis on top of the dermis had negligible effect on delaying freezing of the mist because of rapid merging of the impinging micro-drops with the condensate that flooded the pores. Condensate flooding of the pores also accelerated icing during the freezing rain experiments by increasing large drop adhesion to the superhydrophobic surfaces. However, the due to the heterogeneous nature of the Ny+HB+PG surface the condensation occurred much slower than on the Ny+PG sample providing additional delay in icing onset. Since high humidity leading to condensation is likely to occur along with freezing fog and rain, the experiments represent a conservative assessment of the anti-icing characteristics of the tested coatings. It was also observed that the release of antifreeze not only delayed icing of the surfaces, but also affected the ice morphology and significantly reduced its adhesion. The latter effect was likely caused by the presence of a thin lubricating melt layer between

the ice and the surface. The thin lubricating melt film could also help reduce nano/microscale topology abrasive erosion typically observed on superhydrophobic surfaces due to repeated deicing.[75]

CHAPTER 3

INHIBITION OF CONDENSATION FROSTING BY ARRAYS OF HYGROSCOPIC ANTIFREEZE DROPS

3.1. Introduction

It was shown in Chapter 1 that the nucleation rate can be exponentially decreased using two approaches: (1) by increasing the water contact angle of the surface and (2) by decreasing the water vapor concentration above it. Hydrophobic surfaces and SHS have been proposed as anti-icing coatings based on the first approach. However, Chapter 2 demonstrated that these surfaces are susceptible to frosting. In contrast, in this Chapter inhibition of frosting through modification of the water vapor concentration near the surface with hygroscopic liquids is studied. Recently Beysens and co-workers have explored the formation of frost around microscale NaCl salt crystals and salt saturated water drops.[64] Because the partial pressure of water at the hygroscopic liquid's surface is lower than P_{SAT}, the salt saturated water drop can act as a humidity sink and form a region of inhibited condensation (RIC), and with that condensation frosting, around it.[64–68] The RIC can also form during condensation around drop of the same fluid[65,66,68] as well as during nucleation of calcite crystals.[77] The plot in Figure 3.1b shows water vapor pressure above pure water, ice, salt saturated water, and propylene glycol-water solution (60%, 90%, and 99% propylene glycol by weight) in the temperature range of -40°C to 20°C. If the environment temperature is greater or equal to that of the substrate, all of these substances have water vapor pressure at their surface lower than P_{SAT} and thus act as humidity sinks.

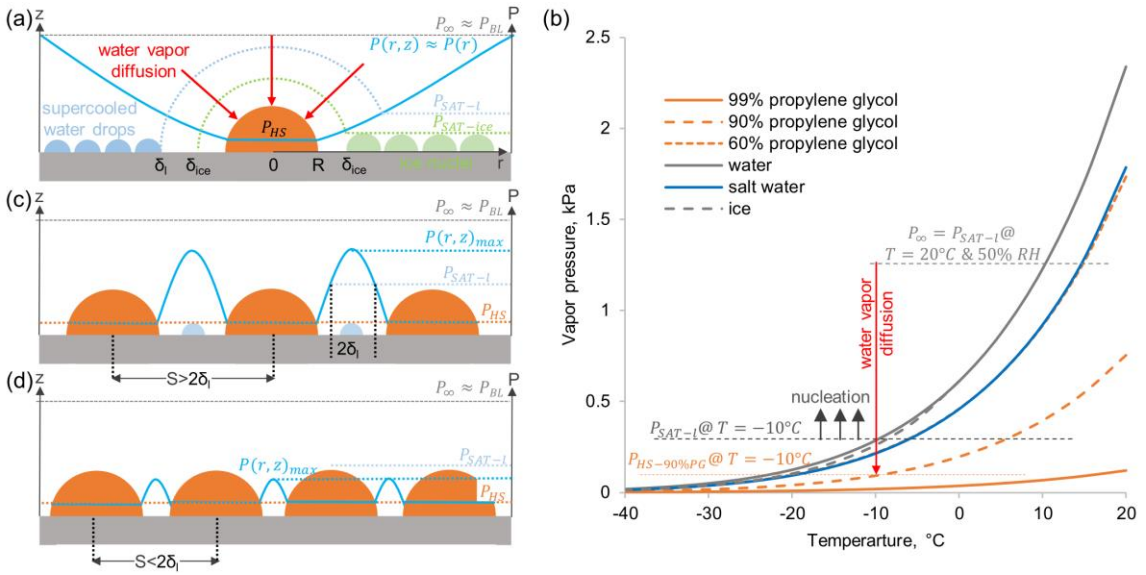

Figure 3.1 Illustration of condensation and frost nucleation inhibition using a (a) single hygroscopic drop, (c) multiple hygroscopic drops with S>2δ, and (d) multiple hygroscopic drops with S<2δ (i.e. overlapping regions of inhibited nucleation); and (b) equilibrium water vapor pressure above surface of water, ice, saturated water salt solution, and 60%, 90%, and 99% by weight propylene glycol water solution in the temperature range of -40°C to 20°C. PBL, δl, δice stand for partial pressure of water at boundary layer, and radii of water and ice RIC, respectively.

The size of the RIC can be estimated from radial water vapor pressure distribution around an isolated humidity sink with surface water vapor pressure (P_{HS}) that is below the water vapor pressure at infinity (P_∞). In quasi-steady state, the water vapor pressure profile around the hygroscopic drop with radius R is hyperbolic, $P(r) = P_\infty + (P_{HS} - P_\infty)R/r$.[64,65] Consequently, as schematically illustrated in Figure 2.1a, nucleation should be inhibited within region δ where $P(r) < P_{SAT}$ equal to $\delta/R \sim (P_{HS} - P_\infty)/(P_{SAT} - P_\infty)$. For example, for an isolated drop of 99% propylene glycol and salt saturated water (~23%

NaCl by weight) with R = 900 μm resting on a sample cooled to -10°C with air at 20°C and 50% relative humidity, $\delta/R_{99\%PG}\approx1.3$ and $\delta/R_{21\%NaCl}\approx1.1$. Consequently, only an array of hygroscopic drops could provide a scalable frost prevention technique.

The hypothesis is that frost formation can be significantly delayed over entire surface covered by array of hygroscopic drops that have center to center separation distance (S) smaller than 2δ (see Figures 3.1c and 3.1d). A closely spaced array of diethylene glycol (DEG) droplets was previously demonstrated to inhibit further nucleation of DEG drops over the array surface.[68] Analogous behavior was also reported for calcite crystal growth.[69] Furthermore, delayed condensation frosting due to integral effect of randomly spaced propylene glycol-filled micropores was implied by the work on responsive antifreeze releasing bi-layer anti-icing coatings presented in Chapter 2.[78] Since majority of common antifreeze substances such as salts (NaCl and $CaCl_2$), glycols, and alcohols are hygroscopic, exploiting the humidity sink array effect to delay frost formation could be possible. The hypothesis is tested experimentally by exploring how frost develops around individual and multiple drops of hygroscopic liquids deposited on a hydrophobic surface. Specifically, frosting dynamics around arrays of macroscale and microscale drops of salt saturated water and propylene glycol with average spacing below and above 2δ are studied. These two liquids are used as representatives of the two most common types of antifreezes, salts and glycols. Frost growth delay obtained using the humidity sink array approach is compared with the common ice and frost prevention technique, represented here through antifreeze films with volume equivalent to that of the drop array

3.2. Results and Ddiscussion

3.2.1. Sample Fabrication and Experimental Procedure

In order to assure about hemispherical shape of drops of both the liquids, a hydrophobic Polytetrafluoroethylene (PTFE) film was deposited on a silicon wafer. The silicon wafer (P type, 100 orientation from University Wafers) was cleaned by ultrasonicating it in a bath of acetone for 10 minutes and double rinsing it with purified water and acetone for 1 minute and drying in air. Next, the specimen was oxygen plasma cleaned for 3 min using Blue Lantern Nano BL1 plasma reactor with 250 mTorr and 50% power. Liquid Teflon precursor (Dupont AF amorphous fluoropolymer) diluted in FC-40 solvent (Sigma-Aldrich) to 20% by weight was spin coated on the wafer at 3000 RPM for 1 minute. The resulting thin film of PTFE was cured at 100°C for 1 h. The static, advancing and receding contact angles of water, salt saturated water, and propylene glycol (Sigma-Aldrich 99.5%) and water solution at different weight concentration were measured for at least six drops using a Rame-hart 290-U1 goniometer and are presented in Table 2.1. To make the saturated salt solution, excessive NaCl powder (Sigma Aldrich) was added into 20 mL of distilled water and stirred using magnetic stirrer for 1 hour. Afterwards, the salt saturated liquid was separated from the sediment.

Liquid	θ (°)	θ_a (°)	θ_r (°)
water	122 ± 1	126 ± 1	113 ± 1
salt saturated water	123± 1	127 ± 1	114 ± 1
99.5% PG	94± 1	94 ± 1	89 ± 1
80% PG	98 ±1	99 ± 1	89 ± 2

60% PG	102± 1	104 ± 1	94 ± 1
40% PG	107 ± 1	111 ± 1	99 ± 1
20% PG	113 ± 1	117 ± 1	107 ± 1

Table 3.1 Static (θ), advancing (θ_a), and receding (θ_r) contact angles of different studied liquids on the PTFE-coated silicon water. Percentage of propylene glycol (PG) in water solution is indicated in per weight terms.

The experiments were conducted under a Zeiss AXIO Zoom V16 high magnification optical microscope with Zeiss Apo Z 1.5x/0 lens with working distance of 3 cm connected to ETS 5518 environmental chamber using a custom built extension section made out of acrylic. The sample was cooled using a 6 by 6 cm peltier element (ATE-1-288-3AS from Analog Technologies), which in turn was cooled by flow of 4°C water using AP28R-30 VWR recirculating bath. The temperature on the surface of the sample was monitored using T-type thermocouple (Omega) and maintained constant by PTC-10 temperature controller (Stanford Research System). The entire sample and peltier assembly was placed in the custom made acrylic extension chamber. The humidity and temperature in the chamber was maintained at 50±2% and 23±1°C. Both of these quantities were monitored using the built-in sensors in the main environmental chamber as well as in close proximity to the sample using Sensirion SHT2x humidity and temperature sensor. The temperature of sample surface was initially maintained at 20°C and then reduced to -10°C at about a rate of 60°C/min. Imaging of the samples was commenced at the start of sample cooling and was continued until the samples were completely covered by ice. The images were analyzed using the Zeiss AxioVison and ImageJ software. The least square fits of the

collected results were performed using "NonlinearModelFit[]" function in Wolfram's Mathematica.

Six types of experiments were performed (I to VI). In type I experiment, a single drop with 0.2 µL, 0.5 µL, 1 µL or 2 µL volume was deposited on a sample. In type II experiment, four 2 µL droplets were placed at the corners of a 2 by 2 square lattice. In type III experiment, thirty 2 µL drops were placed on a 12 by 15 mm^2 sample in a 5 by 6 square lattice array. In type IV experiment 60 µL of either propylene glycol or salt saturated water was deposited on a 12 by 15 mm^2 piece of nylon filter (Nylon 66 Membranes from Supelco) to facilitate formation of a stable liquid film. The thickness of nylon was 70 µm, which was much smaller than the thickness of the liquid film above the nylon (~260 µm). In type V experiment we studied freezing of arrays of microscale droplets that were deposited onto 30 mm^2 samples using a beaker vaporizer. The sample was weighted before and after spraying of the droplets to determine quantity of deposited liquid. The densely and sparsely distributed drops corresponded to 0.017 mg/mm^2 (~20% surface coverage) and 0.0067 mg/mm^2 (~45% surface coverage), respectively. The propylene glycol droplets had initial average radius of 17 µm and were separated by, on average, 38 µm and 61 µm in the "dense" and "sparse" cases. In case of salt saturated water solution, the average radius and separation distance were 69 µm for the "sparse" case and 26 µm and 76 µm for the "dense" case and 14 µm, respectively. In type VI experiment, films of the antifreeze liquids with volume equivalent to that of the microscale drop arrays was deposited on a plasma cleaned silicon wafer without the PTFE coating. A nylon filter was not used in this case because the film thickness (~15 to 20 µm) was much smaller than the filter thickness. For all

experiments we studied frosting around drops of propylene glycol (initially at 99.5% concentration) and saturated salty water (~23% NaCl by weight).

3.2.2. Frost Growth Dynamics Around Individual Hydroscopic Drops

Figure 3.2 show representative results for type I experiment, in which isolated 0.2 to 2 μL drops of 99% propylene glycol and salt saturated water were placed at the center of a cooled PTFE coated silicon wafer. In general, radius of a drop growing via direct mass transfer from the vapor phase follows the generic power law $R(t) = R_0(1 + t/\tau)^{1/\alpha}$, where τ is a case specific time constant and α~2 and ~3 for isolated (hyperbolic pressure distribution) and multiple drops (linear pressure distribution), respectively.[65,69–72,79] Guadarrama-Cetina et al.[64,65] recently used scaling analysis to show that for an isolated drop of a hygroscopic liquid α~5. The growth of majority of the propylene glycol and salt saturated water drops we studied agreed with this scaling, following power growth law with α~5 to 6. For example, the illustrative drops of propylene glycol and salt saturated water in Figure 3.2, α=5.07±0.26 and α=6.2±0.33 (± one standard deviation). Considering that the environmental conditions in the experiments quickly begin to deviate from the idealized conditions used in the scaling analysis (e.g. formation of open frost dome described below), the agreement is reasonable.

While the growth of the original drops followed the expected growth law, some unique features occurred around the cooled propylene glycol drops. Specifically, right after cooling was initiated, formation of a condensation "halo" in the neighborhood of the propylene glycol drop was observed. This process occurred prior to condensation of drops anywhere else on the substrate, implying that vapor pressure of water was locally increased

near the drop. Consequently, the drop was likely rejecting absorbed water vapor as it was cooling to adjust the equilibrium value for given temperature (see Figure 3.1b). Similar halo formation process has been previously reported by Jung et al.[80] for cooled drops of pure water. However, after the temperature of the substrate was lowered to -10°C, the droplets condensed inside of the halo essentially ceased to grow. In contrast, once the temperature of the substrate was below 13°C to 14°C droplets rapidly condensed, grew, and started coalescing in the region outside of the original halo. Because of this markedly different droplet growth dynamics the halo area is referred to as the RIC. The images in Figure 3.2b show the vivid difference between condensate on the inside and outside of RIC after 5 minutes of cooling. The shown RIC has a radius of δ~1600 μm that remained nearly constant throughout the rest of the experiment. In fact, it was observed that value of δ remained nearly constant during the experiments for 0.2 μL, 0.5 μL, 1 μL, and 2 μL drops of both of the liquids (only differences was that we did not observe formation of stagnant drops within the RIC around salt saturated water drops). While at first puzzling, this trend can be explained using simple scaling analysis recently derived by Guadarrama-Cetina et al.[64,65] The authors derived an expression for δ/R in terms of the initial humidity sink pressure (e.g. salt saturated water) as $\delta/R \approx 1 + (\zeta/R)(R_0/R)^3((P_{SAT-l} - P_{HS@t=0})/(P_\infty - P_{SAT}))$, where ζ is the thickness of the mass transfer boundary layer. Rearranging this expression we obtain $(\delta - R)_{t=i}/(\delta - R)_{t=0} \approx (\delta_i - R_i)/(\delta_0 - R_0) \approx (R_0/R_i)^3$ and subsequently $\delta_i/R_o = R_i/R_0 + (\delta_0/R_0 - 1)(R_0/R_i)^3$. For a typical value of δ_0/R_0~1.5 in our experiments, enlarging of the drop to R_i/R_0~1.25 (maximum quantified value in our experiments) leaves the absolute RIC radius unchanged (δ_i/R_0~1.5). More intuitively, the plot in Figure 2c shows steady decay of the RIC radius scaled relative to

the drop radius (δ/R) towards the expected limit of 1 (i.e. no RIC when solution is completely diluted).

The frost growth process around the original drop proceeded in four stages illustrated in Figure 3.2d. The first stage consisted of freezing of the condensed supercooled drops outside of the RIC. This process was initiated within few minutes of cooling at the edges of the specimen and propagated in the previously described wave-like fashion.[19,44,64] A closer evaluation reveals some of the recently described intricate processes involved with the frost wave propagation. These include microdrop evaporation at the expense of dendrites growing from neighboring frozen drops and, in some cases, microdrop freezing due to contact with such dendrites.[19,44,64] The second frosting stage occurred after ~30 min when frost wave propagated around the entire RIC. Interestingly, after surrounding the RIC, growth of ice dendrites toward the drop was not only halted, but was in fact reversed. This occurred because P_{HS} for propylene glycol is much lower than $P_{SAT-ice}$ (see Figure 3.1b). At this point frost growth occurred primarily through vertical growth of dendrites, which eventually formed an open top frost dome around the original drop. Since this frost dome blocked top down visual access to the edge of the drop and the RIC, they could not be quantified both after ~80 to 90 min. Nevertheless, within the third growth stage the original drop grew at the expense of the surrounding open frost dome. For the propylene drop with original volume of 2 µL, this process proceeded for nearly 3 hours until the diluted drop came in contact with an ice dendrite and wicked into the frost (concluding fourth growth stage). The drop wicking times increased with the drop size, being for 50 min, 95 min, 180 min, and 240 min for the 0.2 µL, 0.5 µL, 1 µL, and 2 µL drops of propylene glycol drops, respectively. For the 0.2 µL, 0.5 µL, 1 µL, and 2 µL drops of salty water the drop wicking

times were 39 min, 86 min, 120 min, and 145 min, respectively. Right prior to wicking into frost, the studied drops had final R/R_0 of 1.35 to 1.5. This drop enlargement corresponds to dilution to 30 to 40% by weight of propylene glycol in the solution and 5 to 10% by weight of salt in the solution, respectively. For the propylene glycol, this diluted concentration range is above the freezing point concentration of 25% at -10°C. In contrast, at this temperature the freezing point concentration of salt-water solution is ~15%, explaining why formation of ice crystals was visible on some of the salt drops even prior to contact with the neighboring ice dendrites. In either case, the RIC exists until drop is diluted to near its freezing concentration when $P_{HS} \approx P_{SAT-l}$ (i.e. RIC exists longer for larger drops because it takes a longer time to dilute them to the freezing concentration).

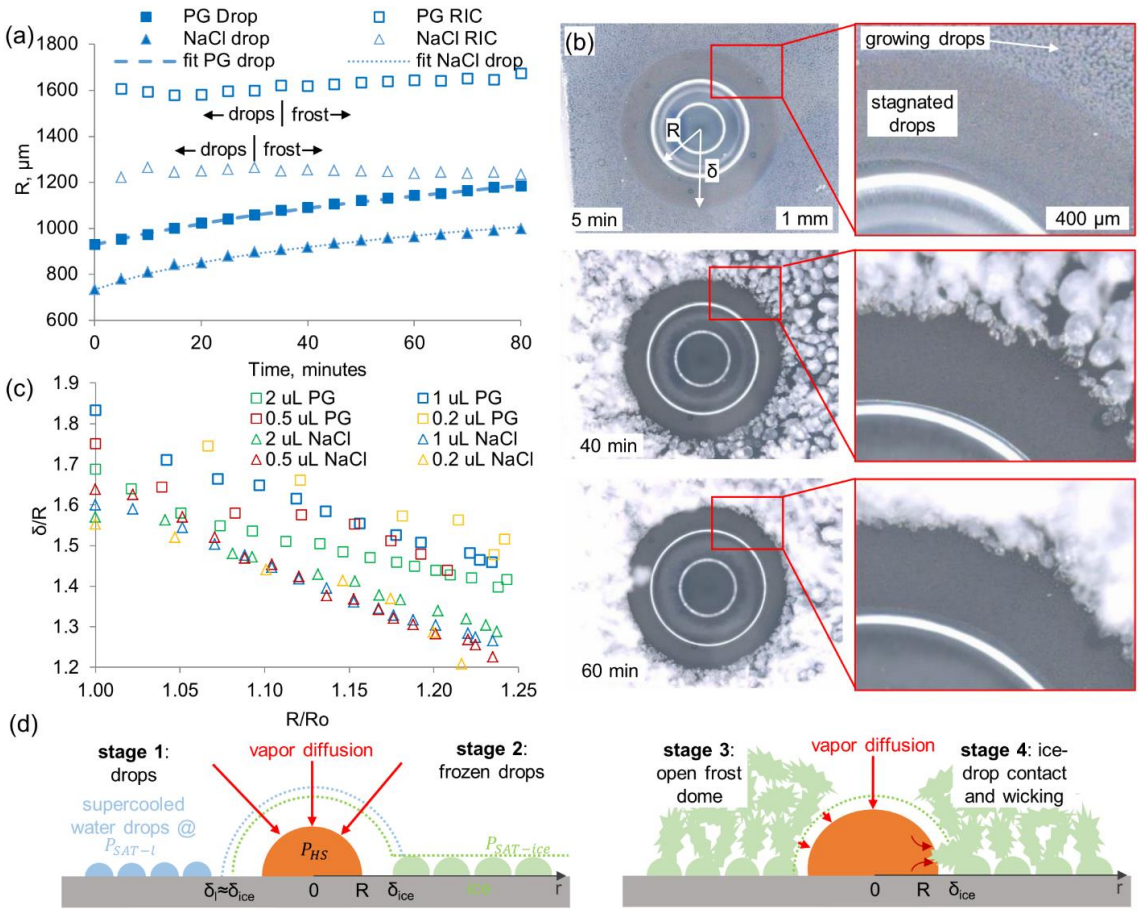

Figure 3.2 Representative frost growth dynamics around isolated hygroscopic drop: (a) plot of drop (R) and RIC (δ) radius vs. time for 2 µL isolated drops of saturated salt solution and 99% propylene glycol and (b) images corresponding to the latter, (c) plot of variation δ/R vs. of R/R0 for six different drops (PG-propylene glycol, NaCl-saturated water solution), and (d) schematic illustrating the four observed frost growth stages around hygroscopic drops.

3.2.3. Frost Growth Around Arrays of Hygroscopic Macroscale Drops and Hygroscopic Films

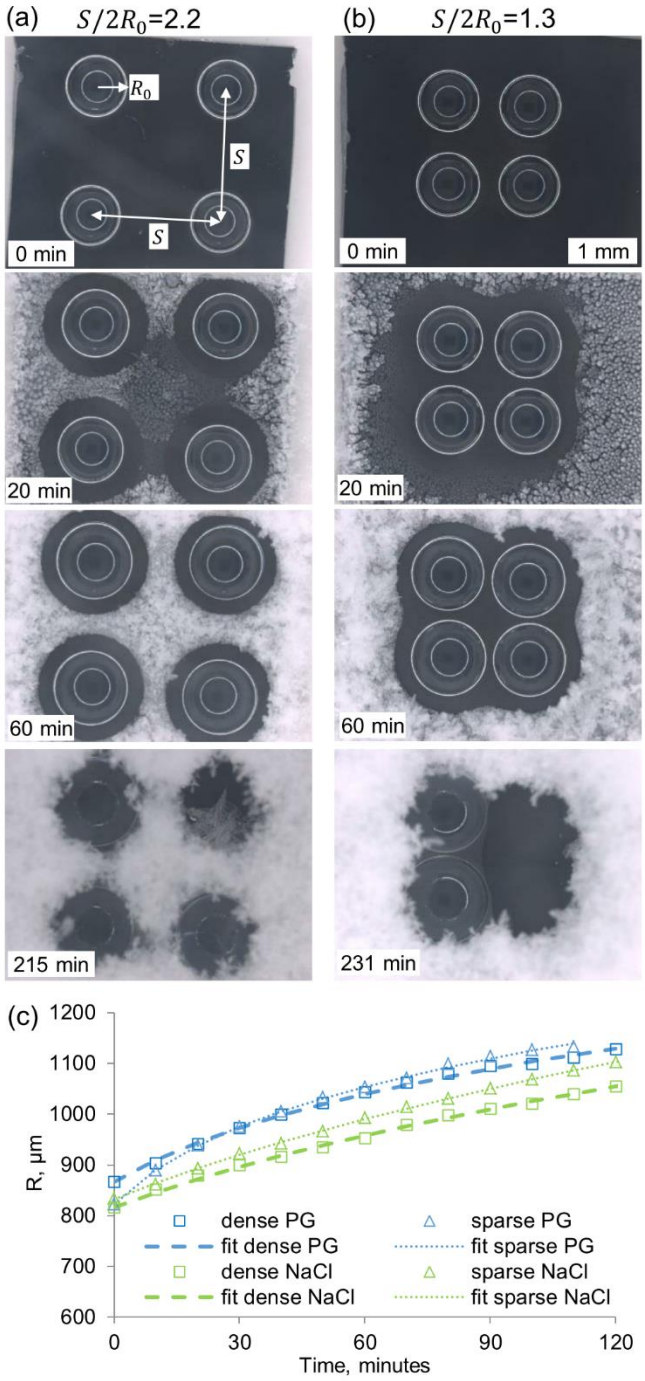

Figure 3.3 Images of condensation frosting around four 2 µL propylene glycol (PG) drops with (a) sparse separation of $S/2R_0$~2.2 and (b) dense separation of $S/2R_0$~1.3, and (c) corresponding plot of temporal evolution of the average drop radius (data for analogous experiment with four 2 µL drops of NaCl saturated water solution are also presented).

The crucial result from the frost growth experiments around individual microliter sized hygroscopic drop was that the size of the RIC remains nearly unchanged for extended periods of time. As a consequence, the area between two drops with $S < 2\delta$ should remain frost free until, at least, the two drops coalesce or are wicked away into neighboring frost. To test hypothesis type II frosting experiments were conducted with arrays of four 2 µL drops of propylene glycol or salt saturated water. This size of drops was selected because they provided the longest duration of the RIC. Since it was observed that for the given conditions δ/R_0 ($= 2\delta/2R_0$)~1.6 to 1.9, drop arrays with $S/2R_0$ ~1.3 to 1.6 and $S/2R_0$~2.2 to 2.6 were tested. The results presented in Figure 3.3 clearly show that while frost growth occurred in-between the sparsely separated drops it was completely inhibited in-between the densely spaced drops. A square RIC with round corners and edge width of ~2.2 S (~$6R_0$) was established around the drops. The sparsely spaced drops did not impact each other's growth, with the average radius following the power growth law with α=6.2±0.33. The average radius of the densely spaced drops followed the same trend with α=6.3±0.34, however, their proximity did impact each other's growth. Specifically, the centers of each of four closely spaced drops moved ~50 to 100 µm towards the center of lattice in the first 30 min of growth. Subsequently, the drop centers' movement reversed towards outside of the array. This behavior likely occurred because the partial water vapor

pressure is lower in the center of the square lattice (~P_{HS}) than on its perimeter (~$P_{SAT-ice}$). As a consequence, the pressure gradient, and with that the diffusive mass flux, is asymmetric (highest in the center of the square array). Because the drops are smaller than water capillary length (~2.7 mm) and have low pinning on the PTFE substrate, their shape is dominated by surface tension forces. Thus, rather than obtaining a non-symmetric drop shape, the drop centers moved. As in the single drop experiments, the inhibition of frost growth continued until the drops wicked away into the surrounding frost after coming in contact with ice dendrites, which occurred after around 230 min and 130 min of experiment for propylene glycol and salt saturated water drops, respectively. After wicking of the drops, frost rapidly propagated into the cleared areas. It is noted that the RIC remained frost free for about same period of time for the single and the four drop arrays (240 vs. 230 min for propylene glycol drops and 145 vs. 130 min for the salt water).

Encouraged by successful inhibition of frost within the smaller drop array, type III experiment, in which 30 drops of propylene glycol or salt saturated water, with 2 μL volume each, were placed in a 5 by 6 array with square lattice with $S/2R_0$~1.4 to 1.5 on a 12 by 15 mm^2 sample were conducted (see Figure 3.4a). The plot in Figure 3.4c shows that prior to first coalescence the average radius of propylene glycol drops increases according to the power law with α=6.5±1.5 (α=5.8±0.8 for salt saturated water). The average drop radius increased in a more quantized fashion after onset of the propylene glycol drop coalescence that occurred after 60 min of the experiment. For the drop array in Figure 3.4a, wicking of the first outer drops into the frost occurred after about 200 min. Immediately afterwards, frost propagated from the outer edge of the original array RIC to the edges of the new RIC posed by the rearranged remaining drops. This behavior continued throughout

the rest of the experiment, clearly highlighting the dynamic evolution of the RIC around the rearranging array. The last propylene glycol drops were overtaken by frost after a remarkable 480 min of cooling. The time for complete frosting over of the samples varied from experiment to experiment, being in the range of 6 to 8 h for propylene glycol and 2 to 4 h for salt saturated water drop arrays. The spread in the complete freezing times is due to small variations in drop arrangements that led to different coalescence patterns, and with that, wicking away times. Irrelevant of this variation, the presence of the array of antifreeze drops dramatically delayed icing of the samples, which without any antifreeze completely frosted over in just 7 to 8 min.

For comparative purposes type IV frosting experiments with films of the propylene glycol or salt saturated water solution with volume equivalent to that of the 30 drop arrays (i.e. 60 μL) were conducted. To ensure complete spreading of the film over the surface the liquids were deposited on a nanoporous nylon filter with thickness much smaller than that of the film (~70 vs. ~260 μm) with same base area as the 30 drop arrays. As in the previous experiments described in Chapter 2,[78] the filter was taped down on the side to prevent wicking of the liquid into surrounding frost and the antifreeze liquid was dyed blue to facilitate image processing. After start of the experiment, frost rapidly grew on the tape surrounding the filter and progressively extended over its edges. Since ice nucleation does not occur near the edges, it was concluded that the frost is overhanging the antifreeze film without coming into contact with it (consequently it is not counted towards ice coverage). The onset of ice nucleation on the propylene glycol films, indicating dilution to 25% by weight, occurs near the center of the filter after ~200 to 220 min. After onset of nucleation, slurry like ice spreads over the entire area occupied by the film. Gradually, frost-like

dendritic ice emerges from the slurry. In repetition of the film icing experiments, the entire surface area of the films was covered by ice within 200 to 320 min and 40 to 80 min for propylene glycol and salt saturated water films, respectively. The large scatter of the film freezing times occurs because of the random nature of the ice nucleation process (i.e. ice does not always emerge immediately after the film is diluted past the freezing point concentration). However, in all cases, the films iced over quicker than the drop arrays. In

particular, on average the propylene glycol and salt saturated water drop arrays delayed complete frosting over of the samples 1.6 and 2.8 times longer than the films, respectively.

An interesting aspect of the frost formation process that can be inferred from comparison of frosting in these two scenarios is that, despite twice higher surface area, the dilution rate of the array of drops is not faster than that of the equivalent film. This

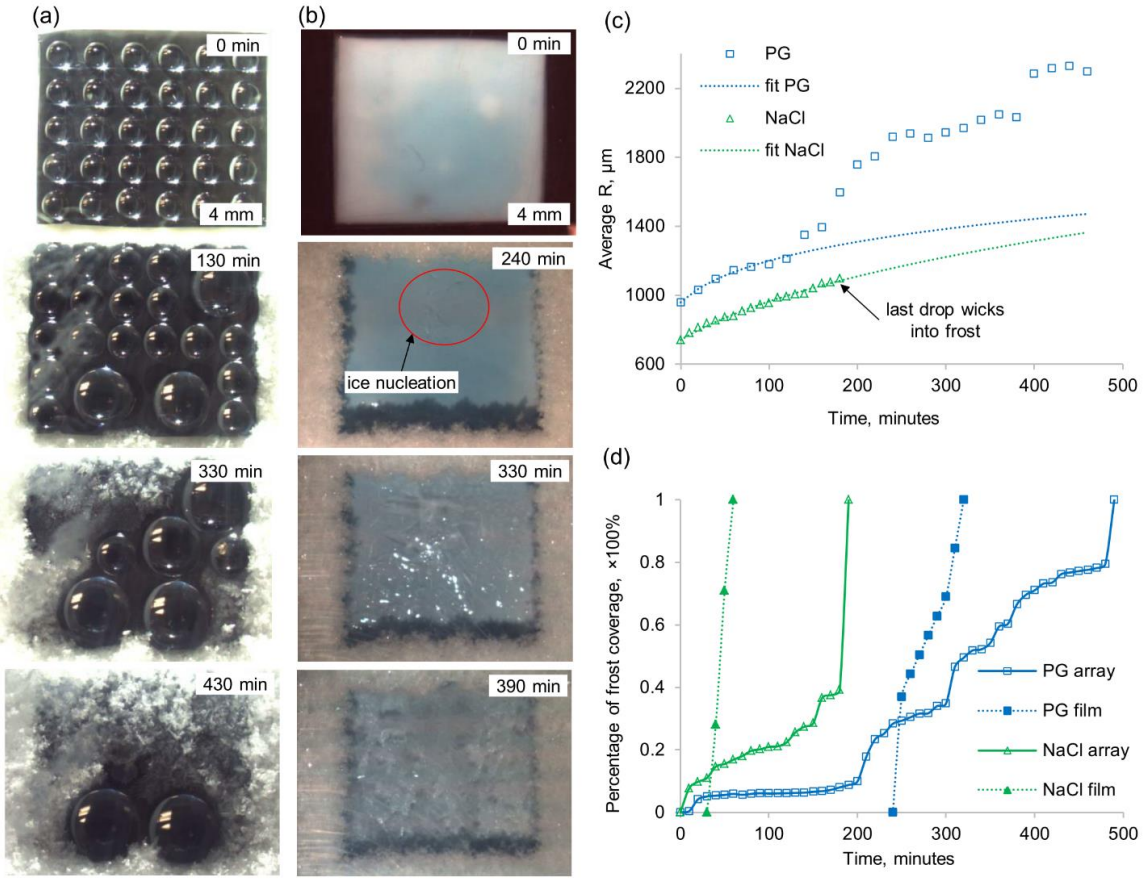

observation at first seems to contradict basic mass transfer principles: by doubling the low

Figure 3.4 Images of condensation frosting over (a) an array of 30 propylene glycol (PG) drops with $S/2R_0$~ 1.4 to 1.5, and (b) a film of 60 µL propylene glycol, (c) corresponding plot of temporal evolution of the average drop radius, and (d) frost coverage. Data for NaCl saturated water is also indicated in (c) and (d).

concentration (pressure) area of we do not increase the moisture diffusion rate from the

high concentration (pressure) region (in fact might decrease it since in Figure 3.3 nucleation for propylene glycol film occurred around 220 min while for drops some possible signs of ice nucleation within drops occurred around 440 min). To explain this phenomenon Comsol Multiphysics was used to simulate quasi-steady state vapor concentration distribution around drops within the array. Four different drop heat transfer scenarios within the drop were simulated. The resulting surface temperature profiles were used to obtain a temperature-dependent water vapor concentration around the drop surface. The results showed that when the boundary layer thickness is significantly greater than the drop and the RIC radii (i.e. > 5 mm), the mass transfer rate is nearly identical in the four simulated drop heating scenarios and in the planar film case. Since this boundary layer thickness is in agreement with values estimated for similar frosting scenario by Guardarrama-Centina et al.,[64] it is concluded that an increase in ice nucleation time with increase in the hydroscopic liquid surface area was not observed because boundary layer thickness is significantly greater than the drop radii. The further discrepancy between the ice nucleation time in film and in drops is likely due to random nature of nucleation dynamics.

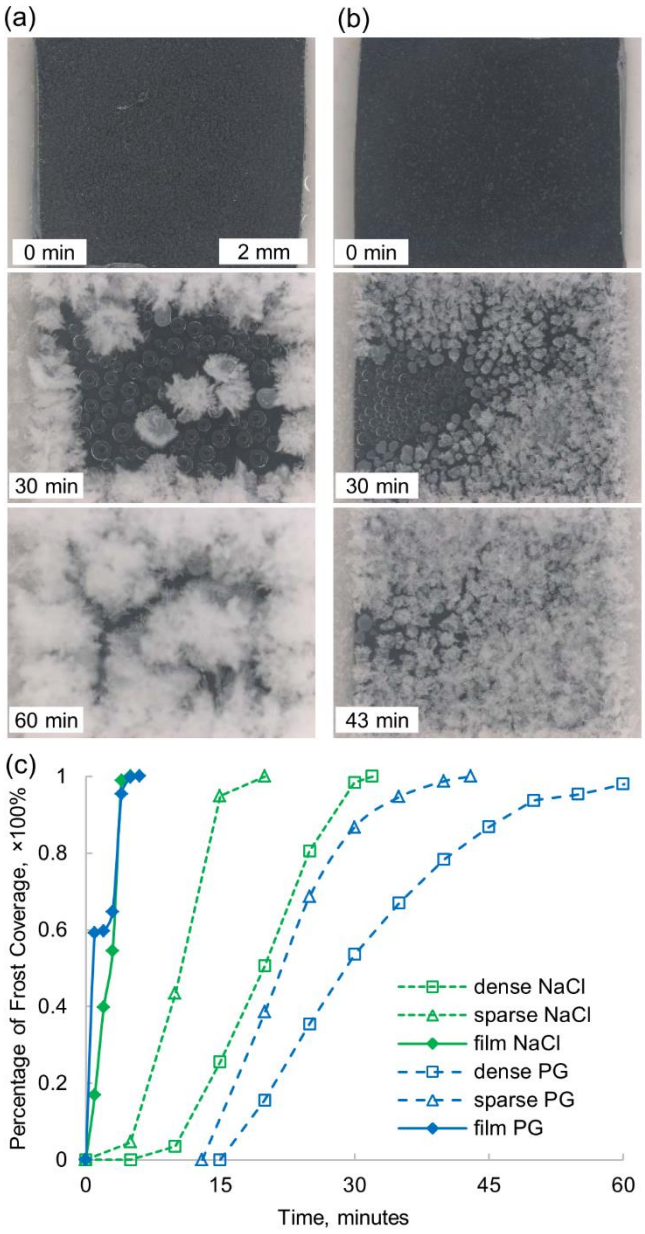

Figure 3.5 Images of frost propagation of microscale droplets of (a) salt saturated water and (b) propylene glycol (PG); (c) percentage of frost coverage corresponding to (a) and (b) as well as equivalent experiments with arrays salt saturated water microdroplets.

3.2.4. Frost Growth Around Sprayed Arrays of Hygroscopic Microscale Drops

From a practical point of view, to take advantage of the integral humidity sink effect induced by hygroscopic drop arrays, the drops would have to be sprayed instead of being dispensed individually onto the surface. This would result in randomly distributed arrays of microscale droplets with sizes smaller than those of pipette-dispensed drops that were studied in previous sections (minimum tested diameter was ~300 μm for the 0.2 μL drop as frosting around smaller hygroscopic drops was previously studied by Guadarrama-Cetina et al. [64,65]). To this end type V frosting experiments were conducted with two different areal densities of microscale propylene glycol and salt saturated water droplets deposited onto the PTFE coated silicon wafer using an atomizer. Figure 3.5 shows freezing dynamics of the sparsely and the densely distributed droplets with initial average radius to average spacing ratio of $S/2R_0$ ~1.1 and $S/2R_0$ ~1.8 for propylene glycol and of $S/2R_0$~1.4 and $S/2R_0$~2.4 for salt saturated water solution, respectively. In all cases, for the first 7 to 10 min the original droplets grew rapidly through further condensation and coalescence. Subsequently, a frost wave initiated at the sample edges began to percolate towards the center. For the sparsely distributed droplets, the frost wave propagated in a typical manner previously reported by Guardarrama-Centina et al.[65] and Boreyko et al.[44] Its propagation was significantly slower in the case of the densely spaced drops, which enabled their significant enlargement. Consequently, the large drops were diluted below the freezing concentration and began to freeze in the center of the sample prior to contact with the frost wave edge. Overall, this resulted in alteration of the freezing dynamics from "outside in mode" for the sparsely separated droplets to mostly "inside out mode" for the

densely separated droplets. The plot in Figure 3.5c shows that the samples covered by the sparsely and densely spaced propylene glycol droplets were on average frosted over within 45 min and 62 min, respectively. The corresponding values for salt saturated water solution were 21 min and 31.3 min. For comparative purposes type VI frosting experiments were conducted with films of both liquids spread over hydrophilic silicon wafer with volume equivalent to the sprayed drops. The propylene glycol and salt saturated water films equivalent to dense drop arrays completely frosted over on average in 6.3 min. For reference, frosting experiments with bare PTFE covered sample, which frosted over in ~7 min, were also conducted. In other words in both cases the denser arrays of droplets delayed complete frosting over of the samples 1.4 to 1.5 times longer than the sparsely spaced droplets. The denser arrays of droplets also delayed icing over of the surface 5 and 10 times longer than equivalent saturated salt water and propylene glycol films.

3.3. Conclusions

In this Chapter condensation frosting dynamics in presence of macroscopic and microscopic hygroscopic antifreeze droplets were explored. Guardarrama-Centina et al.[64,65] recently demonstrated that if the water vapor pressure at the hygroscopic liquid's surface is lower than the saturation pressure at the sample surface, a region of inhibited condensation (i.e. RIC), and with that frosting, occurs around the individual microscopic droplet of the liquid. It was first demonstrated that, as for microscopic drops, [64,65] for macroscopic droplets (R_0 >300 μm) of propylene glycol and salt saturated water the absolute RIC size remains essentially unchanged with δ/R_0~1.5 to 1.8 for R/R_0<1.25. Since the growth of the macroscopic drops follows the power growth law with α~5 to 6,

increase to R/R_0~1.25 can take a substantial time (e.g. 2 h for 2 µL drop). Within ~20 to 30 min a frost wave initiated at the outer edges of the sample percolated through the RIC. However, because $P_{SAT-ice} < P_{HS}$, propagation of ice dendrites was reversed at the edge of RIC. It was observed that the RIC was not only confined to the sample surface, but also expanded into three dimensions resulting in frost eventually growing into an open-dome like shape around the drop. Eventually the drop was diluted past $P_{SAT-ice} > P_{HS}$ and the liquid wicked into frost after coming in contact with one of the extending ice dendrites. For the 2 µL drop of propylene glycol this occurred after a remarkable 3h.

Utilizing the observation that the size of the RIC remains unchanged for prolonged periods of time, it was demonstrated that frost formation can be completely inhibited in-between small and large arrays of propylene glycol and salt saturated water drops with $S/2R_0$~1.3 to 1.6 (< 2δ). It was found that on average the arrays of macroscopic propylene glycol and salt saturated water drops delayed complete frosting over of the samples 1.6 and 2.8 times longer than films of the liquids with equivalent volume, respectively. In turn, it was shown that dense arrays of sprayed microscale droplets with $S/2R_0$~1.1 to 1.4 delayed complete frosting over of the samples 1.4 to 1.5 times longer than the sparsely spaced droplets with $S/2R_0$~1.8 to 2.4 and 5 to 10 times longer than films with volume equivalent (to denser arrays). In addition, due to the integral humidity sink effect frost wave propagation into the densely spaced microdroplet array was significantly slower than for the sparsely spaced microdroplets. This resulted in a major alteration freezing dynamics from “outside in mode” for the sparsely separated droplets to mostly “inside out mode” for the densely separated droplets. Thus this Chapter demonstrates that the integral humidity

sink effect of array of hygroscopic drops with $S < 2\delta$ can be exploited to get better antifrosting performance out of a fixed volume of hygroscopic antifreeze.

CHAPTER 4

SPATIAL CONTROL OF DROPLET AND FROST NUCLEATION USING ENGINEERED INTEGRAL HUMIDITY SINK EFFECT

4.1. Introduction

The onset of frost growth can occur through direct desublimation and condensation of droplets followed by their freezing, which is known as condensation frosting.[9,81] In both cases the nuclei formation rate per unit area, I, can be expressed according to Becker-Döring embryo formation kinetics as:[81,82]

$$I = I_0 \exp(\Delta G_c / kT_{sur}) \quad \text{(Eq. 4.1)}$$

where I_0 is the kinetic prefactor, ΔG_c is the critical Gibbs energy change for nucleation, T_{sur} is temperature of the surface, and k is the Boltzmann constant. At the critical embryo size, r_c, ΔG_c equals:

$$\Delta G_c = \frac{4\pi {\sigma_{ij}}^3 {V_m}^2 \left(2-3cos\theta+cos^3\theta\right)}{3\left(\bar{R}T_{sur} ln\left(\frac{P}{P_{sat}}\right)\right)^2} \quad \text{(Eq. 4.2)}$$

Where θ is the contact angle of the embryo in contact with the solid (subscript s) and subscript i and j correspond to either vapor or liquid state of water, $\bar{R}$ is the ideal gas constant, and V_m is the molar volume of the liquid, P is the partial pressure of water vapor in the surrounding, and P_{SAT} is the water vapor saturation pressure corresponding to the surface temperature. Eq. 4.1 and 4.2 imply that frost formation can be significantly delayed (i.e. nucleation rate decreased) by increasing θ. Since it only requires modification of the surface chemistry, this approach to frost inhibition has been studied in depth.[58,60,83–88] To surpass limits of hydrophobicity induced by chemistry alone, nanoscale and microscale

surface texturing has been used to develop superhydrophobic anti-frosting surfaces.[30,44–46,61,89–96] However, the macroscopically high contact angle of such surfaces (>150°) does not necessarily translate into decrease in nucleation rate below the rate for flat hydrophobic surface predicted by classical nucleation theory because nuclei can form in-between the surface features[15,35,97] or follow alternative growth pathways.[38,39,41–43] On some superhydrophobic surfaces, however, frost growth can be delayed through alternative physical mechanisms such as condensate ejection upon coalescence.[44,46,74,89,91,98–101] Another approach for spatial control of vapor nucleation is disruption of a hydrophobic surface with hydrophilic patterns onto which droplets condense preferentially.[14,92,102,103] Boreyko and co-workers[81,104,105] recently demonstrated that by intelligently spacing the hydrophilic areas dry zones in-between condensed droplets can be created. This clever trick stops the spread of frost by preventing ice-bridging in-between of individual droplets. While promising, it is unclear if this effect can be used to inhibit frost in industrial setting where hydrophobic areas are prone to physical damage.

In addition to decreasing surface wettability, Eq. 4.1 and 4.2 suggest that the onset of frost formation can be significantly delayed through decrease of the nucleation rate via local reduction of the water vapor pressure above the surface. This task, however, is significantly more difficult to achieve than engineering of surface wettability and has only recently been explored. Guadarrama-Cetina et al.[64,65] demonstrated that water vapor pressure can be locally decreased below the saturation pressure through presence of a hygroscopic liquid. Specifically, the authors have shown that a region of inhibited condensation and condensation frosting (RIC) forms around a water drop saturated with salt. The water vapor concentration at the surface of this hygroscopic liquid C_{HS} (from ideal

gas law equal to $P_{HS}/\bar{R}T_{HS}$=$P_{HS}/\bar{R}T_{sur}$) is lower than C_{SAT} which leads to formation of a "humidity sink" and decreased water vapor concentration in its vicinity. The existence of RIC was also described during condensation of water[106,107] and other hygroscopic liquids[108,109] as well as during nucleation of calcite crystals.[110] In previous Chapter it was shown that a significant delay in surface frosting can be achieved by arranging drops of hygroscopic liquid in an orderly array so that the individual RICs overlap.[109] Such integral humidity sink effect was also implied by long delay in condensation observed on bi-layer antifreeze infused anti-icing coatings described in Chapter 2.[111] To reiterate, this surface delays formation of glaze and rime by repelling impacting drops and, once the pores are flooded, counteracts formation of frost through diffusive release of the antifreeze liquid. Both the observed long delay in frost formation as well as pinning of impinging drops during freezing rain as compared to a superhydrophobic surface implied that water vapor distribution was altered above the surface. Analogously to a drop of hygroscopic liquid, the image in Figure 4.1a shows that a pore in a hydrophobic film filled by the liquid also creates a RIC in its vicinity. Contrasting of images in Figures 4.1b and 4.1c clearly demonstrates that, as with arrays of hygroscopic drops,[109] overlapping of the RIC of individual pores leads to inhibition of nucleation over the entire surface.

This Chapter focuses on laying the theoretical foundation and providing experimental validation of the mass transport mechanism that governs the integral humidity sink effect based on the bi-layer hygroscopic liquid infused coatings. A custom environmental chamber that enables quantitative comparison between the proposed theory and experimental results was developed. Utility of this chamber is demonstrated with validation of scaling laws previously developed for the size of RIC around an isolated humidity sink

(drop or pore). Next, model previously developed for calculation of heat spreading resistance is extended to model the current problem. It is used to demonstrate that the condensation onset temperature on the pore array is governed only by properties of the hygroscopic liquid, the source water vapor concentration, and the non-dimensional pore size and ratio of the pore spacing to boundary layer thickness. It is show that as the latter ratio decreases with pore array length scale change to microscale and below, the entire surface concentration becomes uniform and equal to the concentration set by the humidity sink. In other words, the surface concentration becomes completely independent of the non-dimensional pore size. The threshold geometrical parameters for this condition are identified. It is shown that this condition leads to dramatic decrease in nucleation onset surface temperature. With this new fundamental insight, it is demonstrated how the bi-layer surfaces can be designed to engineer the integral humidity sink effect to provide a scalable and robust anti-frosting coating.

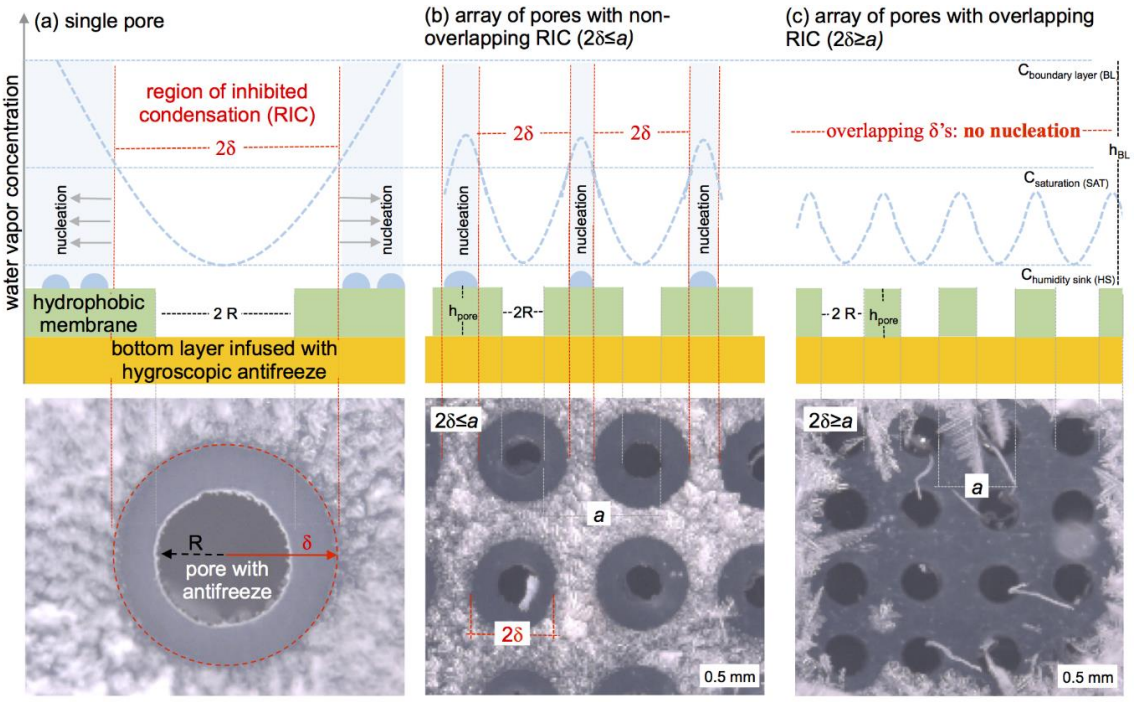

Figure 4.1 Schematics and images of nucleation and condensation frosting inhibition on a hydrophobic membrane with (a) an individual pore with diameter of 500 μm and (b & c) 4 by 4 square pore array with (b) non-overlapping regions of inhibited condensation and condensation frosting (RIC) due to pore spacing, a, being larger than size of RIC ($a \geq 2\delta$), and (c) overlapping RIC (i.e. $a \leq 2\delta$); in this case condensation frosting is completely inhibited in-between the pores due to the integral humidity sink effect. In all cases the membranes are on top of a hydrophilic porous layer infused with propylene glycol antifreeze.

4.2. Sample Fabrication and Experimental Setup

4.2.1. Environmental Chamber

To facilitate analysis of the integral humidity sink effect, a custom environmental chamber schematically shown in Figure 4.3a was designed. This chamber was designed to

mimic the mass transport within a boundary layer where diffusion dominates the transport in the direction normal to the surface.[65] Specifically, the chamber was designed to inhibit natural convection (inherently it is a stable design with heated top and cooled bottom) and to provide a stable and well-controlled vapor source on its top. The chamber has acrylic sides, while the top 3 cm by 3 cm layer consists of a transparent Indium Tin Oxide (ITO) heater supporting a fully wetted cotton fabric. The heater is used to maintain a stable temperature of the inner side of the cotton fabric that is lowered and maintained using a water-cooled Peltier element. Omega CSi32 and SRS PTC10 temperature controllers were used to control the temperatures of the ITO heater and peltier, respectively. As shown in Figure 4.2, T-type thermocouples were used measure the temperature of the vapor source and the surface temperature of the sample. To provide top-down optical access, a round opening with 1 cm diameter was cut in the cotton layer. The distance between the cotton fabric (top) and the sample (bottom) is 5 mm. An acrylic spacer (5 mm in height) was placed between the top and bottom to hold the positions of thermocouple, sample and peltier.

To demonstrate that diffusion is the dominent vapor transport mechanism, calibration film condensation experiments onto a superhydrophilic copper oxide sample were conducted. The change in the height of the condensing film was measured as a function of time and compared the results to film thickness predicted from one dimensional diffusion calculations. To avoid artifacts associated with dynamics of condensation onset,[98] a uniform thin film of water (<0.2 mm) was deposited on the surface. The sample surface temperature was maintained constant at 5°C in all experiments, while the vapor source temperature was set to 20°C, 25°C, and 30°C in order to significantly vary the source vapor

concentration. Imaging Source camera (DFK 23UP031, 1.8–3.6 mm, 1/3") placed on the side of the chamber to record the water film growth onto the cooled samples. The water film height was extracted from the images through image processing using ImageJ software. The experimental results plotted in Figure 4.2b show that the thickness of the water film increased linearly with time for each of the imposed temperature differences. Using a linear fit to the experimental data, it was calculated the experimental film growth rates were 0.16 ± 0.011 mm/h, 0.25 ± 0.011 mm/h, and 0.4 ± 0.011 mm/h (95% confidence level) for the source temperatures of 20°C, 25°C, and 30°C, respectively.

Assuming one dimensional mass transport, the water flux from the source to the sample, J (mol m^{-2} s^{-1}), can be calculated using Fick's law as $J = D_{\mathrm{w}}\left(C_{source} - C_{film}\right)/H$ (D_{w} for simplicity was assumed to be constant at value of 0.248×10^{-4} m^2s^{-1}, 0.251×10^{-4} m^2/s, and 0.254×10^{-4} m^2/s at the average temperature between source and bottom $(T_{top} + T_{bottom})/2 = 12.5$°C, 15°C, and 17.5°C, respectively[112]). In quasi-steady state the change in the film height can be calculated as $h_{film}(\mathrm{t}) - h_0 = Jt/\rho_W M_W$ (where h_{film} is the temporal height of the film, h_0 is the original height of the film, t is time, M_W and ρ_W are molar mass and density of water. The plot Figure 4.2b shows excellent agreement between experimentally measured and predicted film heights. Furthermore, the predicted film growth rates for the source temperatures of 20°C, 25°C, and 30°C are 0.16 mm/h, 0.25 mm/h, and 0.37 mm/h, which is also in good agreement with the measured values. Thus, these calibration experiments demonstrate that, as intended, the mass transport in the chamber occurs predominantly through diffusion.

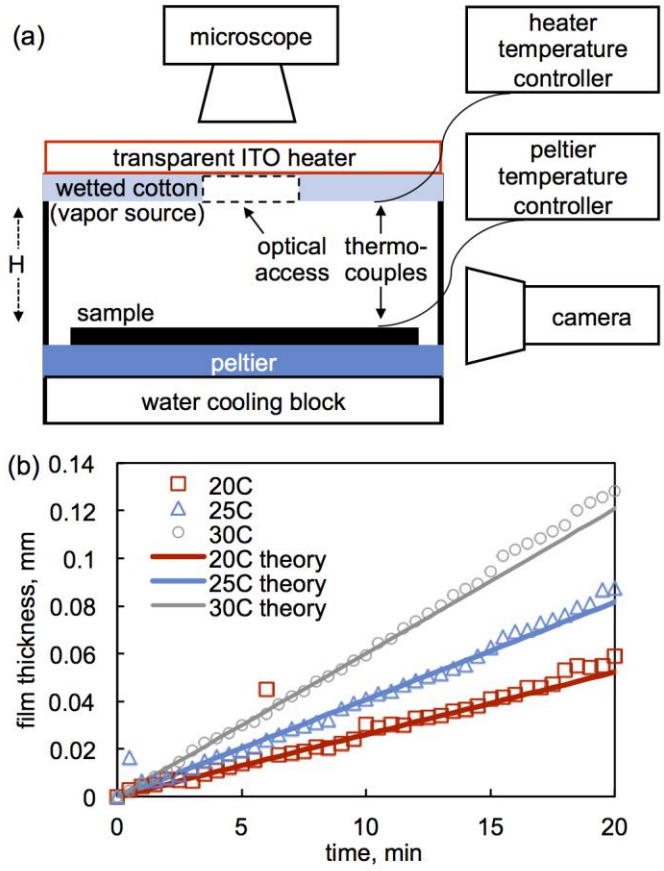

Figure 4.2 (a) Schematic of the designed environmental chamber and (b) plot comparing experimentally measured thickness of condensing water film on superhydrophilic copper oxide surface and same value predicted from one dimensional diffusion theory for three different source (wet cotton) temperatures of 20°C, 25°C, and 30°C with sample temperature at 5°C.

4.2.2. Sample Preparation

The superhydrophilic CuO samples for the chamber calibration experiments were fabricated according to procedure described by Liu et al.[113] Briefly, a mirror polished Cu plate (25.4 mm × 25.4 mm × 1.6 mm, McMaster-Carr) was ultrasonically washed for 10 minutes in each of the following solutions: 3.0 M HCl aqueous solution (Sigma-Aldrich), ethanol (VWR), and purified water (18 MΩcm from Nanopure Diamond purification system). The plate was then immersed in a sealed beaker containing 50 mL of 30 mM Ammonia (Sigma-Aldrich). The beaker was then left on hot plate at 60°C for 24 hours. After this time period, the plated was washed in purified water and dried in air. After this procedure, the plated was covered by a dark film of CuO, which consists of hierarchical nanostructures. The water contact angle on this surface was below 5°.

A PTFE film (20 mm × 20 mm × 0.05 mm, McMaster-Carr) was used to fabricate hydrophobic membranes with single pore and multiple pores with the unit cell size of 1 mm. The PTFE film was flattened with a rotational polisher and washed in ultrasonic bath for 10 minutes. AFM analysis showed the polished PTFE film had average roughness about 50 nm. SEM and EDS were used to confirm that the PTFE films were not affected by the polish procedure (i.e. no residual particles). The designs of the pore arrays were drafted using SolidWorks software. A laser cutter (Universal Laser System VLS 6.60) was used to fabricate pores in the PTFE film. The cutting-in-line resolution of this laser system was about 80 μm, producing smallest round pore with radius of about 80 μm.

In order to fabricate the membranes with unit cell size of 125 μm and 250 μm, metal meshes (McMaster-Carr) with this wire-to-wire spacing were dip-coated in PDMS

(Sylgard 184) diluted in cyclohexane (Sigma Aldrich). The ratio of PDMS curing agent, PDMS base and cyclohexane in weight was 1:10:10. The number of dip-coating steps was used to adjust the size of the openings. Meshes were cleaned through ultrasonication in ethanol and water for 15 minutes, respectively, followed by drying in air. Subsequently, meshes were dipped in the diluted PDMS for 10 seconds and then cured at 120°C for 20 minutes. To fabricate samples consisting of smaller size of pores, after cooling meshes in air to room temperature, the dip-coating process was repeated for up to 6 times. Lastly, the polycarbonate membranes containing pores, whose sizes were 10 nm, 30 nm, 50 nm, 100 nm, and 200 nm respectively, were purchased from Sterlitech (Table 4.1 for details). The static contact angle of polycarbonate membrane was ~ 80°. To render the top surface of the membrane hydrophilic, we sputtered ~10 nm of gold using Denton DC sputter coater. The static contact angle of the gold coating was <10°.

In order to determine equivalent parameters for a square grid array for the utilized polycarbonate membranes with randomly distributed pores, SEM images were processed and analyzed using Mathematica. The two geometrical parameters of interest, unit cell size (a) and non-dimensional pore size (b/a), can be determined from manufacturer provided information or direct image analysis. As shown in Table 4.1, the manufacturer provides information on the pore diameter, fractional exterior surface area (A_f), and areal density of the pores (N_p). It can be easily shown that for a square grid array $b/a = \sqrt{A_f}$ and $a = \sqrt{1/N_p}$. In addition, knowing the pore diameters, d, from manufacturer one can also calculate $b/a = \sqrt{d^2/N_p}$. However, not all of the relevant parameters are available (e.g. exact area fraction for 10 nm pores). Consequently, the equivalent unit cell size was

obtained from image analysis. Specifically, for a square grid array the unit cell size is also equal to the distance in between nearest pores. Since on a square grid each point has 4 closest neighbors, this was used as an alternative metric to determine a distribution for a. To obtain this value, the raw SEM images (see example in Figure S2a) were imported into Mathematica, and edges were detected using "EdgeDetect" function with Sobel method with the parameters adjusted to each image. Subsequently, the features were filled using "FillingTransform" function (see example image in Figure 4.3b) and individual components of the image were identified using "Morphological Components" function (see example image in Figure 4.3c). Once identified, the coordinates of the centroid of each of the components was computed using "ComponentMeasurements" function (see example plot in Figure 4.3d). Subsequently, the nearest 4 neighbors of each components were identified by iterating through the centroid value array with the "Nearest" function. The distance in-between each of the 4 closest neighboring points and the "center" pore were calculated using the "EuclideanDistance" function. To provide sufficient number of distance to define a distribution, data from at least three analyzed images was combined (duplicate values were removed). The histogram in Figure 4.3e shows an example distribution for the 200 nm pore membrane. The resulting mean values for all the utilized samples as well as the associated standard deviation are reported in Table 4.1 The values from image analysis are in close agreement with those obtained from calculations using the manufacturers data. It is noted that SEM imaging of the 10 nm pore samples proved to be challenging because the pore size is same as the size of gold grains used to ground the sample. Similarly, the pores are comparable size to tip of AFM cantilevers, making high quality imaging challenging. Consequently, for the 10 nm pore sample $b/a=\sqrt{d^2/N_p}$

definition was utilized, which was in good agreement with results from image analysis of all the other membrane pore samples.

Pored (um)[a]	Pore Density (pores/cm²)[b]	% Open Area[b]	$b/a = \sqrt{A_f}$	$a = \sqrt{1/N_p}$ (μm)	$\frac{b}{a} = \sqrt{d^2/N_p}$	b/a image analysis	a image analysis (μm)	Nominal Thickness (c) (μm)[b]
0.2	3 x 10^8	10	0.32	0.58	0.34	0.35±0.12	0.58±0.20	10
0.1	4 x 10^8	3	0.17	0.5	0.2	0.2±0.08	0.50±0.20	6
0.05	6 x 10^8	1	0.1	0.41	0.12	0.13±0.06	0.39±0.18	6
0.03	6 x 10^8	<1	<0.1	0.41	0.07	0.05±0.03	0.61±0.43	6
0.01	6 x 10^8	<1	<0.1	0.41	0.025	-	-	6

Table 4.1 Polycarbonate membrane geometrical information provided by manufacturer (http://www.sterlitech.com/pcte-product-and-performance-characteristics.html).[a.]Tolerance + 0%, -20% [b.] Tolerance +/-15%

To compile the bi-layer samples, the patterned membranes (PTFE, PDMS, or polycarbonate) were placed on a porous nylon 66 filter (30 mm × 30 mm, pore size 0.45 μm, Sigma-Aldrich as in our previous work[111]), which was previously infused by 100 μL propylene glycol (PG, 99%, Sigma-Aldrich).

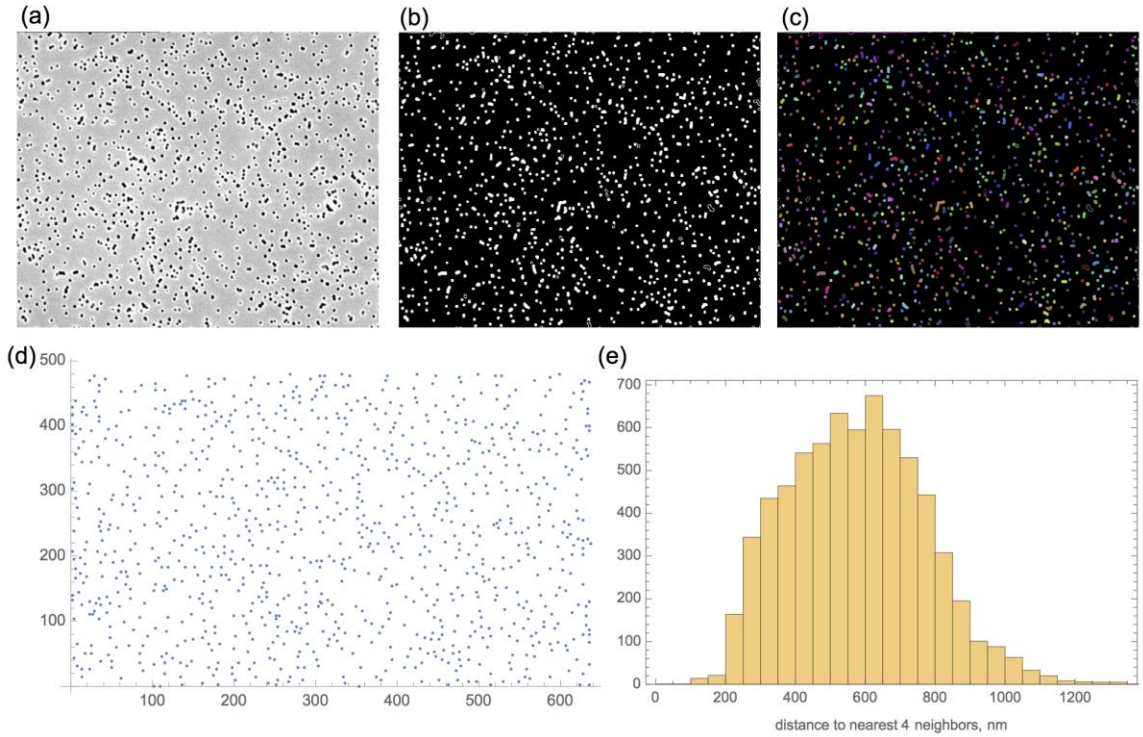

Figure 4.3 Example image processing and statistical analysis of 200 nm polycarbonate tract etch membrane pore density: (a) original SEM image (image width 22 μm), (b) image after edge detection, filling, and binarization, and (c) imaged of the colorized detected components, (d) plot of the location of the computed component centroids (in pixels), and (e) histogram of the distance between neighboring pores (4 closest neighbors analyzed) compiled from analysis of three SEM images.

4.2.3. Finite Element Simulations and Simulation Data Analysis

The mass transport problems schematically described in Figure 4.5a were numerically solved using Finite Element Method in Comsol Multiphysics software. To reduce the computational time, symmetry was used to simulate only a quarter of the full unit cell. Free

tetrahedral mesh with predefined “extremely fine” size adjusted to feature size geometry was utilized (a study was conducted to ensure mesh independence of the solution). For the case with fixed concentration at the pore surface, a parametric sweep was conducted to simulate the full range of b/a from 0.01 to 0.99 with values of a corresponding to the experimental range. The mass sink for each of these cases was determined from surface integration over the sink (which is equal to the top mass source) and was manually substituted into simulations of the corresponding fixed mass sink at the pore surface. The results of the dependence of non-dimensionalized mass sink value on the geometrical parameters (Figure 4.5c) were fitted using Wolfram Mathematica. Specifically, the “NonlinearModelFit” function was used with each pointed weighted with inverse of its 95% confidence interval. Similarly, all reported error bars correspond to the 95% confidence interval.

4.3. Results and Discussion

4.3.1. Inhibition of Nucleation, Droplet and Frost Growth Around Isolated Antifreeze Filled Pores

As drops of the hygroscopic liquid,[64,65,109] individual propylene glycol filled pores with radius of ~80 μm to ~550 μm are surrounded by region of inhibited condensation and condensation frosting (RIC). The plot in Figure 4.4a shows that this common non-toxic antifreeze liquid is also an excellent desiccant, with water vapor concentration above its surface lowered than that of supercooled water and ice for a wide range of concentrations. The images in Figure 4.4b shows that the size of RIC induced by the propylene glycol filled

pore remains nearly unchanged as the condensed water droplets freeze and transition into frost. Furthermore, it was found that the size of RIC is the same on membranes with hydrophobic Polytetrafluoroethylene (PTFE) and highly hydrophilic gold exterior, which confirms that condensation inhibition in this case is predominantly driven by vapor phase dynamics, not surface wetting properties (albeit the PTFE membranes do have a surface roughness on the order of 50 nm, which can encourage nucleation). Consequently, the size of the RIC, δ, should be dictated by the surrounding water vapor concentration field.

For an isolated slowly growing droplet of hygroscopic liquid with radius R surrounded by a stagnant isothermal semi-infinite medium, the quasi-steady state the water vapor concentration profile in spherical coordinates, $C(r)$, is hyperbolic.[114] Specifically, $C(r) = C_\infty + (C_{HS} - C_\infty)\, R/r$, from which it follows that the size of the RIC where $C(r) < C_{SAT}$ is $\delta = R(C_{HS} - C_\infty)/(C_{SAT} - C_\infty)$ (where C_{HS} and C_∞ are the water vapor concentrations at droplet surface and at infinity, in practice taken as the boundary layer thickness h_{BL}). This relation has been used to develop scaling laws for the evolution of the R/δ ratio and droplet growth, which qualitatively agree with experiments.[64,65,109] Despite the difference in pore and drop geometry, the analytical expression for the relation between δ and R derived from the hyperbolic function agrees well with the experimental measurements. It is important to note that the quantitative agreement between modeling and experimental results is enabled by use of our custom environmental chamber. In contrast to previous studies that were conducted in the presence of natural convection or forced flow,[64,65,109] the boundary conditions in this setup can be accurately captured in the theoretical formulation.

An important consequence of the near hyperbolic vapor concentration field around the pores is that the initial ratio R/δ is a non-dimensional constant equal to $(C_{SAT} - C_\infty)$

/ $(C_{HS} - C_{\infty})$ for fixed environmental conditions. Confirming this relation, the experimental value of R/δ=0.82±0.05 obtained from the slope of the line in Figure 4.4b matches closely the theoretically predicted value of 0.83. Furthermore, the plot in Figure 4.4c shows good agreement between experimental and theoretical values of R/δ for varied water source concentrations (achieved by changing the temperature of the water saturated cotton fabric, T_{∞}, on the top boundary, which increases the saturation pressure leading to increase in $C_{\infty} = P_{\infty}/\bar{R}T_{\infty}$). As the source concentration increases, the R/δ ratio approaches 1, implying that RIC ceases to exist. In turn, as the source concentration decreases, R/δ decreases and eventually as $C_{\infty} \rightarrow C_{SAT}$ vanishes (i.e. lack of a concentration gradient prevents mass transfer that feeds nucleation). From an applied perspective this spatial trend is beneficial as a large RIC would ensure inhibition of condensation frosting while the aircraft is ascending (assuming that rapid cooling of wing exterior leads to $C_{\infty} \sim C_{SAT}$). A reasonable value of R/δ of 0.91 to 0.77 should also exist during aircraft descend into majority of environmental conditions.

Naturally, the size of the RIC will decrease as the antifreeze solution becomes diluted (i.e. $R/\delta \rightarrow 1$ as $C_{HS} \rightarrow C_{SAT}$). However, a decrease of the RIC during the duration of any of the single pore experiments was not observed (after about 30 minutes frost nucleated outside the RIC started growing above the pore, making quantification of the δ impossible). This effect could be caused by the presence of a large reservoir of propylene glycol under the individual pore. Consequently, it is unclear if the trends observed for isolated pores are preserved when the water vapor and reservoir concentration fields are altered by presences of multiple pores arranged in well-defined geometrical arrays.

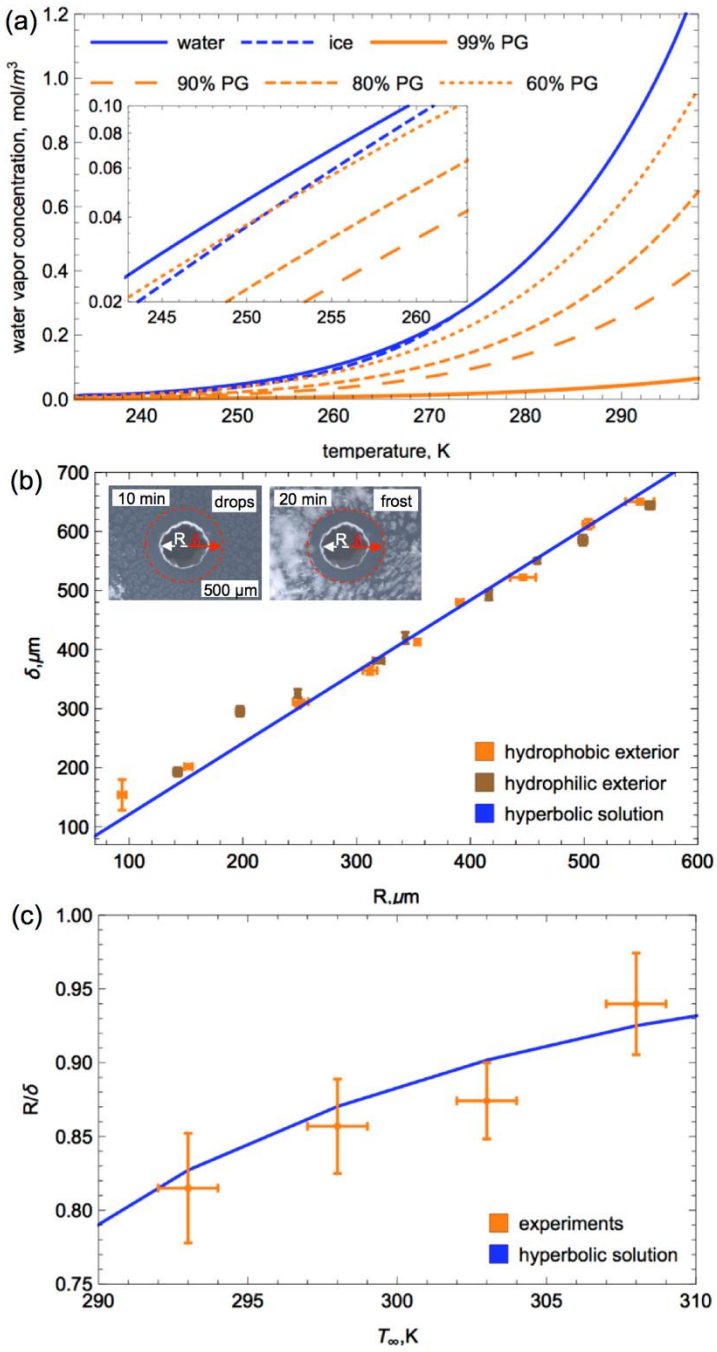

Figure 4.4 (a) Plot of water vapor saturation concentration above surface of water and ice as well as for several concentrations propylene glycol (PG) and water solutions

(concentration specified by weight) as function of temperature; (b) Plot of the measured and theoretically predicted radius of the circular regions of inhibited condensation and condensation frosting (circular RIC with radius δ) around isolated pores with radius R in membranes with hydrophobic and hydrophilic exterior surface cooled from to -6°C±2 with source temperature of 20°C±1, and (c) Plot of the measured and theoretically predicted R/δ ratio for different vapor source temperatures with fixed sample temperature of -6°C±2.

4.3.2. Inhibition of Nucleation, Droplet and Frost Growth by Arrays of Antifreeze Filled Pores

4.3.2.1. Theoretical Considerations

In the previous section it was demonstrated that the extend of the humidity sink effect around an isolated pore filled with propylene glycol can be quantitatively predicted from the hyperbolic quasi-steady state water vapor concentration field. Based on this result, it is assert that the integral humidity sink effect stemming from a pore array can be analyzed by evaluating the three dimensional concentration field, $C(t,x,y,z)$, above a single array "unit cell" with periodic boundary conditions with adjacent unit cells (i.e. no flux condition, see schematics in Figure 4.5a). The source of the water vapor is provided by a constant concentration on the top plane, C_{BL}, that corresponds to the edge of the boundary layer that is located at a height h_{BL} above the membrane plane ($z = 0$). For simplicity, the pore depth is neglected and a square pore with side length b centrally located within a square unit cell with side length a is analyzed. On the plane of the membrane mass transfer in the normal direction occurs only into the pore due to a water vapor concentration C_{HS} that is lower

than the C_{BL} (i.e. $dC/dz_{z=0} = 0$ outside the pore). While the C_{HS} will change due to dilution of the antifreeze with water (see Figure 4.4), for the analysis it is assumed to be constant because the dilution time scale observed during the single pore experiments was significantly longer than the vapor diffusion time scale of ~h_{BL}^2/D_{w}~1 s (where D_w is the water vapor diffusion coefficient in air equal to ~0.25×10^{-4} m^2s^{-1} near room temperature). In the quasi-steady state, the governing equation reduces to $\Delta C(x, y, z) = 0$, making the problem formulation mathematically equivalent to one of the common cases of heat spreading resistance problems.[115,116]

Muzyczka et al.[116] showed that the mathematical difficulties posed by the mixed boundary conditions at the membrane surface can be handled by assuming a constant mass sink, J_{HS} (units of mol/s) at the pore surface that is equivalent to the mass sink driven by the constant pore surface concentration C_{HS} (see the schematics of the two cases in Figure 4.5a). The plots in Figure 4.5b indeed shows excellent agreement between concentration profiles along the membrane diagonal, s, for the mixed and equivalent mass sink boundary condition cases simulated using Finite Element Method (FEM) for wide range of b/a (with a=1 mm, h_{BL}= 5 mm, C_{BL}(293 K)=0.9596 mol/m^3, and C_{HS}(268 K)=0.0113 mol/m^3). The simulated values also match well with Muzyczka et al.[116] analytical equivalent mass sink solution for concentration at the membrane surface. According to the authors, the excess concentration, $\theta(x, y, z) = C(x, y, z) - C_{top}$, over a square a rectangular pore with sides b_1 and b_2 on a rectangular bottom plane with sides a_1 and a_2 that provides a mass sink flux of J_{HS} (in our case square unit cell with square pore, thus $a = a_1 = a_2$ and $b = b_1 =$

b_2) and with a convective boundary condition on the top plane located at a height h_{BL} above the membrane (with convection coefficient h) can be expressed as:

$$\theta(x,y,z) = A_0 + B_0 z + \sum_{m=1}^{\infty} \cos(\lambda x)\,[A_1 cosh(\lambda z) + B_1 sinh(\lambda z)] +$$

$$\sum_{n=1}^{\infty} \cos(\delta y)\,[A_2 cosh(\delta z) + B_2 sinh(\delta z)] +$$

$$\sum_{m=1}^{\infty}\sum_{n=1}^{\infty} \cos(\lambda x)\cos(\delta y)\,[A_3 cosh(\beta z) + B_3 sinh(\beta z)] \qquad \text{(Eq. 4.3)}$$

Where $\lambda = \frac{m\pi}{a_1}, \delta = \frac{n\pi}{a_2}, \beta = \sqrt{\lambda^2 + \delta^2}$, and $A_0, A_1, A_2, B_0, B_1, B_2$ are the Fourier coefficients. In general $B_i = -\phi(\zeta) A_i$ and

$$\phi(\zeta) = \frac{\zeta \sinh(\zeta h_{BL}) + h/D_w \cosh(\zeta h_{BL})}{\zeta \cosh(\zeta h_{BL}) + h/D_w \sinh(\zeta h_{BL})} \qquad \text{(Eq. 4.4)}$$

Where ζ is replaced by λ, δ, or β (in our case $\lambda = \delta$). In addition, it is also assumed that the pore size is significantly smaller than the boundary layer thickness (i.e. at least $h_{BL}/a \geq 5$). Consequently, $e^{-\frac{m\pi}{a} h_{BL}} \to 0$ and:

$$\phi(\lambda) = \phi\left(\frac{m\pi}{a}\right) = \frac{\frac{m\pi}{a}\sinh\left(\frac{m\pi}{a}h_{BL}\right) + \frac{h}{D_w}\cosh\left(\frac{m\pi}{a}h_{BL}\right)}{\frac{m\pi}{a}\cosh\left(\frac{m\pi}{a}h_{BL}\right) + \frac{h}{D_w}\sinh\left(\frac{m\pi}{a}h_{BL}\right)} =$$

$$\frac{\frac{m\pi}{2a}\left(e^{\frac{m\pi}{a}h_{BL}} - e^{-\frac{m\pi}{a}h_{BL}}\right) + h/D_w\left(e^{\frac{m\pi}{a}h_{BL}} + e^{-\frac{m\pi}{a}h_{BL}}\right)}{\frac{m\pi}{a}\left(e^{\frac{m\pi}{a}h_{BL}} + e^{-\frac{m\pi}{a}h_{BL}}\right) + h/D_w\left(e^{\frac{m\pi}{a}h_{BL}} - e^{-\frac{m\pi}{a}h_{BL}}\right)} = 1 \qquad \text{(Eq. 4.5)}$$

In order to predict nucleation conditions, only modeling of the vapor concentration at the membrane surface, where $z = 0$, is required and Eq. 4.3 reduces to:

$$\theta(x,y,0) = A_0 + \sum_{m=1}^{\infty} \cos(\lambda x)\, A_m + \sum_{n=1}^{\infty} \cos(\delta y)\, A_n +$$

$$\sum_{m=1}^{\infty}\sum_{n=1}^{\infty} \cos(\lambda x)\cos(\delta y)\, A_{mn} \qquad \text{(Eq. 4.6)}$$

Setting $h \to \infty$ reduces the top convective boundary condition to a fixed concentration. As a consequence the zeroth order Fourier coefficient reduces to:

$$A_0 = \frac{J_{HS}}{a^2}\left(\frac{h_{BL}}{D_w} + \frac{1}{h}\right) = \frac{J_{HS} h_{BL}}{a^2 D_w} \qquad \text{(Eq. 4.7)}$$

Assuming that the pore is centrally located (pore center coordinates of $X_A = Y_A = a/2$) and using the trigonometric identity $sinx - siny = 2sin(\frac{x-y}{2})\ cos(\frac{x+y}{2})$ and Eq. 4.5, the rest of the Fourier coefficients reduce to:

$$A_m = \frac{2J_{HS}\left[\sin\left(\frac{2X_A+b}{2}\lambda_m\right)-\sin(\frac{2X_A-b}{2}\lambda_m)\right]}{a^2bD_w\lambda_m^2\phi(\lambda_m)} = \frac{4J_{HS}\sin\left(m\pi\frac{b}{a}\right)cos\left(\frac{m\pi}{2}\right)}{bD_w\pi^2m^2}$$

$$A_n = \frac{2J_{HS}\left[\sin\left(\frac{2X_A+b}{2}\lambda_n\right)-\sin(\frac{2X_A-b}{2}\lambda_n)\right]}{a^2bD_w\lambda_n^2\phi(\lambda_n)} = \frac{4J_{HS}\sin\left(n\pi\frac{b}{a}\right)cos\left(\frac{n\pi}{2}\right)}{bD_w\pi^2n^2} \qquad \text{(Eq. 4.8)}$$

$$A_{mn} = \frac{16J_{HS}cos(\lambda_m X_A)sin\left(\frac{1}{2}\lambda_m b\right)cos(\delta_n X_A)sin\left(\frac{1}{2}\delta_n b\right)}{a^2ab^2D_w\lambda_m\delta_n\beta_{mn}\phi(\beta_{mn})} =$$

$$\frac{16J_{HS}a\ cos\left(\frac{n\pi}{2}\right)\sin\left(n\pi\frac{b}{a}\right)\sin\left(m\pi\frac{b}{a}\right)cos\left(\frac{m\pi}{2}\right)}{b^2D_wmn\pi^3\sqrt{n^2+m^2}}$$

It is noted that since $\beta = \sqrt{\lambda^2+\delta^2} = \frac{\pi}{a}\sqrt{n^2+m^2}$, $\phi(\beta_{mn}) = 1$.

After substitution of all the Fourier coefficients and rearrangement, this solution reduces to:

$$C(x,y,0) = C_{BL} + J_{HS}\frac{h_{BL}}{a^2D_w}\left(1 + 4\frac{a}{b}\frac{a}{h_{BL}}\sum_{m=1}^{\infty}\frac{\cos\left(\frac{xm\pi}{a}\right)\cos\left(\frac{m\pi}{2}\right)\sin\left(\frac{m\pi b}{2\ a}\right)}{\pi^2m^2} + \right.$$

$$4\frac{a}{b}\frac{a}{h_{BL}}\sum_{n=1}^{\infty}\frac{\cos\left(\frac{yn\pi}{a}\right)\cos\left(\frac{n\pi}{2}\right)\sin\left(\frac{n\pi b}{2\ a}\right)}{\pi^2n^2} +$$

$$\left. 16\left(\frac{a}{b}\right)^2\frac{a}{h_{BL}}\sum_{n=1}^{\infty}\sum_{m=1}^{\infty}\frac{\cos\left(\frac{xm\pi}{a}\right)\cos\left(\frac{yn\pi}{a}\right)\cos\left(\frac{m\pi}{2}\right)\sin\left(\frac{m\pi b}{2\ a}\right)\cos\left(\frac{n\pi}{2}\right)\sin\left(\frac{n\pi b}{2\ a}\right)}{\pi^3mn\sqrt{n^2+m^2}}\right) \qquad \text{(Eq. 4.9)}$$

For the plots in Figure 4.3b, the value of J_{HS} was substituted from the FEM simulation for each analytical curve case (the "analyt. FEM J_{HS}" curves). Consequently, in order for Eq. 4.9 to have true predictive utility, a formula for J_{HS} that is a function of the geometrical parameters as well as the top and the sink water vapor concentrations must be developed. From Fick's law it is known that the maximal value of the J_{HS} will be $J_{max} = D_W(C_{HS} -$

$C_{BL}) \frac{a^2}{h_{BL}}$ when $b \to a$ (i.e. complete film of antifreeze). The plot in Figure 4.3c shows that, when normalized by this maximum value, the mass sink values obtained from FEM simulations follow a common trend with the b/a ratio that is well represented by the functional form $1 - e^{-w\left(\frac{b}{a}\right)^u}$. It is noted that in agreement with physics of the problem, this relation decays to 0 when $b/a \to 0$ (i.e. no mass sink when there is no pore). The inset in Figure 4.3c shows that the two parameters w and u are a function of the a/h_{BL} ratio and can be respectively fitted with a second order polynomial and a power function. Specifically, we found that the relationships $u = 1.13(a/h_{BL})^{0.2}$ and $w = 10.52 - 48.57(a/h_{BL}) + 116.64(a/h_{BL})^2$ provide excellent fits to the simulation data (see Table 4.2 for specific values). Consequently, we propose the following empirical formula for the equivalent mass sink:

$$\frac{J_{HS}\left(\frac{b}{a}, \frac{h_{BL}}{a}\right)}{D_W(C_{HS} - C_{BL})\frac{a^2}{h_{BL}}} = \left(1 - e^{-\left(10.52 - 48.57\left(\frac{a}{h_{BL}}\right) + 116.64\left(\frac{a}{h_{BL}}\right)^2\right)\left(\frac{b}{a}\right)^{1.13(a/h_{BL})^{0.2}}}\right) \quad \text{(Eq. 4.10)}$$

fitting parameter value	**95% CI**	
1.126	1.038	1.215
0.203	0.181	0.226
10.52	10.29	10.75
-48.57	-54.92	-42.23
116.64	87.19	146.09

Table 4.2 95% confidence interval values for the fitted model parameters for $1 - e^{-w\left(\frac{b}{a}\right)^u}$.

Validating this relation, the plots in Figure 4.3b show good agreement between the FEM simulation results and the concentration profiles calculated using Muzyczka's solution with our proposed mass sink expression ("analyt. fitted J_{HS}" curves).

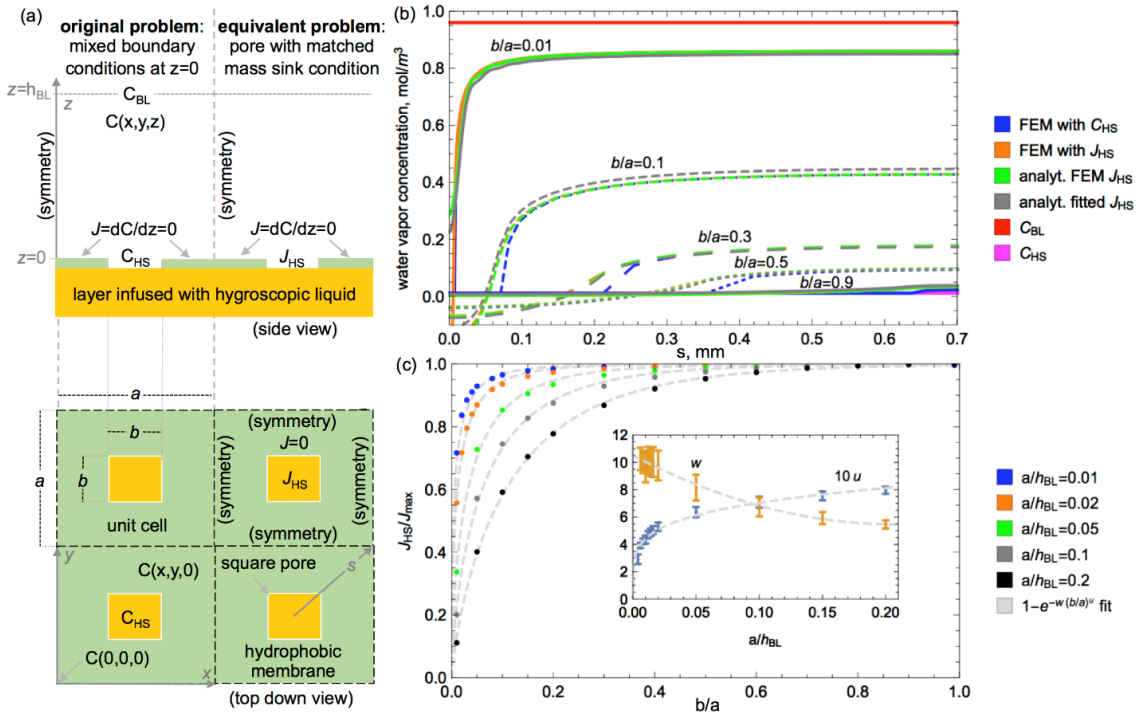

Figure 4.5 (a) Schematic representation of the mathematical formulation of the integral humidity sink effect posed by array of square pores with uniform concentration C_{HS} at the pore surface as well as re-formulated version of the problem proposed by Muzyczka et al.[116] with equivalent mass sink, (b) Plot of concentration profiles along the unit cell diagonal, s, for the two problem formulations simulated using FEM and calculated using Muzyczka et al.[116] analytical solution with J_{HS} directly substituted from FEM simulations as well as calculated using the proposed empirical formula, and (c) plot of the normalized mass sink, J_{HS}/J_{max}, and proposed empirical fits as a function of non-dimensional pore size, b/a, for various pore to boundary layer thickness ratio a/h_{BL}.

Nucleation on the exterior surface of the membrane will not proceed unless the maximum concentration at the membrane surface is equal to or lower than C_{SAT} corresponding to the membrane's surface temperature. Through the symmetry of the problem formulation, we know that the highest concentration on the membrane surface will occur at the corners of the unit cell (e.g. $x = y = 0$). With substitution of Eq. 4.10, Muzychka's general solution can be reduced to the following expression for excess concentration at the corner of the unit cell, $\theta(0,0,0) = C(0,0,0) - C_{BL}$:

$$\frac{\theta(0,0,0)}{\theta_{HS}} = \frac{C(0,0,0)-C_{BL}}{C_{HS}-C_{BL}} = \Omega_0\left(\frac{b}{a}, \frac{a}{h_{BL}}\right) = \frac{J_{HS}\left(\frac{b}{a}, \frac{a}{h_{BL}}\right)}{J_{max}}\left(1 + 8\frac{a}{h_{BL}}\Omega_1\left(\frac{b}{a}\right)\right) \quad \text{(Eq. 4.11)}$$

Where

$$\Omega_1\left(\frac{b}{a}\right) = \frac{a}{b}\sum_{m=1}^{\infty}\frac{\cos\left(\frac{m\pi}{2}\right)\sin\left(\frac{m\pi b}{2\ a}\right)}{\pi^2 m^2} + 2\left(\frac{a}{b}\right)^2\sum_{n=1}^{\infty}\sum_{m=1}^{\infty}\frac{\cos\left(\frac{m\pi}{2}\right)\sin\left(\frac{m\pi b}{2\ a}\right)\cos\left(\frac{n\pi}{2}\right)\sin\left(\frac{n\pi b}{2\ a}\right)}{\pi^3 mn\sqrt{n^2+m^2}}$$

(Eq. 4.12)

Importantly, Eq. 4.10 through 4.12 are only functions of the non-dimensional geometrical ratios of the unit cell size to the boundary layer thickness (a/h_{BL}) and the pore size to the unit cell size (b/a). The plot in Figure 4.6 shows that the absolute value of the Ω_1 function is at most 0.03.

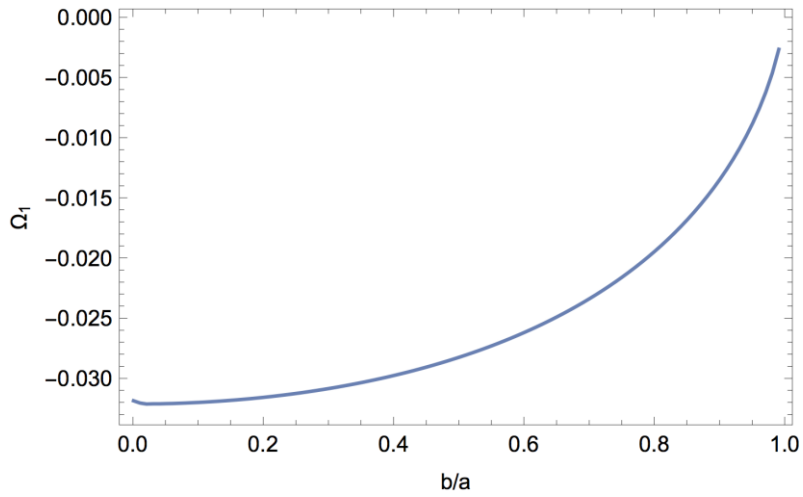

Figure 4.6 Variation of the function Ω_1 with the non-dimensional pore size ($\frac{b}{a}$)

Consequently, as the unit cell size decreases to microscale and below (i.e. with h_{BL} of a few millimeters,[64] $a/h_{BL} \to 0$), Eq. 4.11 reduces to the normalized mass sink (i.e. $\theta(0,0,0)/\theta_{HS} \to J_{HS}\left(\frac{b}{a}, \frac{a}{h_{BL}}\right)/J_{max}$). Furthermore, as $a/h_{BL} \to 0$, $w \to 10.52$ and $u \to 0$ leading to $J_{HS}\left(\frac{b}{a}, \frac{a}{h_{BL}}\right)/J_{max} \to 1 - e^{-10} \to 1$, implying that $\theta(0,0,0) \to \theta_{HS}$ and $C(0,0,0) \to C_{HS}$. In other words, the maximum concentration on the membrane surface will be equal to the concentration set by the propylene glycol liquid within the pore. Remarkably, this means that as the length scale of the pore array decreases to microscale and below the vapor concentration will be uniform and equal to the humidity sink concentration. Furthermore, when the exponential term in Eq. 4.10 decays to zero, this effect will be completely independent of the non-dimensional pore size. The threshold for this condition can be assumed to occur when the exponential term is smaller than 0.01 (i.e.

at least $e^{-4.5}$), which leads to the following expression for the critical value of the non-dimensional pore size:

$$\left(\frac{b}{a}\right)_{critial} \geq \left(\frac{4.5}{105.2-48.57\frac{a}{h_{BL}}+116.6\left(\frac{a}{h_{BL}}\right)^2}\right)^{0.89\left(\frac{a}{h_{BL}}\right)^{0.2}} \qquad \text{(Eq. 4.13)}$$

4.3.2.2. Experimental Validation

The dependence of the excess concentration ratio solely on temperature (left hand side of Eq. 4.11) and of the Ω_0 function solely on two geometrical ratios b/a and h_{BL}/a (right hand side of Eq. 4.11) provides a path for experimental validation of the theory developed in the previous section. Specifically, the theory can be validated by comparing experimental values of nucleation onset surface temperature ("NOST") on various pore array geometries to ones determined theoretically through equating of the $\frac{C_{sat}(T_{NOST})-C_{BL}(T_{BL})}{C_{HS}(T_{NOST})-C_{BL}(T_{BL})}$ ratio with $\Omega_0\left(\frac{b}{a},\frac{a}{h_{BL}}\right)$ for utilized geometry. The plots in Figure 4.7a show these two functions while those in Figure 4.7b show T_{NOST} values predicted by equating them for different pore arrays configurations. A strong dependence of the T_{NOST} range on both the b/a and a/h_{BL} ratios is evident, with sharp decrease predicted with decrease of the unit cell size (with fixed h_{BL}= 5 mm). This trend is a manifestation of the decay of the maximum concentration on the membrane surface towards the value set by the propylene glycol liquid within the pore predicted in previous section. Specifically, while the plot in Figure 4.4a shows that the concentration set by nearly pure propylene glycol (e.g. 99% by weight) is always lower than saturation concentration of supercooled water and ice, the differences between these values becomes negligible (below 0.01 mol/m^3)

as the temperature decreases below 250 K. This implies that for microscale and smaller pore arrays with the b/a larger than the critical value resting on a nearly pure propylene glycol infused layer, nucleation of ice or droplets on the membrane exterior will be inhibited until substrate is cooled to below ~250 K. Naturally, the duration of this effect will depend on the liquid dilution rate, which will increase C_{HS} and with that concentration above the entire surface.

In order to experimentally validate the proposed theory, the nucleation onset surface temperature was measured on samples with the unit cell size ranging over three orders of magnitude from ~500 nm to 1 mm. The images in Figure 4.7c, 4.7d, and 4.7e respectively show images of laser etched PTFE thin film membranes with a=1 mm, PDMS coated metal meshes with a=125 μm and 250 μm, and of commercial polycarbonate membranes with an average equivalent a of ~400 to 600 nm. For the latter samples that have randomly distributed pores the equivalent parameters for a square pore array were defined through statistical analysis of surface electron micrographs As in the single pore experiments, the PTFE and PDMS samples wer tested with native hydrophobic properties as well as with highly hydrophilic gold thin film coating. Since the gold film needs to be about 10 nm thick in order to ensure continuity, it could affect the size of the nanopores and thus was not utilized with the polycarbonate membranes.

Since the onset of nucleation surface temperature is dependent on the concentration of propylene glycol in the pores, it is critical to perform the experiments without substantial dilution of the antifreeze. Another nuisance of using propylene glycol is that it can store substantial content of water that is rejected from the liquid when it is cooled from room temperature (see Figure 4.4a). To avoid artifacts caused by this water vapor rejection

process (i.e. humidity sink temporarily becoming a humidity source), the entire sample was pre-cooled at 268 K with a "dry" source at the top of the chamber and continuous purging of the chamber with flow of dry nitrogen gas for a period of 15 minutes (the time was iteratively determined to be sufficient to remove the excess moisture). Subsequently, the surface temperature of the sample was increased to case-dependent starting temperature while at the same time the wick on top of the chamber was infused with water (the wicking time as a few seconds). The temperature of vapor source at the top of the chamber was maintained at 298 K for all experiments. To determine the T_{NOST}, temperature of the sample was decreased at a ramping rate of 0.1 K/s until condensation water droplets were observed. The cooling process was recorded using a high magnification optical microscope. T_{NOST} was determined by observing the start of formation of visible droplets between pores. To further ensure that the measured temperature was not significantly affected by the fast temperature ramping rate, each experiment was repeated with the starting temperature prior to the ramping adjusted closer to the T_{NOST} value measured during the previous iteration. The experiments were iterated until the value of measured T_{NOST} was independent of the starting temperature.

The measured nucleation onset surface temperatures follow the general theoretically predicted trends. Specifically, the plot in Figure 4.7b shows that T_{NOST} decreases dramatically as the order of magnitude of the unit size is decreased. For example, for b/a ~ 0.3 T_{NOST} decreases from ~275 K at a=1 mm to ~255 K for a=125 to 250 μm and remarkably to ~230 K for a~0.5 μm. To reiterate, for same area fraction of exposed propylene glycol the temperature for onset of nucleation can be decreased by 40 K simply by decreasing the size of the pores from millimeters to a fraction of micrometer. Similarly,

for larger b/a about a 20 K drop in T_{NOST} was measured when the unit cell size was decreased by an order of magnitude from 1 mm to 125 to 250 μm. In all cases, the dramatic effects of the unit cell size and the non-dimensional pore size are quantitatively predicted by the developed model, which validates the proposed theory of the integral humidity sink effect. The most pronounced discrepancy between experimental and theoretical results is an offset of the experimental data by ~5 to 10 K for the nanoporous samples. This effect likely stems from the significant departure of the geometry of randomly distributed nanopores from the idealized square grid pore array that we modeled. Furthermore, vapor transport within the nanopores is likely slowed down due to increased boundary scattering. Specifically, the continuum assumption is valid for flows with the Knudson number, $Kn = \lambda/L$, smaller than ~0.1 (where L is the representative physical length scale equal to the pore diameter in this case). In case of water vapor in air at atmospheric pressure, p, the molecular mean free path, λ, can be calculated as:

$$\lambda = \frac{k_b T}{\sqrt{2} d^2 p} \qquad \text{(Eq. 4.14)}$$

Where k_b is the Bolzmann constant of 1.3806x10^{-23} J/K, T is the temperature in K, and d is the particle hard-shell diameter (265 pm for water). For the temperature range in the experiments (230 K to 293 K), the mean free path of water vapor is on the order of 30 nm to 40 nm. Since the utilized pores have diameters ranging from 10 nm to 200 nm, the Knudson number is greater than 0.2 to 3 and the flow is clearly not in the continuum regime. However, boundary scattering only slows down the transport of water vapor, which would translate in this case into depleted humidity sink effect and facilitated nucleation on the

surface. Consequently, as a result of this non-continuum effect the measured T_{NOST} on the nanoporous samples is likely increase.

The nucleation onset surface temperature measurements can also be used to validate the formula developed for the critical value of the non-dimensional pore size needed for reaching a uniform surface vapor concentration for different unit cell sizes (i.e. Eq. 4.13). Specifically, this condition can be assumed to occur when $\frac{C_{sat}(T_{NOST})-C_{BL}(T_{BL})}{C_{HS}(T_{NOST})-C_{BL}(T_{BL})} \geq 0.99$. Based on the inset in the plot in Figure 4.7a (here T_{BL}=298 K), this condition occurs at around 240 K and 250 K for propylene glycol concentrations of 99% and 75%, respectively (we broader the concentration range to take into account possible surface dilution). In other words, it can be assumed that the surface concentration gradient vanishes when T_{NOST} is in this range. Based on the experimental data, this condition occurs for the nanopore and micropore (a=125 to 250 μm) samples when b/a is larger than ~0.05 to 0.1 and ~0.45, respectively. In a reasonable agreement, corresponding values of the critical b/a of 0.01 to 0.02 and 0.3 to 0.4 are obtained using Eq. 4.13 with h_{BL}=5 mm. For the largest pores with a =1 mm Eq. 4.13 predicts a critical b/a of 0.8, however, the corresponding experimental T_{NOST} is ~260 K, which is well above the threshold value of ~250 K. It is noted that Eq. 4.13 was derived under the assumption of $a/h_{BL} \rightarrow 0$, while for the large pores a/h_{BL}=0.2. Consequently in this case using the full model results in Figure 4.4b provides a better estimate of the critical b/a of ~0.95. This value of the non-dimensional pore corresponds to a nearly open propylene glycol film and is beyond the capabilities of the PTFE membrane laser etching method (thus cannot be observed).

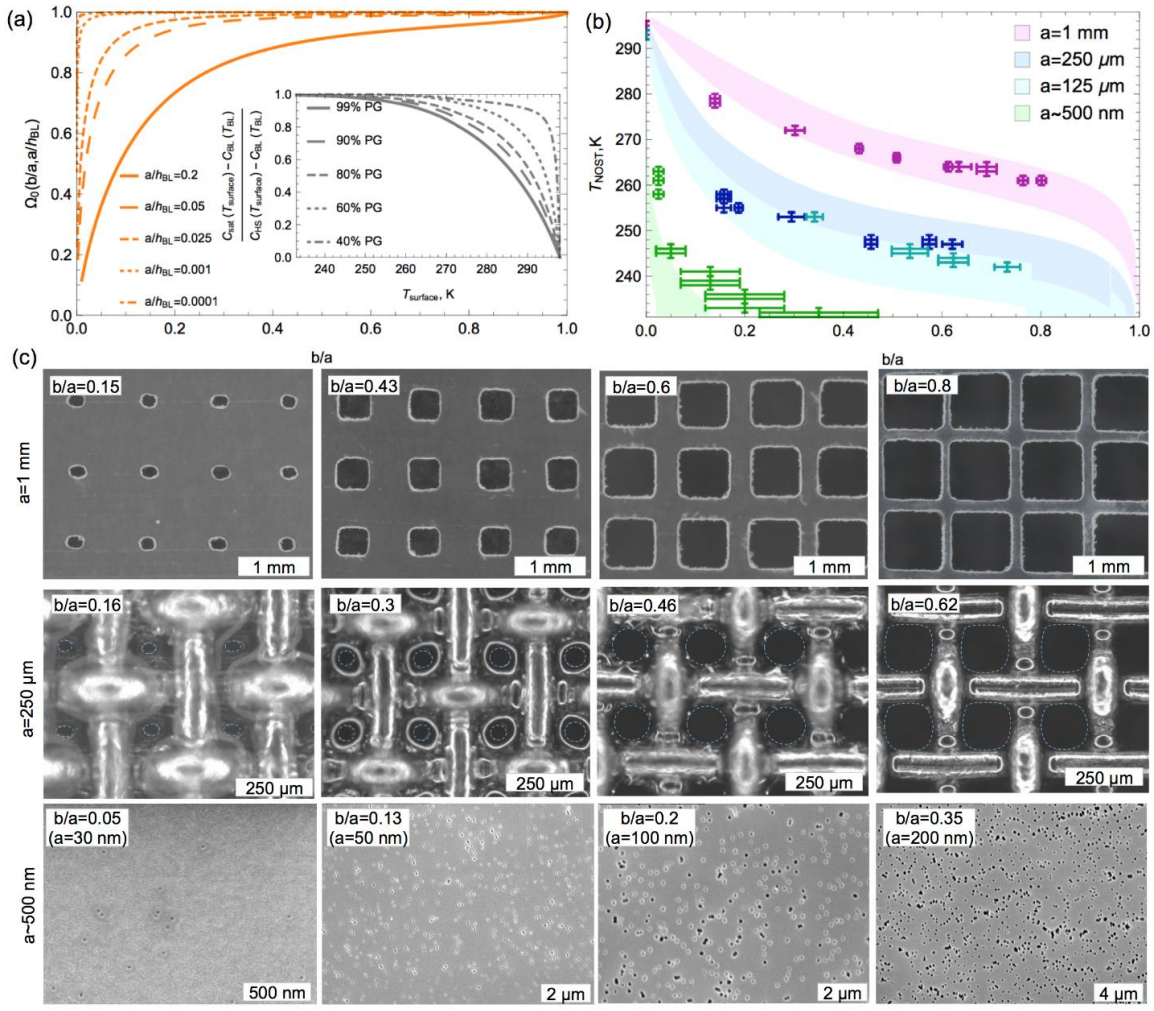

Figure 4.7 (a) Plot of Ω_0 as a function of non-dimensional pore size, b/a, for various ratios of the array unit cell size to boundary layer thickness, a/h_{BL}; the inset shows variation of the excess saturation to pore surface concentration ratio, $\frac{C_{sat}(T_{surface})-C_{BL}(T_{BL})}{C_{HS}(T_{surface})-C_{BL}(T_{BL})}$, as a function of surface temperature, $T_{surface}$, for fixed boundary layer temperature of T_{BL}=298 K; (b) Plot of theoretically predicted (colored areas) and experimentally measured (points with darker tone of the colored area correspond to this a) nucleation onset surface temperature, T_{NOST}, as a function of b/a for various a/h_{BL} ratios (to account for some dilution effects, predictions for propylene glycol concentrations between 75% and 99% are

plotted for each unit cell size), and (c) example images of the porous membranes used in the experiments with unit cell size, a, of 1 mm (laser etched PTFE membranes), 250 μm (PDMS coated steel mesh), and ~500 nm (for the polycarbonate membranes an equivalent cell size was found through image analysis).

4.3.2.3. Shape Effect of Pores

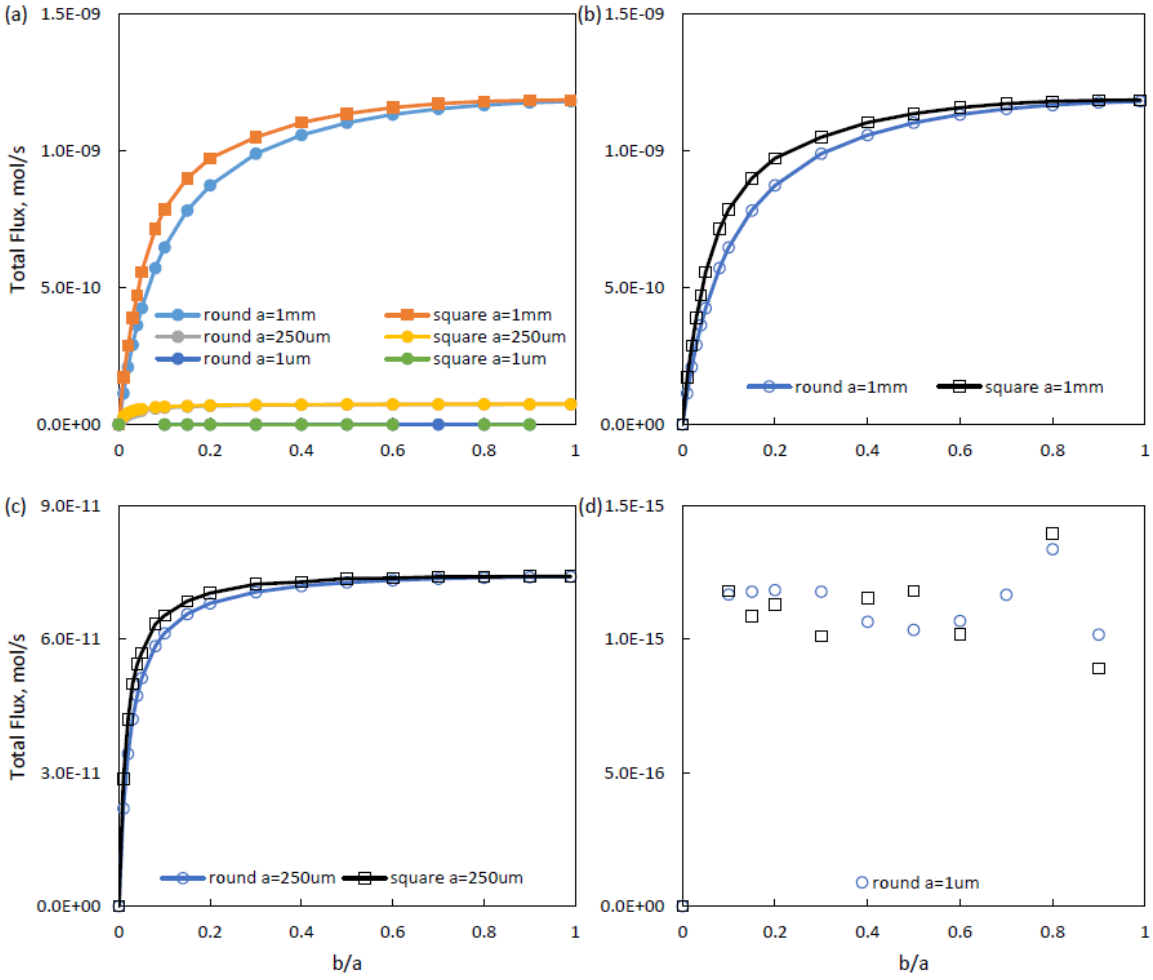

Figure 4.8 (a) Plot of simulation result of total flux on the pore area, F, of cell size a=1 mm, 250 μm, 1 μm for square and round pores; Simulation results of cell size a=1 mm, 250 μm, 1 μm are presented in (b)(c)(d) respectively.

a	Shape	Integral Difference
1mm	Square	4%
	Round	
250μm	Square	2%
	Round	
1μm	Square	1%
	Round	

Table 4.3 Fitted functions of F for cell size a=1 mm, 250 μm, 1 μm; The difference of F between square and round pore shapes in three cell size a.

In this chapter, the integral humidity effect has been discussed using a model of pores of square shape. Pores of square shape can be easily fabricated using laser machining in millimeter scale. However, due to the difficulty of fabrication, pore shape is barely square for microscale and nanoscale samples, whose shape appears to be circular. The shape effect of square and round pores is addressed in this section using finite element simulations. Three scenarios of different cell sizes (a=1mm, 250μm, 1μm) are compared in Figure 4.8, and the boundaries are identical to Figure 4.5.

Figure 4.8(a) shows the simulation results of total flux, F, on the pore area for both square and round pores of three different cell sizes. Figure 4.8(b)(c)(d) show F of cell size 1mm, 250μm and 1μm respectively. The largest discrepancy of square and round pores can

be found in a=1mm scenario, Figure 4.8(b). Comparing to millimeter pore size, F of square and round pores are nearly identical in microscale and nanoscale domain, Figure 4.8(c) and (d). To numerically define the discrepancy between square and round pore, integral difference is calculated as following. For each set of data from simulation result of F, the integral over the domain $0<b/a<1$ was numerically calculated in Matlab. The integral difference is identical to the difference of areal integral in Figure 4.8. The difference in percentage of F of the two shapes are presented in Table 3. The largest discrepancy between the two shapes is around 4% when cell size a=1 mm. The F of the two shapes with cell size a=250μm and 1μm are nearly identical.

4.3.3. The Temporal Anti-frosting Performance of the Nanoporous Bi-layer Antifreeze Infused Coatings

In the previous section it was demonstrated that due to a vanishing ratio of the unit cell size to the boundary layer thickness ratio, the nanoporous bi-layer antifreeze infused coatings can provide a remarkable ~40 K depression in surface temperature required for onset of nucleation. Furthermore, at the surface of the nanoporous membranes the water vapor concentration is uniform and equal to the concentration set by the propylene glycol within the pores. This effect provides a strong advantage over membranes with larger pores on which saturation concentration can be reach easier in-between the pores. Consequently, the bi-layer antifreeze infused coatings with nanoporous exterior appear to be optimal for anti-frosting applications. However, besides lowering of the nucleation onset point described in previous section, the key characteristics of anti-frosting coatings are the delay in frost onset and the time needed for complete icing over of the surface. To quantify the

times required for onset of condensation, frost formation, and complete icing over of the samples, extended frosting experiments on the nanoporous sample set cooled to 263 K, 253 K, and 243 K were conducted. Figure 4.9 shows histograms and corresponding images of the extended frosting at the latter two temperatures. Since the T_{NOST} for the membrane with b/a =0.025 (10 nm pore diameter) was ~260 K, water condensed and froze nearly instantaneously on these samples (<1 minutes). For the rest of the nanoporous membranes the T_{NOST} was substantially lower (near or below 240 K) which translated into substantially longer condensation and frost onset times. Specifically, at 253 K the condensation onset time was 5 minutes on the membrane with b/a=0.12 (50 nm pore diameters and T_{NOST} ~240 K) while a 10 minutes delay was achieved on membranes with b/a=0.12 (100 nm and T_{NOST} ~235 K) and b/a=0.12 (200 nm and T_{NOST} ~232 K) pore diameters. Setting the sample temperature to 243 K decreased the corresponding condensation delay times to 2 to 5 minutes. After the condensation onset, droplets began to freeze about 1 to 2 minutes and ~10 minutes at sample surface temperatures of 243 K and 253 K. By comparison, condensation is nearly instantaneous on any solid substrates when they are their temperature is decreased slightly below the dew point (e.g. ~298 K in our experiments).

Besides occurring much faster, frosting of the nanoporous membrane with the smallest b/a=0.025 proceeded in a different mode from the membranes with larger nanopores. Specifically, the images in Figure 4.9 show that both during the 243 K and 253 K experiments droplets condensed and froze over the entire surface of the sample with b/a =0.025 within 5 minutes. In contrast, on the samples with larger nanopores condensation is followed with gradual wave-like propagation of frost and its dendrites from the edges of the sample.[44,64,81,105,117] The time required for complete coverage of the surface

by frost increases with the pore size and is about 1 to 2 h and 15 to 20 minutes at 253 K and 243 K, respectively. Interestingly, while the nucleation onset times during frosting experiments conducted with surface temperature of 263 K increase substantially to 2 h, the freezing onset times increase dramatically to 2 h. In addition, the morphology of the ice crystals formed at 263 K resembles ice slush, not the classical frost dendrites observed at the lower temperatures. Taking also into consideration that in similar cooling conditions ice crystals begin to appear in a film of propylene glycol within 1 to 1.5 h,[111] it is asserted that the dramatic increase in freezing onset time of the nanoporous membranes cooled to 263 K occurs due to formation of a liquid bridges across the nanopores that releases antifreeze to the exterior. At 263 K the liquid bridge likely forms through bottom up filling of the pores due to dilution of the propylene glycol via vapor diffusion. As the substrate temperature is decreased to 253 K and 243 K the probability of nucleation on the exterior of the surfaces increases. Once droplets or frost do nucleate on the exterior and begin to growth vertically, a majority of the water vapor molecules will be depleted prior to reaching the bottom of the pores. In other words, due to the competing mass sink posed by exterior frost growth, the antifreeze is never "released" out of the relatively deep (~6 μm) nanopores used in the current experiments. Consequently, the optimal design of the bi-layer nanoporous anti-frosting must also take into consideration transient dilution effects and balance pore diameter as well as pore depth.

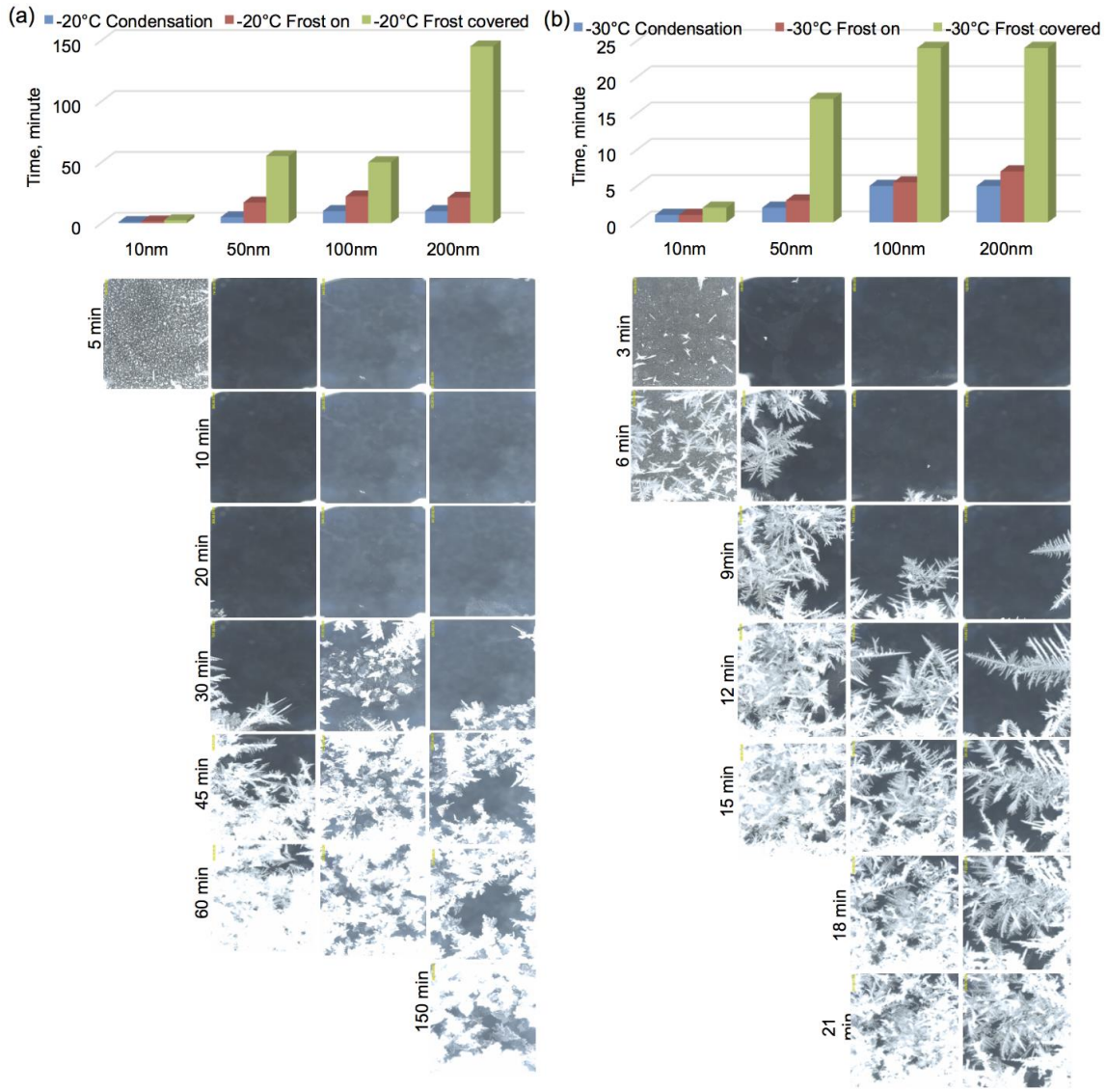

Figure 4.9 Histogram and images summarizing the results of the extended frosting experiments of the nanoporous bi-layer antifreeze infused coatings with surface temperature of (a) 253 K and (b) 243 K.

4.4. Conclusions

In this Chapter the engineered integral humidity sink effect posed by porous bi-layer coatings with bottom infused with hygroscopic liquid was methodically studied and intriguing size effects in this system were revealed. First it was demonstrated that with a proper design of the environmental chamber that allows for exact replication of boundary conditions in the model formulation, the size of the region of inhibited condensation and condensation frosting around an isolated propylene glycol pore can be quantitatively predicted by previously described solution of the quasi-steady state water vapor concentration field.[64,65] The size of this region relative to the pore diameter is a constant that depends solely on the ratio of the excess saturation to the excess humidity sink concentrations (i.e. $(C_{SAT} - C_{BL})$ /$(C_{HS} - C_{BL})$). This effect is a result of the hyperbolic vapor concentration profile around the pore, and as it was shown, does not occur when the concentration field changes due to presence of multiple periodically spaced pores. It was shown that for the simplest case of such periodic geometry, the square pores distributed on a square grid array, an analytical solution of the three dimensional concentration field can be obtained by analyzing a unit cell of the system. Specifically, the equivalent mass sink solution developed by Muzychka et al.[116] (Eq. 4.11 and 4.12) was extended with an empirical expression for sink term (Eq. 4.10) based on fitting of finite element simulations. This analysis revealed that the ratio of the maximum (i.e. unit cell corner) excess to the humidity sink excess concentrations is governed by only two non-dimensional geometrical parameters: the pore size relative to the unit cell size (b/a) and the ratio of the unit cell size to the thickness of the boundary layer (a/h_{BL}). In other words, knowing the source

(boundary layer) and sink (propylene glycol) concentrations and these two geometrical ratios, it can be predict if nucleation will occur on the surface (i.e. unit cell corner concentration is larger than the saturation concentration corresponding to surface temperature). Intriguingly, this solution shows that when the boundary layer thickness is much larger than the unit cell size (i.e. $a/h_{BL} \to 0$) the surface concentration becomes uniform and equal to the humidity sink concentration, nearly irrespective of the non-dimensional pore size. In particular, this effect occurs for b/a greater than a critical value for specific a/h_{BL} (see Eq. 4.13). For nanoporous surfaces with a~500 nm the critical value of b/a is ~0.05, implying a vanishing surface concentration gradient for nearly all possible sample geometries. As we showed, the lack of a concentration gradient across the surface of the nanoporous surfaces translates into dramatic lowering of the temperature required for onset of droplet and frost nucleation. For example, for $b/a \sim 0.3$ T_{NOST} decreases from ~275 K at a=1 mm to ~255 K for a=125 to 250 μm and remarkably to ~230 K for a~0.5 μm. To reiterate, for same area fraction of exposed propylene glycol we can decrease the temperature for onset of nucleation by 40 K simply by decreasing the size of the pores from millimeters to a fraction of micrometer. Since it is set by the propylene glycol vapor pressure, this effect is of course transient. For the nanoporous membranes with $b/a > 0.15$, the samples remained mostly frost-free for impressive ~10 and ~30 minutes at 243 K and 253 K, respectively. Naturally, condensation onset occurred earlier at around 5 and 10 minutes at 243 K and 253 K, respectively. On these samples cooled only to 263 K droplets began to condense after substantially 120 minutes longer. The impressive 2 hour delay of freezing of the condensate in this case highlighted two possible and competing modes of frosting on the nanoporous surface. Specifically, at 263 K the

long inhibition in exterior condensation provides sufficient time for the bottom up filling of the pores and release of the antifreeze. This in turn causes the dramatic delay in onset of freezing of the condensate. When temperature was lowered to 253 K and 243 K, frost formation on the exterior and its vertical growth occurred faster, preventing release of the antifreeze (since frost growth depletes majority of the water vapor travelling to the pores).

CHAPTER 5

CONCLUSION AND RECOMMENDATIONS FOR FUTURE WORK

5.1. Summary of the Performed Work

Icing is a common atmospheric phenomenon that can cause significant problems in various industries.[81] The specific challenges posed by ice depend on its physical form, which is dictated by its formation mechanism. For instance rime and glaze form during impact of supercooled water drops and can make all types of travel dangerous, disrupt electricity delivery, and decrease efficiency of wind power generation.[8,14,118,119] In turn frost forms through heterogeneous nucleation from the vapor phase and can reduce heat transfer efficiency of refrigerators and heat exchangers by as much as 50% to 75%.[120,121] Frost also plays a subtle role in rendering superhydrophobic and lubricant-impregnated anti-icing coatings that are designed to prevent rime and glaze accretion ineffective.[15,32,122,123] In particular, condensate and frost cause pinning of impinging supercooled droplets and increase adhesion of resulting ice layer by filling in the nano/microscale texture of superhydrophobic surfaces.[15] Growth of frost dendrites on lubricant impregnated surfaces leads to rise of a capillary pressure that drains the oil away from the substrate into the ice.[35,122] Consequently, to be of any practical use, non-wetting anti-icing coatings must be re-engineered to also prevent or slow down the growth of frost.

This dissertation work introduced a novel type of anti-icing coating inspired by the functional liquid skin secretion in natural systems was introduced. This semi-passive

coating consists of porous superhydrophobic epidermis and wick-like underlying dermis that is infused with antifreeze liquid. The outer layer serves as a barrier between the antifreeze and environment and, as a typical anti-icing superhydrophobic surface, easily sheds large sessile drops. However, in scenarios in which a typical SHS easily ices over, such as by pore penetration by high-velocity impacting drops or condensation frosting, the coating architecture responds by releasing stored antifreeze liquid. In general, the presence of antifreeze on the surface, with or without the epidermis layer, prevents the accumulation of all the studied forms of ice for a significantly longer time when compared to all other studied anti-icing coatings. The addition of the epidermis dramatically improved the performance of the surface in freezing rain conditions. For the condensation frosting experiments, addition of the epidermis slowed both the icing-onset and complete icing-over of the surface by about 133% as compared to the Ny+PG (additional 20 to 40 minutes) and by at least 1600% as compared to all other samples (i.e., 80 minutes vs. <5 minutes). The addition of the epidermis on top of the dermis had negligible effect on delaying freezing of the mist because of rapid merging of the impinging micro-drops with the condensate that flooded the pores. It was also observed that the release of antifreeze not only delayed icing of the surfaces, but also affected the ice morphology and significantly reduced its adhesion. The latter effect was likely caused by the presence of a thin lubricating melt layer between the ice and the surface. The thin lubricating melt film could also help reduce nano/microscale topology abrasive erosion typically observed on superhydrophobic surfaces due to repeated deicing.[75] Overall, it was estimated that use of the bi-layer coating would reduce antifreeze use by 2-8 fold compared to the commercial Weeping Wing system.

The delayed condensation frosting due to integral effect of randomly spaced propylene glycol-filled micropores was implied on by work in Chapter 2 on responsive antifreeze releasing bi-layer anti-icing coatings.[78] Thus, the rest of this dissertation focused on exploring the physics of the integral humidity sink effect and its utilization for delaying of condensation and condensation frosting. Specifically, in Chapter 3 condensation frosting dynamics in presence of macroscopic and microscopic hygroscopic antifreeze droplets were explored. Guardarrama-Centina et al.[64,65] recently demonstrated that if the water vapor pressure at the hygroscopic liquid's surface is lower than the saturation pressure at the sample surface, a region of inhibited condensation (i.e. RIC), and with that frosting, occurs around the individual microscopic droplet of the liquid. It was first demonstrated that, as for microscopic drops, [64,65] for macroscopic droplets (R_0>300 μm) of propylene glycol and salt saturated water the absolute RIC size remains essentially unchanged with δ/R_0~1.5 to 1.8 for R/R_0<1.25 for prolonged periods of time. Utilizing this observation, it was demonstrated that frost formation can be completely inhibited in-between small and large arrays of propylene glycol and salt saturated water drops with $S/2R_0$~1.3 to 1.6 (< 2δ). It was found that on average the arrays of macroscopic propylene glycol and salt saturated water drops delayed complete frosting over of the samples 1.6 and 2.8 times longer than films of the liquids with equivalent volume, respectively. In turn, it was shown that dense arrays of sprayed microscale droplets with $S/2R_0$~1.1 to 1.4 delayed complete frosting over of the samples 1.4 to 1.5 times longer than the sparsely spaced droplets with $S/2R_0$~1.8 to 2.4 and 5 to 10 times longer than films with volume equivalent (to denser arrays). In addition, due to the integral humidity sink effect frost wave propagation into the densely spaced microdroplet array was significantly slower than for the sparsely spaced

microdroplets. This resulted in a major alteration freezing dynamics from "outside in mode" for the sparsely separated droplets to mostly "inside out mode" for the densely separated droplets. Thus this Chapter demonstrates that the integral humidity sink effect of array of hygroscopic drops with $S< 2\delta$ can be exploited to get better antifrosting performance out of a fixed volume of hygroscopic antifreeze. The droplet growth results obtained in this Chapter also qualitatively agreed with scaling laws developed by Beysens and co-workers. However, in Chapter 4 we showed that in order to obtain quantitative prediction of the integral humidity sink effect, the experimental setup had to be altered so that boundary conditions can be accurately represented in the theoretical problem formulation.

In Chapter 3 the basic hypothesis of condensation and condensation frosting inhibition using hygroscopic drops with overlapping RIC was validated. However, dispensing of droplets is a not a scalable solution that can be applied to, for example, aircraft. In contrast, the bi-layer coatings described in Chapter 2 could be adapted for the purpose and applied on a large scale (e.g. as modified primer and top coat paint). Thus in Chapter 4 the possibility of engineering of the integral humidity sink effect using the porous bi-layer coatings was explored. First it was shown that with a proper design of the environmental chamber that allows for exact replication of boundary conditions in the model formulation, the size of the region of inhibited condensation and condensation frosting around an isolated propylene glycol pore can be quantitatively predicted by previously hyperbolic solution of the water vapor concentration field.[64,65] The size of this region relative to the pore diameter is a constant that depends solely on the ratio of the excess saturation to the excess humidity sink concentrations. This effect is a result of the hyperbolic vapor concentration profile around the pore, and as it was shown, does not occur when the

concentration field changes due to presence of multiple periodically spaced pores. It was shown that for the simplest case of such periodic geometry, the square pores distributed on a square grid array, an analytical solution of the three dimensional concentration field can be obtained by analyzing a unit cell of the system. Specifically, the equivalent mass sink solution developed by Muzychka et al.[116] was extended with an empirical expression for sink term based on fitting of finite element simulations. This analysis revealed that the ratio of the maximum (i.e. unit cell corner) excess to the humidity sink excess concentrations is governed by only two non-dimensional geometrical parameters: the pore size relative to the unit cell size (b/a) and the ratio of the unit cell size to the thickness of the boundary layer (a/h_{BL}). In other words, knowing the source (boundary layer) and sink (propylene glycol) concentrations and these two geometrical ratios, it can be predict if nucleation will occur on the surface (i.e. unit cell corner concentration is larger than the saturation concentration corresponding to surface temperature). Intriguingly, this solution shows that when the boundary layer thickness is much larger than the unit cell size (i.e. $a/h_{BL} \to 0$) the surface concentration becomes uniform and equal to the humidity sink concentration, nearly irrespective of the non-dimensional pore size. In particular, this effect occurs for b/a greater than a critical value for specific a/h_{BL}. For nanoporous surfaces with a~500 nm the critical value of b/a is ~0.05, implying a vanishing surface concentration gradient for nearly all possible sample geometries. As we showed, the lack of a concentration gradient across the surface of the nanoporous surfaces translates into dramatic lowering of the temperature required for onset of droplet and frost nucleation. For example, for b/a ~ 0.3 T_{NOST} decreases from ~275 K at a=1 mm to ~255 K for a=125 to 250 μm and remarkably to ~230 K for a~0.5 μm. To reiterate, for same area fraction of exposed

propylene glycol we can decrease the temperature for onset of nucleation by 40 K simply by decreasing the size of the pores from millimeters to a fraction of micrometer.

5.2. Recommendations for Future Work

Since it is set by the propylene glycol vapor pressure, the integral humidity sink effect is of course transient. Consequently, it is recommended that future efforts focus on understanding of the transient dynamics of the engineered integral humidity sink effect. The key aspects of this study should include the effect of pore depth and hierarchical superhydrophobic exterior on the water vapor concentration above the surface. The current work revealed that nanoporous bi-layer coatings with $b/a > 0.15$ provide remarkable depression of the nucleation onset temperature up to 40 K and impressive nucleation onset delays. With further understanding of the process, the nanoporous bi-layer coatings can be designed to combine optimal anti-frosting functionality with water repellency to provide all ice type preventing coatings.

This dissertation explored predominantly inhibition of condensation on the bi-layer, however, it also illustrated the importance of droplet impact, adhesion, and antifreeze mixing on the rime and glaze formation process. Naturally, use of nanoporous surfaces will resolve the issue of fog droplet penetration of the coating. However, the physics of droplet impact onto bi-layer surfaces with a liquid interior are largely unknown. For example, what coating geometry and impact conditions lead to penetration of the outer layer by the imping water? How much pinning force do the formed capillary bridges impose? How long can freezing of such droplets with high antifreeze concentration near surface be inhibited?

Another exciting area of future investigation is the reduced ice adhesion caused by the release of the antifreeze at the interface. This effect should lead to a lubricating melt layer that facilitates ice removal. Here again the effect of the surface geometry on the dynamics of the melt layer formation and ice removal should be quantified. Since optimal geometry for condensation inhibition, droplet repelling, and facilitated ice removal might not necessarily overlap, an optimal bi-layer coating geometry should balance these three functional needs.

Lastly, in order to be translated into industry, bi-layer coating formulation that is easy to apply on a large scale and can compete cost wise with current technologies has to be developed. Possibilities could include novel durable polysiloxane paints, whose corrosion resistance I have studied in my other work.

5.3. Original Contributions and Publications

The primary original contributions of this dissertation are:

- The invention of the bi-layer antifreeze infused coatings that respond to icing by releasing the functional liquid. These coatings significantly improve three “anti-icing” aspects: delay in condensation frosting, freezing of pinned droplets, and ease of formed ice removal. The coating does not get rid of antifreeze, but reduces its use at least by 2-8 fold as compared to current commercial systems.
- The discovery and first systematic investigation of the integral humidity sink effect posed by both arrays of droplets and pores filled with hygroscopic liquid. A theory of the effect posed by the bi-layer coating was developed and experimentally validated.

The key results was demonstration of a vanishing surface concentration gradient with decrease of the pore array length scale to nanoscale (with boundary layer thickness of a few millimeters). This effect translated into dramatically decreased nucleation onset on nanoporous surfaces (down by 40 K comparing to millimeter pore arrays with same area fraction). Past a theoretically predicted non-dimensional pore size, the nanoporous bi-layer surfaces also exhibited a 2 hour delay in onset of surface nucleation at 263 K.

This work resulted in the following archival journal publications:

1. Sun, X. and Rykaczewski, K.* Spatial Control of Nucleation through Engineered Integral Humidity Sink Effect, submitted 11/2016
2. Sun, X., Damle, V., Uppal, A., Linder, R.,[#] Chandrashekar, S., Mohan, R. A., and Rykaczewski, K.* Inhibition of Condensation Frosting by Arrays of Hygroscopic Drops, Langmuir, 31, 13743-13752, (2015).
3. Sun, X., Liu, S., Damle, V. and Rykaczewski, K.* Bioinspired Stimuli-Responsive Antifreeze-Secreting Anti-Icing Coatings. Advanced Materials Interfaces, 2, 7, (2015).

In addition the following conference presentations were a product of this dissertation:

1. Sun, X., Damle, V., Uppal, A., Linder, R. and Rykaczewski, K., Inhibition of Condensation and Condensation Frosting Through Engineered Integral Humidity Sink Effect, ASME IMECE 2016, Phoenix, AZ, 11/2016.

2. Sun, X., Damle, V., and Rykaczewski, K., Bioinspired Stimuli-Responsive and Antifreeze-Secreting Anti-Icing Coatings Spring Meeting 2016, Phoenix, AZ, 4/2016.

3. Sun, X., Damle, V., Liu, X., and Rykaczewski, K., Bionspired Frost-Responsive Antifreeze Secreting Anti-Icing Coatings. ASME IMECE 2015, Houston, TX, 11/2015.

4. Sun, X., Damle, V., and Rykaczewski, K., Bionspired Frost-Responsive Antifreeze Secreting Pagophobic Coatings. 67th APS DFD Meeting, San Francisco, CA, 12/2014.

5. Sun, X., Liu, Z., and Rykaczewski, K., *Thermally Optimized Design of Cooling Stage for in situ ESEM Experimentation.* Microscopy and Microanalysis 2014, Hartford, CT, 8/2014.

6. Sun, X., Damle, V., and Rykaczewski, K., *Bionspired Frost-Responsive Antifreeze Secreting Pagophobic Coatings*, 2014 Arizona Imaging and Microanalysis Society Meeting, Tempe, AZ, 3/2014.

REFERENCES

(1) Björnstig, U.; Björnstig, J.; Dahlgren, A. Slipping on Ice and Snow--Elderly Women and Young Men Are Typical Victims. *Accid. Anal. Prev.* **1997**, *29* (2), 211–215.

(2) Andreyl, J.; Olley2, R. Relationships Between Weather and Road Safety: Past and Future Research Directions. **1990**.

(3) Ryerson, C. C. Ice Protection of Offshore Platforms. *Cold Reg. Sci. Technol.* **2011**, *65* (1), 97–110.

(4) Marwitz, J.; Politovich, M.; Bernstein, B.; Ralph, F.; Neiman, P.; Ashenden, R.; Bresch, J. Meteorological Conditions Associated with the ATR72 Aircraft Accident near Roselawn, Indiana, on 31 October 1994. *Bull. Am. Meteorol. Soc.* **1997**, *78* (1), 41–52.

(5) J. Lu, Z. L. Jiang, Z. H. Hongcai, J. Peng, B. Li, Z. F. No Title. *Autom. Elect. Power Syst.* **2008**, *11* (5).

(6) Ryerson, C. C. No Title. *ERDC/CRRELTR-09-4 Report, U.S. Army Eng. Res. Dev. Center, Hanover, NH* **2009**.

(7) Ryerson, C. C. No Title. *ERDC/CRRELTR-09-4 Report, U.S. Army Eng. Res. Dev. Center, Hanover, NH* **2008**.

(8) Parent, O.; Ilinca, A. Anti-Icing and de-Icing Techniques for Wind Turbines: Critical Review. *Cold Reg. Sci. Technol.* **2011**, *65* (1), 88–96.

(9) Na, B.; Webb, R. L. A Fundamental Understanding of Factors Affecting Frost Nucleation. *Int. J. Heat Mass Transf.* **2003**, *46*, 3797–3808.

(10) Protection, C. I. T. ice. No Title. *http://www.caviceprotection.com/* **2014**.

(11) Chang, Y.-S. Performance Analysis of Frostless Heat Exchanger by Spreading Antifreeze Solution on Heat Exchanger Surface. *J. Therm. Sci. Technol.* **2011**, *6* (1), 123–131.

(12) Ayres, J.; Simendinger, W. H.; Balik, C. M. Characterization of Titanium Alkoxide Sol–gel Systems Designed for Anti-Icing Coatings: I. Chemistry. *J. Coatings Technol. Res.* **2007**, *4* (4), 463–471.

(13) Meuler, A. J.; Smith, J. D.; Varanasi, K. K.; Mabry, J. M.; McKinley, G. H.; Cohen, R. E. Relationships between Water Wettability and Ice Adhesion. *ACS Appl. Mater. Interfaces* **2010**, *2* (11), 3100–3110.

(14) Varanasi, K. K.; Hsu, M.; Bhate, N.; Yang, W.; Deng, T. Spatial Control in the Heterogeneous Nucleation of Water. *Appl. Phys. Lett.* **2009**, *95* (9).

(15) Varanasi, K. K.; Deng, T.; Smith, J. D.; Hsu, M.; Bhate, N. Frost Formation and Ice Adhesion on Superhydrophobic Surfaces. *Appl. Phys. Lett.* **2010**, *97*, 2010–2012.

(16) Tourkine, P.; Le Merrer, M.; Quéré, D. Delayed Freezing on Water Repellent Materials. *Langmuir* **2009**, *25* (13), 7214–7216.

(17) Alizadeh, A.; Yamada, M.; Li, R.; Shang, W.; Otta, S.; Zhong, S.; Ge, L.; Dhinojwala, A.; Conway, K. R.; Bahadur, V.; et al. Dynamics of Ice Nucleation on Water Repellent Surfaces. *Langmuir* **2012**, *28* (6), 3180–3186.

(18) Jung, S.; Tiwari, M. K.; Doan, N. V.; Poulikakos, D. Mechanism of Supercooled Droplet Freezing on Surfaces. *Nat. Commun.* **2012**, *3*, 615.

(19) Guadarrama-Cetina, J.; Mongruel, A.; González-Viñas, W.; Beysens, D. Percolation-Induced Frost Formation. *EPL* **2013**, *101* (101).

(20) T. F. Ford, O. D. Nichols NRL Report 5832, Naval Research Laboratory, Arlington, V. 1962. No Title.

(21) Kulinich, S. A.; Farzaneh, M. On Ice-Releasing Properties of Rough Hydrophobic Coatings. *Cold Reg. Sci. Technol.* **2011**, *65* (1), 60–64.

(22) Lv, J.; Song, Y.; Jiang, L.; Wang, J. Bio-Inspired Strategies for Anti-Icing. **2014**

(23) Barthlott, W.; Neinhuis, C. Purity of the Sacred Lotus, or Escape from Contamination in Biological Surfaces. *Planta* **1997**, *202* (1), 1–8.

(24) Quéré, D. Wetting and Roughness. *Annu. Rev. Mater. Res.* **2008**, *38* (1), 71–99.

(25) Quéré, D. Non-Sticking Drops. *Reports Prog. Phys.* **2005**, *68* (11), 2495–2532.

(26) Wong, T.-S.; Kang, S. H.; Tang, S. K. Y.; Smythe, E. J.; Hatton, B. D.; Grinthal, A.; Aizenberg, J. Bioinspired Self-Repairing Slippery Surfaces with Pressure-Stable Omniphobicity. *Nature* **2011**, *477* (7365), 443–447.

(27) Kulinich, S. A.; Farzaneh, M. Ice Adhesion on Super-Hydrophobic Surfaces. *Appl. Surf. Sci.* **2009**, *255* (18), 8153–8157.

(28) Kulinich, S. A.; Farzaneh, M. How Wetting Hysteresis Influences Ice Adhesion Strength on Superhydrophobic Surfaces. *Langmuir* **2009**, *25* (16), 8854–8856.

(29) Mishchenko, L.; Hatton, B.; Bahadur, V.; Taylor, J. A.; Krupenkin, T.; Aizenberg, J. Design of Ice-Free Nanostructured Surfaces Based on Repulsion of Impacting Water Droplets. *ACS Nano* **2010**, *4* (12), 7699–7707.

(30) Cao, L.; Jones, A. K.; Sikka, V. K.; Wu, J.; Gao, D. Anti-Icing Superhydrophobic Coatings. *Langmuir* **2009**, *25* (21), 12444–12448.

(31) Guo, P.; Zheng, Y.; Wen, M.; Song, C.; Lin, Y.; Jiang, L. Icephobic/Anti-Icing Properties of Micro/Nanostructured Surfaces. *Adv. Mater.* **2012**, *24* (19), 2642–2648.

(32) Kim, P.; Wong, T. S.; Alvarenga, J.; Kreder, M. J.; Adorno-Martinez, W. E.; Aizenberg, J. Liquid-Infused Nanostructured Surfaces with Extreme Anti-Ice and Anti-Frost Performance. *ACS Nano* **2012**, *6* (8), 6569–6577.

(33) Wilson, P. W.; Lu, W.; Xu, H.; Kim, P.; Kreder, M. J.; Alvarenga, J.; Aizenberg, J.; Patankar, N. A.; Yao, X.; Song, Y.; et al. Inhibition of Ice Nucleation by Slippery Liquid-Infused Porous Surfaces (SLIPS). *Phys. Chem. Chem. Phys.* **2013**, *15* (2), 581–585.

(34) Lafuma, A.; Quéré, D.; Onda T., S. S. . S. N. and T. K.; D., Q.; Cottin-Bizonne C., B. J. L. . B. L. and C. E.; Ou J., P. B. and R. J. P.; R., B.; W., N. C. and B.; al, G. X. F. et; Bush J. W. M., H. D. and P. M.; et al. Slippery Pre-Suffused Surfaces. *EPL (Europhysics Lett.* **2011**, *96* (5), 56001.

(35) Rykaczewski, K.; Anand, S.; Subramanyam, S. B.; Varanasi, K. K. Mechanism of Frost Formation on Lubricant-Impregnated Surfaces. *Langmuir* **2013**, *29*, 5230–5238.

(36) Subramanyam, S. B.; Rykaczewski, K.; Varanasi, K. K. Ice Adhesion on Lubricant-Impregnated Textured Surfaces. *Langmuir* **2013**, *29* (44), 13414–13418.

(37) Zhu, L.; Xue, J.; Wang, Y.; Chen, Q.; Ding, J.; Wang, Q. Ice-Phobic Coatings Based on Silicon-Oil-Infused Polydimethylsiloxane. *ACS Appl. Mater. Interfaces* **2013**, *5* (10), 4053–4062.

(38) Maitra, T.; Tiwari, M. K.; Antonini, C.; Schoch, P.; Jung, S.; Eberle, P.; Poulikakos,

D. On the Nanoengineering of Superhydrophobic and Impalement Resistant Surface Textures below the Freezing Temperature. *Nano Lett.* **2014**, *14*, 172–182.

(39) Eberle, P.; Tiwari, M. K.; Maitra, T.; Poulikakos, D. Rational Nanostructuring of Surfaces for Extraordinary Icephobicity. *Nanoscale* **2014**, *6*, 4874–4881.

(40) Maitra, T.; Antonini, C.; Auf der Mauer, M.; Stamatopoulos, C.; Tiwari, M. K.; Poulikakos, D. Hierarchically Nanotextured Surfaces Maintaining Superhydrophobicity under Severely Adverse Conditions. *Nanoscale* **2014**, *6* (15), 8710–8719.

(41) Jung, S.; Dorrestijn, M.; Raps, D.; Das, A.; Megaridis, C. M.; Poulikakos, D. Are Superhydrophobic Surfaces Best for Icephobicity. *Langmuir* **2011**, 3059–3066.

(42) Maitra, T.; Antonini, C.; Tiwari, M. K.; Mularczyk, A.; Schoch, P. Supercooled Water Drops Impacting Superhydrophobic Textures. **2014**.

(43) Schutzius, T. M.; Jung, S.; Maitra, T.; Eberle, P.; Antonini, C.; Stamatopoulos, C.; Poulikakos, D. Physics of Icing and Rational Design of Surfaces with Extraordinary Icephobicity. **2014**.

(44) Boreyko, J. B.; Collier, C. P. Delayed Frost Growth on Jumping-Drop Superhydrophobic Surfaces. *ACS Nano* **2013**, *7* (2), 1618–1627.

(45) Boreyko, J. B.; Srijanto, B. R.; Nguyen, T. D.; Vega, C.; Fuentes-Cabrera, M.; Collier, C. P. Dynamic Defrosting on Nanostructured Superhydrophobic Surfaces. *Langmuir* **2013**, *29*, 9516–9524.

(46) Chen, X.; Ma, R.; Zhou, H.; Zhou, X.; Che, L.; Yao, S.; Wang, Z. Activating the Microscale Edge Effect in a Hierarchical Surface for Frosting Suppression and Defrosting Promotion. *Sci. Rep.* **2013**, *3*, 2515.

(47) Nosonovsky, M.; Hejazi, V. Why Superhydrophobic Surfaces Are Not Always Icephobic. *ACS Nano* **2012**, *6* (10), 8488–8491.

(48) Farhadi, S.; Farzaneh, M.; Kulinich, S. A. Anti-Icing Performance of Superhydrophobic Surfaces. *Appl. Surf. Sci.* **2011**, *257* (14), 6264–6269.

(49) Smith, J. D.; Dhiman, R.; Anand, S.; Reza-Garduno, E.; Cohen, R. E.; McKinley, G. H.; Varanasi, K. K.; Quéré, D.; Patankar, N. A.; Tuteja, A.; et al. Droplet Mobility on Lubricant-Impregnated Surfaces. *Soft Matter* **2013**, *9* (6), 1772–1780.

(50) Kim, P.; Kreder, M. J.; Alvarenga, J.; Aizenberg, J. Hierarchical or Not? Effect of the Length Scale and Hierarchy of the Surface Roughness on Omniphobicity of Lubricant-Infused Substrates. *Nano Lett.* **2013**, *13* (4), 1793–1799.

(51) Rykaczewski, K.; Paxson, A. T.; Staymates, M.; Walker, M. L.; Sun, X.; Anand, S.; Srinivasan, S.; McKinley, G. H.; Chinn, J.; Scott, J. H. J.; et al. Dropwise Condensation of Low Surface Tension Fluids on Omniphobic Surfaces. *Sci. Rep.* **2014**, *4*, 4158.

(52) Lee, H.; Alcaraz, M. L.; Rubner, M. F.; Cohen, R. E. Zwitter-Wettability and Antifogging Coatings with Frost-Resisting Capabilities. *ACS Nano* **2013**, *7* (3), 2172–2185.

(53) Dou, R.; Chen, J.; Zhang, Y.; Wang, X.; Cui, D.; Song, Y.; Jiang, L.; Wang, J. Anti-Icing Coating with an Aqueous Lubricating Layer. *ACS Appl. Mater. Interfaces* **2014**, *6* (10), 6998–7003.

(54) Hermes, C.; Piucco, R.; Barbosa, J.; Melo, C. A Study of Frost Growth and Densification on Flat Surfaces. *Exp. Therm. ...* **2009**.

(55) Fletcher; Fletcher, N. H.; Squires, P.; Bowen, E. G. *The Physics of Rainclouds*; Cambridge University Press, 2011.

(56) Carey, V. P. (Van P. . *Liquid-Vapor Phase-Change Phenomena : An Introduction to the Thermophysics of Vaporization and Condensation Processes in Heat Transfer Equipment*; Taylor and Francis, 2008.

(57) Cai, L.; Wang, R.; Hou, P.; Zhang, X. Study on Restraining Frost Growth at Initial Stage by Hydrophobic Coating and Hygroscopic Coating. *Energy Build.* **2011**.

(58) Hoke, J. L.; Georgiadis, J. G.; Jacobi, A. M. Effect of Substrate Wettability on Frost Properties. *J. Thermophys. heat Transf.* **2004**, *18* (2), 228–235.

(59) Wu, X.; Webb, R. Investigation of the Possibility of Frost Release from a Cold Surface. *Exp. Therm. Fluid Sci.* **2001**.

(60) Lee, H.; Shin, J.; Ha, S.; Choi, B.; Lee, J. Frost Formation on a Plate with Different Surface Hydrophilicity. *Int. J. Heat Mass Transf.* **2004**, *47* (22), 4881–4893.

(61) Wang, H.; Tang, L.; Wu, X.; Dai, W.; Qiu, Y. Fabrication and Anti-Frosting Performance of Super Hydrophobic Coating Based on Modified Nano-Sized Calcium Carbonate and Ordinary Polyacrylate. *Appl. Surf. Sci.* **2007**, *253* (22),

8818–8824.

(62) Liu, Z.; Gou, Y.; Wang, J.; Cheng, S. Frost Formation on a Super-Hydrophobic Surface under Natural Convection Conditions. *Int. J. Heat Mass Transf.* **2008**, *51* (25–26), 5975–5982.

(63) He, M.; Wang, J.; Li, H.; Song, Y. Super-Hydrophobic Surfaces to Condensed Micro-Droplets at Temperatures below the Freezing Point Retard Ice/frost Formation. *Soft Matter* **2011**.

(64) Guadarrama-Cetina, J.; Mongruel, a.; González-Viñas, W.; Beysens, D. Frost Formation with Salt. *EPL (Europhysics Lett.* **2015**, *110* (5), 56002.

(65) Guadarrama-Cetina, J.; Narhe, R. D.; Beysens, D. a.; González-Viñas, W. Droplet Pattern and Condensation Gradient around a Humidity Sink. *Phys. Rev. E - Stat. Nonlinear, Soft Matter Phys.* **2014**, *89*, 1–10.

(66) Leach, R. N.; Stevens, F.; Langford, S. C.; Dickinson, J. T. Dropwise Condensation: Experiments and Simulations of Nucleation and Growth of Water Drops in a Cooling System. *Langmuir* **2006**, *22* (21), 8864–8872.

(67) Williams, R.; Blanc, J. Inhibition of Water Condensation by a Soluble Salt Nucleus. *J. Chem. Phys.* **1981**, *74* (8), 4675.

(68) Schäfle, C.; Leiderer, P.; Bechinger, C. Subpattern Formation during Condensation Processes on Structured Substrates. *EPL (Europhysics Lett.* **2003**.

(69) Neuwirth, M.; Daly, J. W.; Myers, C. W.; Tice, L. W. Morphology of the Granular Secretory Glands in Skin of Poison-Dart Frogs (Dendrobatidae). *Tissue Cell* **1979**, *11* (4), 755–771.

(70) Zheng, L.; Li, Z.; Bourdo, S.; Khedir, K. R.; Asar, M. P.; Ryerson, C. C.; Biris, A. S. Exceptional Superhydrophobicity and Low Velocity Impact Icephobicity of Acetone-Functionalized Carbon Nanotube Films. *Langmuir* **2011**, *27* (16), 9936–9943.

(71) Khedir, K. R.; Kannarpady, G. K.; Ishihara, H.; Woo, J.; Trigwell, S.; Ryerson, C.; Biris, A. S. Advanced Studies of Water Evaporation Kinetics over Teflon-Coated Tungsten Nanorod Surfaces with Variable Hydrophobicity and Morphology. *J. Phys. Chem. C* **2011**, *115* (28), 13804–13812.

(72) Khedir, K. R.; Kannarpady, G. K.; Ishihara, H.; Woo, J.; Asar, M. P.; Ryerson, C.;

Biris, A. S. Temperature-Dependent Bouncing of Super-Cooled Water on Teflon-Coated Superhydrophobic Tungsten Nanorods. *Appl. Surf. Sci.* **2013**, *279*, 76–84.

(73) Mockenhaupt, B.; Ensikat, H.-J.; Spaeth, M.; Barthlott, W. Superhydrophobicity of Biological and Technical Surfaces under Moisture Condensation: Stability in Relation to Surface Structure. *Langmuir* **2008**, *24* (23), 13591–13597.

(74) Rykaczewski, K.; Paxson, A. T.; Anand, S.; Chen, X.; Wang, Z.; Varanasi, K. K. Multimode Multidrop Serial Coalescence Effects during Condensation on Hierarchical Superhydrophobic Surfaces. *Langmuir* **2013**, *29* (3), 881–891.

(75) Kulinich, S. A.; Farhadi, S.; Nose, K.; Du, X. W. Superhydrophobic Surfaces: Are They Really Ice-Repellent? *Langmuir* **2011**, *27* (1), 25–29.

(76) Laforte, C.; Beisswenger, A. Icephobic Material Centrifuge Adhesion Test. **2005**.

(77) Aizenberg, J.; Black, A. J.; Whitesides, G. M. Oriented Growth of Calcite Controlled by Self-Assembled Monolayers of Functionalized Alkanethiols Supported on Gold and Silver. *J. Am. Chem. Soc.* **1999**, *121* (18), 4500–4509.

(78) Sun, X.; Damle, V. G.; Liu, S.; Rykaczewski, K. Bioinspired Stimuli-Responsive and Antifreeze-Secreting Anti-Icing Coatings. *Adv. Mater. Interfaces* **2015**, n/a-n/a.

(79) Viovy, J. L.; Beysens, D.; Knobler, C. M. Scaling Description for the Growth of Condensation Patterns on Surfaces. *Phys. Rev. A* **1988**, *37* (12), 4965–4970.

(80) Jung, S.; Tiwari, M. K.; Poulikakos, D. Frost Halos from Supercooled Water Droplets. *Proceedings of the National Academy of Sciences*. 2012.

(81) Nath, S.; Ahmadi, F.; Boreyko, J. B. A Review of Condensation Frosting. *Nanoscale Microscale Thermophys. Eng.* **2016**.

(82) Fletcher, N. H. J. Size Effect in Heterogeneous Nucleation. *J. Chem. Phys.* **1958**, *29* (3), 572–576.

(83) Cai, L.; Wang, R.; Hou, P.; Zhang, X. Study on Restraining Frost Growth at Initial Stage by Hydrophobic Coating and Hygroscopic Coating. In *Energy and Buildings*; 2011.

(84) Wang, Z. J.; Kwon, D. J.; Lawrence DeVries, K.; Park, J. M. Frost Formation and Anti-Icing Performance of a Hydrophobic Coating on Aluminum. *Exp. Therm. Fluid Sci.* **2015**, *60*, 132–137.

(85) El Cheikh, A.; Jacobi, A. A Mathematical Model for Frost Growth and Densification on Flat Surfaces. *Int. J. Heat Mass Transf.* **2014**, *77*, 604–611.

(86) Hermes, C. J. L.; Piucco, R. O.; Barbosa, J. R.; Melo, C. A Study of Frost Growth and Densification on Flat Surfaces. *Exp. Therm. Fluid Sci.* **2009**, *33* (2), 371–379.

(87) Shin, J.; Tikhonov, A. V.; Kim, C. Experimental Study on Frost Structure on Surfaces With Different Hydrophilicity: Density and Thermal Conductivity. *J. Heat Transfer* **2003**, *125* (1), 84.

(88) Wu, X. M.; Webb, R. L. Investigation of the Possibility of Frost Release from a Cold Surface. *Exp. Therm. Fluid Sci.* **2001**, *24* (3–4), 151–156.

(89) He, M.; Wang, J.; Li, H.; Song, Y. Super-Hydrophobic Surfaces to Condensed Micro-Droplets at Temperatures below the Freezing Point Retard Ice/frost Formation. *Soft Matter* **2011**, *7* (8), 3993.

(90) Gou, Y.; Liu, Z.; Wang, J.; Cheng, S. Frost Formation on a Bionic Super-Hydrophobic Surface under Natural Convection Conditions. *Heat Transf. - Asian Res.* **2008**, *37* (7), 412–420.

(91) Hao, Q.; Pang, Y.; Zhao, Y.; Zhang, J.; Feng, J.; Yao, S. Mechanism of Delayed Frost Growth on Superhydrophobic Surfaces with Jumping Condensates: More than Interdrop Freezing. *Langmuir* **2014**, *30* (51), 15416–15422.

(92) Mishchenko, L.; Khan, M.; Aizenberg, J.; Hatton, B. D. Spatial Control of Condensation and Freezing on Superhydrophobic Surfaces with Hydrophilic Patches. *Adv. Funct. Mater.* **2013**, *23* (36), 4577–4584.

(93) Oberli, L.; Caruso, D.; Hall, C.; Fabretto, M.; Murphy, P. J.; Evans, D. Condensation and Freezing of Droplets on Superhydrophobic Surfaces. *Advances in Colloid and Interface Science*. 2014, pp 47–57.

(94) Jing, T.; Kim, Y.; Lee, S.; Kim, D.; Kim, J.; Hwang, W. Frosting and Defrosting on Rigid Superhydrohobic Surface. *Appl. Surf. Sci.* **2013**, *276*, 37–42.

(95) Huang, L.; Liu, Z.; Liu, Y.; Gou, Y. Preparation and Anti-Frosting Performance of Super-Hydrophobic Surface Based on Copper Foil. *Int. J. Therm. Sci.* **2011**, *50* (4), 432–439.

(96) Xu, Q.; Li, J.; Tian, J.; Zhu, J.; Gao, X. Energy-Effective Frost-Free Coatings Based on Superhydrophobic Aligned Nanocones. *ACS Appl. Mater. Interfaces* **2014**, *6*,

8976–8980.

(97) Rykaczewski, K.; Scott, J. H. J. Methodology for Imaging Nano-to-Microscale Water Condensation Dynamics on Complex Nanostructures. *ACS Nano* **2011**, *5* (7), 5962–5968.

(98) Boreyko, J. B.; Chen, C.-H. Self-Propelled Dropwise Condensate on Superhydrophobic Surfaces. *Phys. Rev. Lett.* **2009**, *103* (18), 184501.

(99) Miljkovic, N.; Enright, R.; Nam, Y.; Lopez, K.; Dou, N.; Sack, J.; Wang, E. N. Jumping-Droplet-Enhanced Condensation on Scalable Superhydrophobic Nanostructured Surfaces. *Nano Lett.* **2013**, *13* (1), 179–187.

(100) He, M.; Li, H.; Wang, J.; Song, Y. Superhydrophobic Surface at Low Surface Temperature. *Appl. Phys. Lett.* **2011**, *98* (9), 93118.

(101) Chen, X.; Wu, J.; Ma, R.; Hua, M.; Koratkar, N.; Yao, S.; Wang, Z. Nanograssed Micropyramidal Architectures for Continuous Dropwise Condensation. *Adv. Funct. Mater.* **2011**, *21* (24), 4617–4623.

(102) Ghosh, A.; Beaini, S.; Zhang, B. J.; Ganguly, R.; Megaridis, C. M. Enhancing Dropwise Condensation through Bioinspired Wettability Patterning. *Langmuir* **2014**, *30* (43), 13103–13115.

(103) Garrod, R. P.; Harris, L. G.; Schofield, W. C. E.; McGettrick, J.; Ward, L. J.; Teare, D. O. H.; Badyal, J. P. S. Mimicking a Stenocara Beetle's Back for Microcondensation Using Plasmachemical Patterned Superhydrophobic-Superhydrophilic Surfaces. *Langmuir* **2007**, *23* (2), 689–693.

(104) Boreyko, J. B.; Hansen, R. R.; Murphy, K. R.; Nath, S.; Retterer, S. T.; Collier, C. P. Controlling Condensation and Frost Growth with Chemical Micropatterns. *Sci. Rep.* **2016**, *6*.

(105) Nath, S.; Boreyko, J. B. On Localized Vapor Pressure Gradients Governing Condensation and Frost Phenomena. *Langmuir* **2016**, *32* (33), 8350–8365.

(106) Leach, R.; Stevens, F.; Langford, S.; Dickinson, J. Dropwise Condensation: Experiments and Simulations of Nucleation and Growth of Water Drops in a Cooling System. *Langmuir* **2006**.

(107) Williams, R.; Blanc, J. Inhibition of Water Condensation by a Soluble Salt Nucleus Inhibition of Water Condensation by a Soluble Salt Nucleus. **2014**, *4675* (1981), 8–

11.

(108) Schäfle, C.; Leiderer, P.; Bechinger, C. Subpattern Formation during Condensation Processes on Structured Substrates. *Europhys. Lett.* **2007**, *63* (3), 394–400.

(109) Sun, X.; Damle, V. G.; Uppal, A.; Linder, R.; Chandrashekar, S.; Mohan, A. R.; Rykaczewski, K. Inhibition of Condensation Frosting by Arrays of Hygroscopic Antifreeze Drops. *Langmuir* **2015**, *31* (51), 13743–13752.

(110) Joanna Aizenberg, *,†; Andrew J. Black, ‡ and; George M. Whitesides*, ‡. Oriented Growth of Calcite Controlled by Self-Assembled Monolayers of Functionalized Alkanethiols Supported on Gold and Silver. **1999**.

(111) Sun, X.; Damle, V. G.; Liu, S.; Rykaczewski, K. Bioinspired Stimuli-Responsive and Antifreeze-Secreting Anti-Icing Coatings. *Adv. Mater. Interfaces* **2015**, *2* (5), 1400479.

(112) Marrero, T. R.; Mason, E. A. Gaseous Diffusion Coefficients. *J. Phys. Chem. Ref. Data* **1972**, *1* (1), 3–118.

(113) Liu, J.; Huang, X.; Li, Y.; Sulieman, K. M.; He, X.; Sun, F. Hierarchical Nanostructures of Cupric Oxide on a Copper Substrate: Controllable Morphology and Wettability. *J. Mater. Chem.* **2006**, *16*, 4427.

(114) Medici, M.-G.; Mongruel, A.; Royon, L.; Beysens, D. Edge Effects on Water Droplet Condensation. *Phys. Rev. E* **2014**, *90* (6), 62403.

(115) Yovanovich, M. M.; Marotta, E. E. Thermal Spreading and Contact Resistances. *Heat Transf. Handb.* **2003**, *1*, 261–394.

(116) Muzychka, Y. S.; Culham, J. R.; Yovanovich, M. M. Thermal Spreading Resistance of Eccentric Heat Sources on Rectangular Flux Channels. *J. Electron. Packag.* **2003**, *125* (2), 178–185.

(117) Guadarrama-Cetina, J.; Mongruel, A.; González-Viñas, W.; Beysens, D. Percolation-Induced Frost Formation. *Europhys. Lett.* **2013**, *101* (1), 16009.

(118) Ryerson, C. C. Assessment of Superstructure Ice Protection as Applied to Offshore Oil Operations Safety: Problems, Hazards, Needs, and Potential Transfer Technologies. *Erdc/Crrel Tr-08-14* **2008**, No. September, 156.

(119) Lacroix, A.; Manwell, J. F. Wind Energy: Cold Weather Issues. *Univ. Massachusetts* **2000**, No. June, 17.

(120) Huang, L.; Liu, Z.; Liu, Y.; Gou, Y.; Wang, J. Experimental Study on Frost Release on Fin-and-Tube Heat Exchangers by Use of a Novel Anti-Frosting Paint. *Exp. Therm. Fluid Sci.* **2009**, *33* (7), 1049–1054.

(121) Emery, A. F.; Siegel, B. L. Experimental Measurements of the Effects of Frost Formation on Heat Exchanger Performance. In *American Society of Mechanical Engineers, Heat Transfer Division*; Seattle, WA, 1990; pp 1–7.

(122) Liu, Q.; Yang, Y.; Huang, M.; Zhou, Y.; Liu, Y.; Liang, X. Durability of a Lubricant-Infused Electrospray Silicon Rubber Surface as an Anti-Icing Coating. *Appl. Surf. Sci.* **2015**, *346*, 68–76.

(123) Kreder, M. J.; Alvarenga, J.; Kim, P.; Aizenberg, J. Design of Anti-Icing Surfaces: Smooth, Textured or Slippery? *Nat. Rev. Mater.* **2016**, *1*, 15003.